

STUDIES ON CHEMICAL VAPOR DEPOSITION IN THE
GALLIUM INDIUM ARSENIDE PHOSPHIDE SYSTEM

By

CHINHO PARK

A DISSERTATION PRESENTED TO THE GRADUATE SCHOOL
OF THE UNIVERSITY OF FLORIDA IN PARTIAL FULFILLMENT
OF THE REQUIREMENTS FOR THE DEGREE OF DOCTOR OF PHILOSOPHY

UNIVERSITY OF FLORIDA

1992

ACKNOWLEDGEMENTS

The author wishes to express his sincere gratitude to his graduate advisor and committee chairman Dr. T. J. Anderson for his trust, guidance, and support throughout this educational program. He helped the author to understand and really enjoy the freedom of independent research. Also, many thanks go to the other members of his graduate committee, Dr. V. S. Ban, Dr. S. S. Li, Dr. L. E. Johns, and Dr. C. Park, for their advice and useful discussions.

The author wishes to thank many coworkers who worked with the author in various projects throughout his entire graduate studies. He had the good fortune to have been a visitor at Epitaxx, Inc., in Princeton, NJ, and is grateful for the advice and support of Dr. V. S. Ban, Dr. G. H. Olsen, Mr. G. Erickson, and Ms. S. Mason, in successfully accomplishing the hydride VPE projects. The author also wishes to thank Dr. K. P. Quinlan at Rome Air Development Center (U. S. Air Force), ESME, in Hanscom AFB, MA, for reviewing the work. The author also thanks Dr. W. M. Duncan and Mr. Q. Montague for their hospitality and support when he was visiting the Central Research Laboratory of Texas Instruments in Dallas, TX, to learn the Raman Spectroscopy and the low temperature Fourier Transform Photoluminescence for the characterization of hydride VPE grown InP samples. Many thanks also go to the other coworkers regarding the hydride VPE projects: Dr. F. Defoort for the complex equilibrium analysis of the hydride process, Dr. K. C. Hwang and Dr. S. S. Li for the surface passivation of GaInAs, Dr. P. H. Holloway for the sputter Auger electron spectroscopy measurements of GaInAs, Dr. B. Pathangey for the variable temperature Hall measurements of InP, and Dr. V. Zelezny for the analysis of the results of InP characterizat

are deeply appreciated. The author also wishes to thank the coworkers regarding the solid phase micro-Raman spectroscopy projects: Dr. A. Deneuve and Dr. P. Ayyub for the characterization of nitrogen and oxygen implanted ZnSe samples, and Dr. V. Zelezny for the characterization of GdBaCuO samples are deeply appreciated. Again, many thanks go to the coworkers regarding the OMCVD projects: Dr. Z. S. Huang for his experimental help and advice in the gas phase laser Raman spectroscopy, Dr. A. Zhao for the modeling and simulation of the upflow OMCVD reactor, and Dr. L. E. Johns for his valuable discussions with the author are deeply appreciated. Special thanks go to Mr. P. Axson for his friendship and assistance in the construction and operation of the Raman spectrometer and the OMCVD system. The author also gratefully acknowledges the financial support of U. S. Air Force, Microfabritech, and DARPA for portions of this study.

Warm, personal thanks go to the author's family, especially his wife Jawon, his son Jeehoon, and his daughter Jeasue, for their love and moral support throughout the course of his graduate studies. This work is dedicated to them and also to his parents, Dr. Joung K. Park and Ms. Young S. You.

TABLE OF CONTENTS

	<u>page</u>
ACKNOWLEDGEMENTS.....	ii
ABSTRACT.....	vi
CHAPTERS	
I INTRODUCTION.....	1
II HYDRIDE VPE OF GALLIUM INDIUM ARSENIDE USING A GALLIUM/INDIUM ALLOY SOURCE.....	10
2.1 Introduction.....	10
2.2 Experiment.....	12
2.3 Equilibrium Analysis of the Ga/In/As/Cl/H System.....	15
2.3.1 Method of Calculation.....	15
2.3.2 Source Zone Calculation.....	20
2.3.3 Deposition Zone Calculation.....	24
2.4 Results and Discussion.....	32
2.4.1 Parametric Studies.....	32
2.4.2 Source Zone Performance.....	46
2.5 Fabrication of <i>p-i-n</i> Photodetectors.....	54
2.6 Summary.....	57
III BACKGROUND IMPURITIES IN INDIUM PHOSPHIDE EPITAXIAL FILMS GROWN BY HYDRIDE VPE.....	59
3.1 Introduction.....	59
3.2 Experiment.....	62
3.3 Results and Discussion.....	65
3.3.1 Hall measurements.....	65
3.3.2 FTPL measurements.....	75
3.4 Summary.....	84
IV INVESTIGATION OF AN UPFLOW OMCVD REACTOR.....	86
4.1 Introduction.....	86
4.2 Experiment.....	90

4.2.1 Experimental System.....	90
4.2.2 Temperature Measurement.....	96
4.2.3 Tracer Experiment.....	103
4.3 Reactor Modeling and Simulation.....	105
4.4 Results and Discussion.....	111
4.4.1 Temperature Distribution in the Reactor.....	111
4.4.2 Tracer Study: Behavior of Reactants in the Reactor.....	123
4.4.3 Tracer Study: Transient Response of the Reactor.....	136
4.5 Summary.....	141
V CONCLUSIONS AND RECOMMENDED FUTURE WORK.....	144
REFERENCES.....	148
BIOGRAPHICAL SKETCH.....	158

Abstract of Dissertation Presented to the Graduate School
of the University of Florida in Partial Fulfillment
of the Requirements for the Degree of Doctor of Philosophy

STUDIES ON CHEMICAL VAPOR DEPOSITION IN THE
GALLIUM INDIUM ARSENIDE PHOSPHIDE SYSTEM

By

CHINHO PARK

August 1992

Chairman: Dr. Timothy James Anderson
Major Department: Chemical Engineering

Chemical vapor deposition (CVD) of $\text{Ga}_x\text{In}_{1-x}\text{As}_y\text{P}_{1-y}$ system has been investigated. Several issues have been examined in the growth of this quaternary compound semiconductor system by two major deposition techniques, hydride vapor phase epitaxy (VPE) and organo-metallic chemical vapor deposition (OMCVD).

A novel and simplified hydride VPE method based on the utilization of a Ga/In alloy as the group III source was experimentally investigated for deposition of $\text{Ga}_x\text{In}_{1-x}\text{As}$. The effects of a wide range of experimental variables (*i.e.*, inlet mole fractions of HCl and AsH_3 , deposition temperature, gas velocity, Ga/In alloy composition, and reactor geometry) on the ternary composition and growth rate were investigated. Layers of $\text{Ga}_{0.47}\text{In}_{0.53}\text{As}$ lattice matched to InP were successfully grown from alloys containing 5 to 8 at.% Ga. These layers were used to produce state-of-the-art *p-i-n* photodetectors. This study demonstrated for the first time that a simplified hydride VPE process with a Ga/In alloy source is capable of producing device quality epitaxial layers. Complex chemical equilibrium analysis of the Ga/In/As/Cl/H

system was performed to evaluate the dependence of solid solution composition on process parameters at equilibrium conditions. Comparison with experimental results showed a good agreement in the trend of this intensive variable.

Background impurities in epitaxial layers of InP grown by the hydride VPE technique were studied by low temperature Fourier-transform photoluminescence (FTPL) and variable temperature Hall measurements. The effects of source zone temperature and inlet mole fractions of HCl and PH₃ on the extent of impurity incorporation were investigated. The background carrier concentration was found to decrease with decreasing source zone temperature and increasing HCl, but was relatively independent of PH₃ for the range of mole fraction studied. The major impurities were identified as Si donors and Zn acceptors.

A stagnation point flow OMCVD reactor in which cold gas flows up toward a resistively heated susceptor was studied by gas phase laser Raman spectroscopy. Pure rotational Raman scattering by the carrier gas (N₂ or H₂) was used to determine the axial temperature profile in the reactor. The temperature profile was examined as a function of the inlet flow velocity and the reactor aspect ratio. A larger temperature gradient normal to the susceptor surface was obtained with higher gas flow velocity, larger aspect ratio, and the use of a N₂ carrier gas. The results were in good agreement with computed profiles of a two-dimensional axisymmetric model. A tracer molecule, CH₄, was used to investigate the behavior of reactants in the reactor and the transient switching response of the reactor. The use of a sweeping flow was found to be a good method for preventing wall depositions. Design of the gas inlet was tested and found to be critical in obtaining the well-defined gas dynamics in the reactor. Optimum operating conditions were developed for the study of reaction rates and the growth of InP epitaxial films.

CHAPTER I INTRODUCTION

Since the transistor was first invented by Shockley, Brattain, and Bardeen, in 1948, silicon has been the most widely used semiconductor in the solid state electronics industry primarily due to its good electrical properties, available high single-crystalline purity, and ease of use in the fabrication of semiconductor devices. The relatively low electron mobility and fixed indirect bandgap of silicon, however, makes its application difficult in the present-day optoelectronic devices which require extremely high speed and optical emission properties. These new demands have spurred the development of compound semiconductors composed of either elements from the group IIIB (Al, Ga, In) and group VB (N, P, As, Sb) or elements from the group IIB (Zn, Cd, Hg) and group VIB (S, Se, Te) columns of the periodic table. Semiconductors formed from combinations of these elements provide a large selection of electrical and physical properties suitable for a variety of modern-day optoelectronic devices such as light emitting diodes (LEDs), solid state lasers, photodetectors, high electron mobility transistors (HEMTs), and microwave devices. Among these materials, the group III-V semiconductors have been most widely used in the industry due to the availability of high quality binary substrates and the fairly well developed epitaxial growth techniques. Active research is still in progress for these III-V semiconductors, although much research interest has also been shown for the group II-VI semiconductors.

Table 1-1 lists the bandgap energy, electron mobility, lattice parameter, and refractive index of nine binary III-V semiconductors and silicon. Electron mobilities ranging from 80 to $10^5 \text{ cm}^2\text{V}^{-1}\text{s}^{-1}$ and bandgap energies ranging from 0.18 to 2.45 eV are available amongst the binary III-V semiconductors listed in this table, which sharply contrasts with the single

Table 1-1: Properties of Silicon and III-V Binary Compound Semiconductors at 300 K[1].

	Bandgap Energy (eV)	Electron Mobility (cm ² V ⁻¹ s ⁻¹)	Lattice Parameter (Å)	Refractive Index
Si	1.12 (I)	1350	5.4300	3.400
AlP	2.45 (I)	80	5.4625	3.027
AlAs	2.16 (I)	180	5.6611	3.178
AlSb	1.60 (I)	200	6.1355	3.400
GaP	2.26 (I)	300	5.4495	3.452
GaAs	1.43 (D)	8500	5.6419	3.655
GaSb	0.70 (D)	5000	6.0940	3.820
InP	1.28 (D)	4000	5.8687	3.450
InAs	0.36 (D)	22600	6.0584	3.520
InSb	0.18 (D)	100000	6.4788	4.000

(I): Indirect bandgap

(D): Direct bandgap

available set of these values for silicon. Five of the nine compounds listed (GaAs, GaSb, InP, InAs, InSb) have a direct bandgap. The direct nature of the energy band structure of many III-V semiconductors allows for the efficient conversion of electromagnetic radiation into electric current (photodetectors, photovoltaic cells) or electric current into the emission of electromagnetic radiation (LEDs, lasers), since a third particle (*e.g.*, phonon) is not necessary for the generation and recombination of free carriers. Direct bandgap III-V semiconductors generally have higher electron mobilities, in some cases as much as two orders of magnitude higher values, compared with that of silicon.

III-V compound semiconductors are not limited to simple binary compounds, and indeed, a wide range of compound semiconductors can be formed by creating solid solutions of the individual elements. Most device structures include heteroepitaxial growth of multicomponent solid solutions that are lattice matched to the available binary substrates. These structures permit variation of the physical and electrical properties continuously between the property limits of the constituent binary compounds, and this provides device applications beyond the range possible with elemental or binary compound semiconductors. Figure 1-1 shows a plot of the lattice parameter versus the bandgap energy (at 300 K) for many III-V compound semiconductors. Solid dots indicate binary compounds, solid lines connecting dots indicate direct bandgap ternary solutions of intermediate composition between the binaries, and dashed lines connecting dots represent indirect bandgap ternary solutions. Essentially, the entire area bounded by the solid and dashed lines is available for use in the design of new III-V semiconductor devices employing ternary and quaternary solid solutions.

In terms of present optoelectronic device applications, $\text{Ga}_x\text{In}_{1-x}\text{As}_y\text{P}_{1-y}$ is the most important III-V quaternary compound semiconductor system, and the available ranges for the lattice parameter and bandgap energy in this system are given by the cross-hatched area shown in Figure 1-1. The lattice parameter and bandgap energy can be independently specified with the compositions of the quaternary solution chosen to meet these specifications. To maintain a

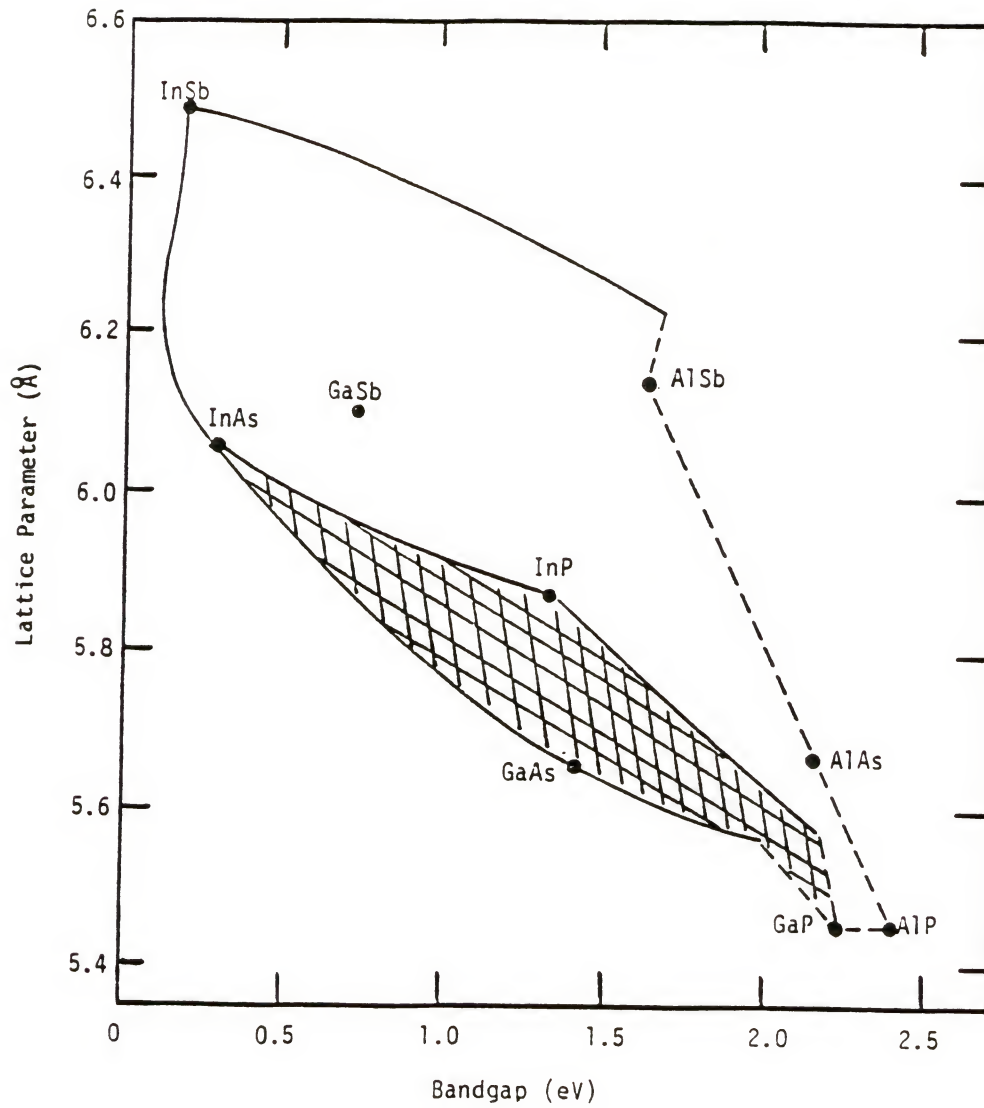


Figure 1-1: Lattice parameter and bandgap energy of various III-V semiconductors.

given lattice parameter for the quaternary system a simultaneous variation of the Ga/In and As/P ratio is required. The availability of a degree of freedom in the lattice parameter is extremely important, since only the Ga and In binary compounds (GaP, GaAs, GaSb, InP, InAs, InSb) are commercially available as substrate materials because of the difficulties related to the preparation of Al containing compounds and solid solutions (only GaAs and InP are produced in large quantity with good quality at the present time). In the case of $\text{Ga}_x\text{In}_{1-x}\text{As}_y\text{P}_{1-y}$ on InP, for example, a lattice-mismatch of greater than 0.1% between the grown film and the substrate induces, for film thicknesses greater than the critical thickness, the formation of structural defects which can degrade the device performance. The $\text{Ga}_x\text{In}_{1-x}\text{As}_y\text{P}_{1-y}$ system is used for many device applications. For example, $\text{Ga}_x\text{In}_{1-x}\text{As}_y\text{P}_{1-y}$ lattice matched to InP has aroused great interest for sources in optical fiber communications systems operating at the wavelength of 1.3 μm and 1.55 μm where high quality fused silica fibers exhibit minimum transmission loss (less than 1 dB/km) and minimum dispersion[2]. The ternary endpoint of this material system, $\text{Ga}_{0.47}\text{In}_{0.53}\text{As}$ lattice matched to InP has been developed as photodetectors to complement the 1.3 to 1.6 μm light sources. The interest in $\text{Ga}_{0.47}\text{In}_{0.53}\text{As}$ latticed matched to InP has been recently expanded to microwave and millimeter-wave device applications due to its superior mobilities and velocity-field characteristics. Room temperature mobilities in the range 11000 to 13800 $\text{cm}^2\text{V}^{-1}\text{s}^{-1}$ have been recorded for this material[3-5]. $\text{Ga}_x\text{In}_{1-x}\text{As}_y\text{P}_{1-y}$ lattice matched to GaAs with a shorter wavelength is of interest in the application of visible lasers and LEDs[2].

$\text{Ga}_x\text{In}_{1-x}\text{As}_y\text{P}_{1-y}$ can be grown by a number of techniques including liquid phase epitaxy (LPE), chloride and hydride vapor phase epitaxy (VPE), organo-metallic chemical vapor deposition (OMCVD), molecular beam epitaxy (MBE), and recently developed techniques such as atomic layer epitaxy (ALE)[6], chemical beam epitaxy (CBE)[7] which are variations of OMCVD and MBE. Each technique has its own advantages and drawbacks, and excellent reviews can be found in the literature which discuss the general aspects of these techniques.

LPE[8] is a growth technique which can be used to deposit thin single crystal layers of III-V compound semiconductors from a heated liquid solution by decreasing the temperature of the substrate relative to the solution. It is a relatively simple, inexpensive, near equilibrium (reproducible) technique that is well understood. The growth rate can be high, and a wide range of both p- and n-type dopants are available and their incorporation is controllable. LPE has been used to grow InP[9] and high quality $\text{Ga}_x\text{In}_{1-x}\text{As}$ on InP and $\text{Al}_x\text{Ga}_{1-x}\text{As}$ on GaAs[10] for laser applications. However, problems such as surface defects, poor thickness and compositional uniformity, and difficulty in growing abrupt heterojunctions have made the LPE less attractive for present-day device fabrication demands.

Chloride VPE[11] uses chloride species (*e.g.*, AsCl_3 , PCl_3) as group V sources with group III metals (*e.g.*, Ga, In) in an open tube system. H_2 is used as a carrier gas to transport reactants from the source zone, through the mixing zone, to the deposition zone where deposition occurs at the substrate surface. It is a well-established vapor phase technique for the growth of $\text{Ga}_x\text{In}_{1-x}\text{As}_y\text{P}_{1-y}$ with high growth rate and high purity. However, it is difficult to vary the III/V ratio, and a careful source composition control and an accurate temperature control throughout the system are required for process reproducibility. Source transients are also long and consequently, it is hard to grow abrupt heterojunctions. Hydride VPE[12] differs from chloride VPE by replacing group V chlorides with group V hydrides (*e.g.*, AsH_3 , PH_3). In the case of InP growth, for example, HCl gas is first reacted with liquid indium metal in the source zone. The gaseous product InCl is then carried by H_2 to mix with PH_3 in the mixing zone and to react with PH_3 and its thermal decomposition products (*e.g.*, P_4 , P_2) in the deposition zone. Typically the source and mixing zones in the hydride system are operated at higher temperatures than those of the chloride system in order to increase the rate of PH_3 decomposition, since the decomposition kinetics of PH_3 are much slower than that of PCl_3 . One major advantage of the hydride process over the chloride process is the ability to vary the vapor III/V ratio by adjusting the inlet compositions or flow rates of VH_3 and HCl. Hydride

VPE is currently widely used for LED applications using $\text{GaAs}_y\text{P}_{1-y}$. It has also found applications in the growth of $\text{Ga}_x\text{In}_{1-x}\text{As}_y\text{P}_{1-y}$ and $\text{Ga}_x\text{In}_{1-x}\text{As}$ for LEDs, lasers, and photodetectors[13]. One drawback of both the chloride and hydride VPE is that they both use hot-wall reactors, and the interaction between the vapor and heated SiO_2 reactor wall occurs, which results in the unintentional incorporation of Si into the grown layers. Also, these VPE techniques are not suitable for the growth of Al containing compounds.

Another important vapor phase growth technique is OMCVD[14]. The OMCVD technique involves an irreversible pyrolysis reaction in which a group III organometallic species is fed to a cold wall reactor along with a group V species (usually hydrides). These species then contact a heated substrate, decompose, and deposit an epitaxial layer onto the substrate. Typically, the OMCVD process is limited by mass transport of the group III species through a stagnant layer near the growing surface. The technique is capable of growing a wide variety of films (including Al-containing compounds) with excellent abruptness and uniformity over large substrate areas. The OMCVD technique has been widely used in optoelectronic device applications. One problem inherent to this technique is the unintentional incorporation of carbon as an acceptor. Other unintentional dopants include Mg, Zn, and Si which are often present as impurities in the organometallic source material. The cold wall design employed in the OMCVD technique results in significant deposition on the reactor wall, and dopants which have been deposited on the wall often desorb during a later stage of the deposition process.

MBE[15] is a technique capable of growing epitaxial thin films by impinging one or more thermal energy beams of atoms or molecules onto a heated substrate in an ultra high vacuum environment. The distinguishing characteristic of MBE is the slow growth rate ($0.1 - 2 \mu\text{m/hr}$) which, in combination with relatively low growth temperatures, permits precise control of layer thickness, composition, and doping profiles[16]. Additionally, in-situ analyses of the surface structure and reaction conditions during growth are possible by the attached monitoring techniques such as RHEED, mass spectrometry, Auger electron spectroscopy. Numerous

devices such as LEDs, lasers, FETs, and HBTs have been fabricated with MBE. However, the high expense and low throughput limit the usage of MBE technique to research and small-scale production.

In this dissertation, several aspects of the current problems involved in the chemical vapor deposition of $\text{Ga}_x\text{In}_{1-x}\text{As}_y\text{P}_{1-y}$ are presented. Two major deposition techniques, hydride VPE and OMCVD, have been studied to address the current issues in these growth techniques. These issues include composition control and unintentional doping in the case of hydride VPE and gas dynamics in the OMCVD reactor. An unified approach to these problems was taken by employing necessary experiments and calculations. Chapter II presents a study of hydride VPE for the deposition of $\text{Ga}_x\text{In}_{1-x}\text{As}$ on InP using a Ga/In alloy source. This method eliminates the need for independent control of HCl to each source material which is required in conventional hydride VPE, thereby providing better reproducibility and control of the composition of the ternary compound. Furthermore it ensures uniform mixing of the group III species. A comprehensive experimental study was undertaken to investigate this novel, simplified method. The effects of a wide range of experimental variables on the ternary composition and growth rate were investigated, and the results are discussed. A complex chemical equilibrium analysis of the process was performed to evaluate the dependence of the solid solution composition on process parameters at equilibrium conditions and was compared with the experimental observations. State-of-the-art *p-i-n* photodetectors were fabricated for the first time by this new method to demonstrate that it is capable of producing device-quality epitaxial layers. In chapter III, an experimental study of the unintentional doping of hydride VPE grown InP epitaxial layers is presented. Understanding and control of the background impurities are very important in achieving the desired device performances. The effects of process parameters on impurity incorporation were studied by low temperature Fourier-transform photoluminescence (FTPL) and variable temperature Hall measurement. The background impurities were identified by the peak positions of FTPL spectra, and the mobilities and carrier concentrations of the InP layers

were determined by the Hall measurements. Chapter IV presents a study of the gas dynamics in a vertical upflow OMCVD reactor. This reactor configuration was proposed to have well-defined gas dynamics for conducting kinetic experiments to study the reaction rates and the growth of epitaxial layers. It can also be used as an actual reactor to grow device structures. Raman spectroscopy was employed as a method of measuring the thermal profiles in the reactor and monitoring the behavior of reactants in the reactor with the use of a tracer molecule, CH_4 . The axial temperature profiles in the reactor were studied as a function of process and design variables. A two-dimensional axisymmetric model of the reactor was developed, and the calculations were compared with the experimental observations. The behavior of reactants in the reactor was investigated as a function of operating parameters, and the emphasis was put on the use of a sweeping flow as a method to prevent the depositions on the reactor wall. The transient switching response of the reactor was also investigated, and the design of the gas inlet was tested. Finally, conclusions of this dissertation work are given in chapter V, and suggestions for future work are discussed.

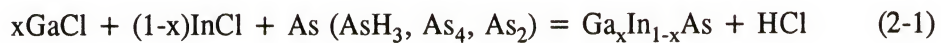
CHAPTER II

HYDRIDE VPE OF GALLIUM INDIUM ARSENIDE USING A GALLIUM/INDIUM ALLOY SOURCE

2.1 Introduction

Epitaxial layers of $\text{Ga}_x\text{In}_{1-x}\text{As}$ on InP substrates have properties which make them extremely attractive for a wide range of optoelectronic and electronic device applications. As an example, $\text{Ga}_x\text{In}_{1-x}\text{As}$ is used as the active layer in photodiode structures important in long wavelength optical communication technology. This active layer must have a low background carrier concentration and zero lattice mismatch to the substrate for production of quality devices. The hydride vapor phase epitaxy (VPE) technique has several advantages for large-scale production of such devices, including high purity, high growth rate, and process controllability. Since hydride VPE can be operated at conditions for which growth is limited by surface reaction, the technique is attractive for applications which require uniform growth rates and epitaxy selectivity.

In conventional hydride VPE, a HCl/H_2 gas mixture is reacted with separate Ga and In liquid sources to form volatile group III chloride species (mostly monochlorides). The source zone products then mix with group V hydride (AsH_3) in the mixing zone where the hydride is decomposed, and finally, the epitaxial layers of $\text{Ga}_x\text{In}_{1-x}\text{As}$ are deposited on the substrate in the deposition zone according to the following process:



Experimental results[17] and thermodynamic calculations[18-20] indicate that the deposited film composition is very sensitive to the vapor phase molar ratio of Ga to In

generated in the separate sources; this ratio must be controlled to better than 0.1% for some device applications. Since the sensitivity of the film composition to the Ga/In molar ratio is highest near the condition to grow $\text{Ga}_x\text{In}_{1-x}\text{As}$ lattice matched to InP, extremely fine control of the HCl flows to both source zones is required. Equilibrium conversion of HCl is not always attained in many of the reactors[18,21,22]. Therefore, run to run reproducibility of the deposited film composition can be influenced by factors which alter mass transfer and reaction rates in the source zone (*e.g.*, liquid metal height, flow velocity)[18]. Radial compositional uniformity in the deposited film is also affected by the degree of mixing of the gas streams exiting the separated source regions.

Several investigators[23-29] have proposed using a binary liquid alloy source to improve the quality of the deposited layers. Although the growth rate is affected by changes in the group III transport rate, the molar ratio of transported Ga to In or the film composition should be less sensitive to variations in the HCl flow rate or reaction efficiency with an alloy source. The Ga/In alloy source also eliminates the need for gas phase mixing of the group III species. In addition, the alloy-source technique will require less expensive reactors with simplified process operations.

The alloy source has been experimentally investigated using either HCl[24-28] or AsCl_3/H_2 [23,29] as the source of HCl with a separate flow of AsH_3 [24,26-28] or AsCl_3 [25] (chloride VPE). A full parametric study of the hydride VPE using an alloy source has not yet been reported. The reported alloy-source composition required to produce $\text{Ga}_{0.47}\text{In}_{0.53}\text{As}$ films lattice matched to InP varies from 3.2 to 12.2 at.% Ga[24-26,28]. This study reports the influence of alloy-source composition and other process parameters (*e.g.*, inlet mole fraction of AsH_3 and HCl, deposition temperature) on the film composition and growth rate. An interesting observation by Quinlan and Erstfeld[27] is the growth of a limiting $\text{Ga}_{0.87}\text{In}_{0.13}\text{As}$ film composition by the addition of excess HCl downstream of the source zone. Similar experiments are repeated for two different source alloy compositions and the results are

reported. A complex chemical equilibrium analysis is also performed on the Ga/In/As/Cl/H system to explain the experimentally observed trends in the solid solution composition.

Operation of the group III metal source with equilibrium conversion is desirable to achieve reproducible transport rates. The present study shows that the traditional open-boat design gives non-equilibrium conversion. A modified source boat was studied and further design changes are suggested to overcome these limitations. The transport of Ga and In with an alloy source has been shown to occur by incongruent reaction, thus limiting the source life-time[25]. It is shown in this study that the source life-time can be increased by the gradual variation of deposition parameters to counter the run-to-run variation in the alloy composition. In addition, state-of-the-art *p-i-n* photodetectors were fabricated in order to demonstrate that an alloy source is capable of producing device-quality epitaxial films.

2.2 Experiment

The hydride VPE reactor used in this study was the double-barrel reactor design, which has been functioning at Epitaxx, Inc. in Princeton, New Jersey, and its simplified schematic is shown in Figure 2-1. The system consists of three basic parts: (1) the gas handling system, (2) the reactor/substrate loading system, and (3) the exhaust/scrubbing system. The reactor/substrate loading system is composed of source zone, mixing zone, deposition zone, and entrance load-lock chamber. The reactor is a horizontal open-tube made of quartz, and it is heated by a clam-shell furnace with six independent temperature controllers to obtain a desired temperature profile in the reactor. It has been successfully used to produce a large variety of III-V compounds and devices, and the details of the reactor design are described elsewhere[30-32]. Instead of using separate Ga and In source boats, a single alloy boat containing gallium and indium was inserted into one of the In source barrels. Alloy compositions of 5.35, 8.69 and 15.10 at.% Ga were studied. Excess HCl could be introduced into the mixing zone via a dopant line. The base operating conditions used in this study were the following: source zone

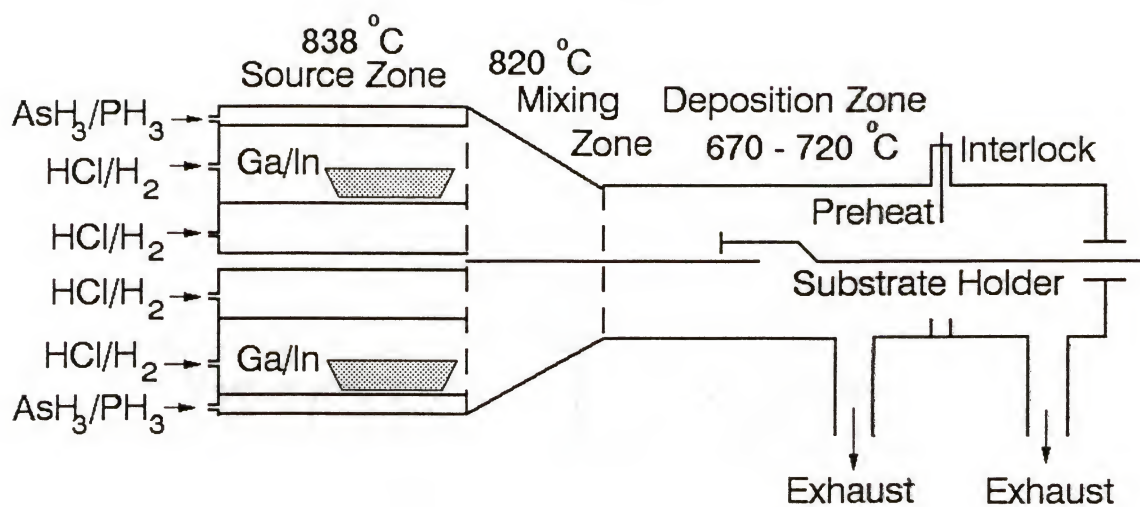


Figure 2-1: Schematic of the hydride VPE double barrel reactor.

temperature, 838 °C; mixing zone temperature, 820 °C; deposition temperature, 700 °C; and total pressure, 1 atm. The III/V ratio was fixed at a value of two and the total volumetric flow rate in the deposition zone was held constant at 4200 sccm (25 cm/s linear velocity). These values are based on previous work and were found to produce excellent epitaxial layer properties (*e.g.*, surface morphology, interfacial quality, and photoelectrical properties). Study of the inlet mole fractions of HCl and AsH₃, deposition temperature, source gas velocity, source alloy composition, excess HCl, and source geometry was performed around these base operating conditions.

Volatile metal chlorides were generated and transported by combining streams of HCl (100%) in H₂ (carrier gas). The carrier gas was purified by Pd-alloy diffusion. Arsine or phosphine (which was used to stabilize the InP surface prior to deposition and to grow InP cap and buffer layers) was introduced as 10% mixtures of AsH₃ and PH₃ in H₂. The purity of reactant gases was at a level to give background doping of epitaxial layers routinely in the range 5×10^{14} to 5×10^{15} cm⁻³. The metals, Ga and In, were 99.99999% pure. Substrates grown by the liquid encapsulated Czochralski (LEC) method were S or Fe doped InP, cut 2° off the (100) toward the nearest (110).

Substrates were etched in Caro's acid (5:1:1 H₂SO₄:H₂O₂:H₂O) and a 1% Br₂ in CH₃OH solution. The etched substrate, typically about 1×1 cm², was placed into the reactor load-lock chamber and flushed with H₂ prior to opening the reactor. Reactant flows were initiated about 15 min prior to the insertion of substrates in order to avoid significant transient effects. The substrates were preheated in a PH₃/H₂ mixture ($P_{PH_3}^{\circ} = 3.9 \times 10^{-2}$ atm) to prevent surface decomposition and extraneous initial deposition and to promote desorption of native oxides on the surface. No deposition on the quartz wall or substrate holder was observed during most of the depositions. The alloy source was baked for 50 hrs at 838 °C in flowing H₂ before deposition to insure the complete mixing of In and Ga and to lower the background doping concentrations in the resulting films[24].

The layer thickness was measured by optical microscopy on cleaved and stained samples. The composition of $\text{Ga}_x\text{In}_{1-x}\text{As}$ epitaxial layers was determined from Vegard's law using lattice parameters measured with a Siemens single-crystal x-ray diffractometer. The initial and final compositions of the Ga/In source alloy were determined by atomic absorption spectroscopy. The alloys for these analyses were remelted and rapidly quenched to 77 K to form an alloy of uniform composition[26].

2.3 Equilibrium Analysis of the Ga/In/As/Cl/H System

2.3.1 Method of Calculation

The calculation of complex chemical equilibrium in multicomponent, multiphase systems has been reviewed most completely by Smith[33]. Essentially, there are two types of the solution to this problem. Nonstoichiometric methods, such as the Rand algorithm[34], directly minimize the Gibbs energy of the total system in order to obtain a solution without recourse to a specific set of formation reaction equations. Stoichiometric methods[35] require that an independent set of chemical reactions be in equilibrium. Generally, a formation reaction is written for each species present in the system and the corresponding equilibrium constant for each reaction is generated from the Gibbs energy change of the reaction.

An extension of the Rand algorithm to include not only a gas phase with an inert species, but also a multicomponent solution and pure condensed phases, was developed by Anderson[36], and it was initially applied to the hydride and chloride VPE systems. However, this algorithm was susceptible to finding local minima, and in particular, some component mole fractions sought were as low as 0.1 ppb. The contribution to the system Gibbs energy for these components was quite small and the resulting component mole changes were not capable of releasing the Gibbs energy of the system from the local minima. A stoichiometric algorithm was therefore developed and coded by Meyer[37], and it was successfully applied to the

hydride and chloride VPE systems. It was superior to the extended Rand algorithm since a linearized Gibbs energy function was not required, and also the amount of computer memory required for the stoichiometric algorithm was found to be much less than that required by the extended Rand algorithm in order to solve identical systems. The stoichiometric algorithm developed by Meyer[37] was essentially used in this work, with some improvements made in the original program to include different solution models for the solid and liquid solutions. All the thermochemical data have been critically reviewed, and the new data set was employed in the calculation.

Three major factors determine the overall accuracy of the calculated equilibrium compositions: (1) the choice of species postulated to be present in the system, (2) the accuracy of the thermodynamic data chosen to represent each pure species, and (3) the choice of solution model. Choosing an appropriate set of species, which accurately represent the system at equilibrium, is an inherent difficulty in the calculation of multicomponent equilibrium. A true calculation of equilibrium in a given system must include any chemical species which is formed from any combination of the elements present in the system. However, the compilation of such a complete thermodynamic data base can represent a nearly impossible task, even for systems consisting of only a few elements. Fortunately many species are either present in extremely low concentrations at equilibrium or their formation is limited by kinetics. Therefore, the selection of species must be carefully made such that it does not alter or disguise the reality.

Table 2-1 lists the chemical species chosen for the Ga/In/As/Cl/H system with selected thermochemical values. Near one atmospheric pressure and in the temperature range of interest to VPE (600 - 900 °C), some of the species are fairly unstable, thus insignificant in quantity. Equilibrium mole fractions of the gallium hydrides and indium hydrides are typically less than 10^{-10} , hence they are excluded from consideration. The binary compound vapor species of GaAs and InAs are also insignificant and do not have a great impact on the overall chemical equilibrium. Group III chlorides and group V molecules are the dominant species in the

Table 2-1: Chemical Species Considered for the Complex Chemical Equilibrium Analysis of the Ga/In/As/Cl/H System with Selected Thermochemical Values.

Species	$\Delta H_f^\circ(298K)$ (kcal/mol)	Ref.	$S^\circ(298K)$ (cal/mol-K)	Ref.	C_p° (cal/mol-K)				Form	Ref.
					a	b	c	d		
As(g)	68.7	[38]	41.611	[38]	4.968	-----	-----	-----	1	[38]
As ₂ (g)	45.95	[37]	57.546	[38]	7.630	-0.169	-0.3708	0.212	1	[38]
As ₃ (g)	52.2	[38]	74.121	[38]	13.836	-0.1365	-0.5889	0.172	1	[38]
As ₄ (g)	37.5	[37]	78.232	[38]	18.516	-0.1756	-1.1128	0.218	1	[38]
AsCl(g)	27	[39]	66.24	[39]	8.878	0.0453	-0.3815	-----	1	[39]
AsCl ₂ (g)	14.5	[39]	72.04	[39]	13.79	0.08566	-0.8524	-----	1	[39]
AsCl ₃ (g)	-62.7	[37]	77.97	[39]	19.76	0.0726	-1.5766	-----	1	[39]
AsH(g)	58	[37]	51	[37]	6.4	1.432	0.108	-----	1	[40]
AsH ₃ (g)	16	[41]	53.22	[42]	10.07	5.42	-2.20	-----	1	[43]
Cl(g)	28.992	[44]	39.454	[44]	5.779	-0.4083	-0.387	-----	1	[45]
Cl ₂ (g)	0	---	53.29	[44]	8.8	0.208	-0.67	-----	1	[40]
Ga(g)	65.0	[38]	40.375	[38]	30.138	2.09	-2.662	-3.812	1	[38]
GaCl(g)	-16.43	[46]	57.236	[46]	8.8475	0.23288	-0.49179	-0.39757	3	[46]
GaCl ₂ (g)	-31.0	[46]	71.668	[46]	13.794	0.13396	-0.40503	-0.83318	3	[46]
GaCl ₃ (g)	-102.4	[46]	77.515	[46]	19.463	0.56688	-2.11570	-1.51840	3	[46]
Ga ₂ Cl ₂ (g)	-43.3	[46]	84.52	[46]	19.842	0.02843	-0.07060	-0.70484	3	[46]
Ga ₂ Cl ₄ (g)	-139.0	[46]	106.78	[46]	27.628	0.20703	-0.57781	-1.83760	3	[46]
Ga ₂ Cl ₆ (g)	-228.9	[46]	117.74	[46]	42.554	1.40800	-4.23770	-2.75690	3	[46]
H(g)	52.103	[44]	27.391	[44]	4.968	-----	-----	-----	1	[47]
H ₂ (g)	0	---	31.207	[44]	15.256	2.12	-0.5906	-1.462	1	[40]

Table 2-1: Continued.

Species	$\Delta H_f^\circ(298\text{K})$ (kcal/mol)	Ref.	$S^\circ(298\text{K})$ (cal/mol-K)	Ref.	$C_p^\circ(\text{cal/mol-K})$				Form	Ref.
					a	b	c	d		
HCl(g)	-22.063	[44]	44.643	[44]	6.224	1.29	0.3251	-----	1	[40]
In(g)	57.3	[37]	41.507	[38]	3.575	4.426	-----	-1.689×10^6	2	[38]
InCl(g)	-16.9	[47]	59.255	[47]	8.9004	0.05843	-0.21865	-0.28166	3	[47]
InCl ₂ (g)	-39.0	[47]	75.3	[47]	13.505	0.63122	-2.6803	-1.03040	3	[47]
InCl ₃ (g)	-90.0	[47]	81.45	[47]	19.552	0.48698	-2.0179	-1.21710	3	[47]
In ₂ Cl ₂ (g)	-55.9	[47]	88.94	[47]	19.843	0.040298	-0.1511	-0.50377	3	[47]
In ₂ Cl ₄ (g)	-137.0	[47]	110.81	[47]	28.142	4.0013	-12.718	-7.8477	3	[47]
In ₂ Cl ₆ (g)	-211.5	[47]	127.24	[47]	42.554	1.408	-4.2377	-2.7569	3	[47]
Ga(l)	1.33	[37]	14.169	[37]	6.35	-----	-----	-----	1	[37]
In(l)	0.754	[37]	15.56	[37]	7.05	-----	-----	-----	1	[37]
GaAs(s)	-19.54	[48]	16.05	[48]	11.015	1.9915	-----	-----	1	[48]
InAs(s)	-14.29	[48]	17.84	[48]	11.822	2.026	-----	-----	1	[48]

Form:

$$1: C_p = a + b \times 10^{-3} T + c \times 10^5 T^{-2} + d \ln T$$

$$2: C_p = a + b \times 10^{-3} T + c \times 10^5 T^2 + d T^3$$

$$3: C_p = a + b \times 10^{-3} T + c \times 10^{-7} T^2 + d \times 10^5 T^{-2}$$

Ga/In/As/Cl/H system. Kinetic studies on the growth of GaAs have indicated that gallium monochloride and arsenic molecules are responsible for the epitaxial reaction in a hydrogen-rich ambient, and gallium trichloride plays a certain role in a hydrogen-deficient ambient. Although some of the group III chlorides are less important than the others, all of them are included. For similar reasons, the group V molecules composed of different number of atoms should all be considered. The inclusion of all possible group V hydride species is also meaningful. However, some of the species formed by arsenic atoms (*e.g.*, AsH₂, As₂H₂, As₂H₄) are not included in the calculation, since those molecules have not been adequately studied and their reported thermochemical properties are, at present, missing or inconclusive. There is no evidence that these species are present in VPE. Finally, 28 vapor species are selected with two condensed phase solutions, the Ga/In liquid alloy in the source zone and Ga_xIn_{1-x}As solid solution in the deposition zone.

Accuracy of the thermochemical data is very important in performing meaningful equilibrium calculations. The absolute composition of the calculated solution can be no better than the data set employed. The thermochemical data listed in Table 2-1 are largely based on the Meyer's data set[37], except for the values for the six gallium chlorides[46], six indium chlorides[47], GaAs(s)[48], and InAs(s)[48], which have been recently assessed. These new data result from a critical review of the thermochemical data published in the literature. As a result of these reviews, the species that showed large uncertainties were experimentally determined[46-48].

The choice of solution model is equally important for accurate equilibrium calculations. An excellent review has been recently published by Hsieh[18] of common solution models for the Ga/In/As/P semiconductor system. Several of these models were tested in the equilibrium calculation for both the Ga_xIn_{1-x} liquid alloy and the Ga_xIn_{1-x}As solid solution. The results are compared and discussed in the following sections.

2.3.2 Source Zone Calculation

The chemical system in the source zone is constituted by four elements (Ga, In, Cl, and H) which form species in two phases (vapor and $\text{Ga}_x\text{In}_{1-x}$ liquid). The gallium and indium chlorides are generated by chemical reaction between hydrogen chloride and the liquid alloy of gallium and indium. Equilibrium calculations have been made as a function of the actual experimental process parameters used in this study, *i.e.*, source zone temperature (T_s), total pressure (P_t), inlet mole fraction of HCl (x_{HCl}^o), and source alloy composition ($x_{\text{Ga}}(\text{l})$).

Figure 2-2 shows the composition of the gas phase in equilibrium with the $\text{Ga}_x\text{In}_{1-x}$ liquid alloy. Mole fractions of gas phase species are plotted as a function of source zone temperature. The source alloy composition is 8.69 at.% Ga, and the Cl/H ratio is 1.48×10^{-2} ($x_{\text{HCl}}^o = 7.2 \times 10^{-3}$) which corresponds to 30 sccm of HCl flow in 1000 sccm of H_2 carrier flow. Obviously the major vapor species are indium monochloride and gallium monochloride except for the most abundant H_2 carrier. HCl is almost completely consumed by the liquid alloy ($> 98\%$). The most important second order species are In_2Cl_2 and atomic indium. It is noted that InCl_3 is not present in a significant amount. The qualitative nature of the equilibrium gas phase composition in the source zone is not altered by the change of process parameters within the range of this study.

The group III molar ratio, $\text{Ga}/(\text{Ga}+\text{In})$, in the vapor phase is important, since it is strongly related to the composition of deposited $\text{Ga}_x\text{In}_{1-x}\text{As}$. This ratio is easily obtained from the equilibrium calculation by calculating the total number of moles of vapor species containing gallium divided by the total number of moles of vapor species containing gallium and indium. Figure 2-3 shows the variation of this ratio versus the gallium content in the liquid alloy ($x_{\text{Ga}}(\text{l})$). As expected, the gas phase $\text{Ga}/(\text{Ga}+\text{In})$ ratio strongly depends on the source alloy composition. The results depicted in Figure 2-3 were achieved using three different liquid solution models:

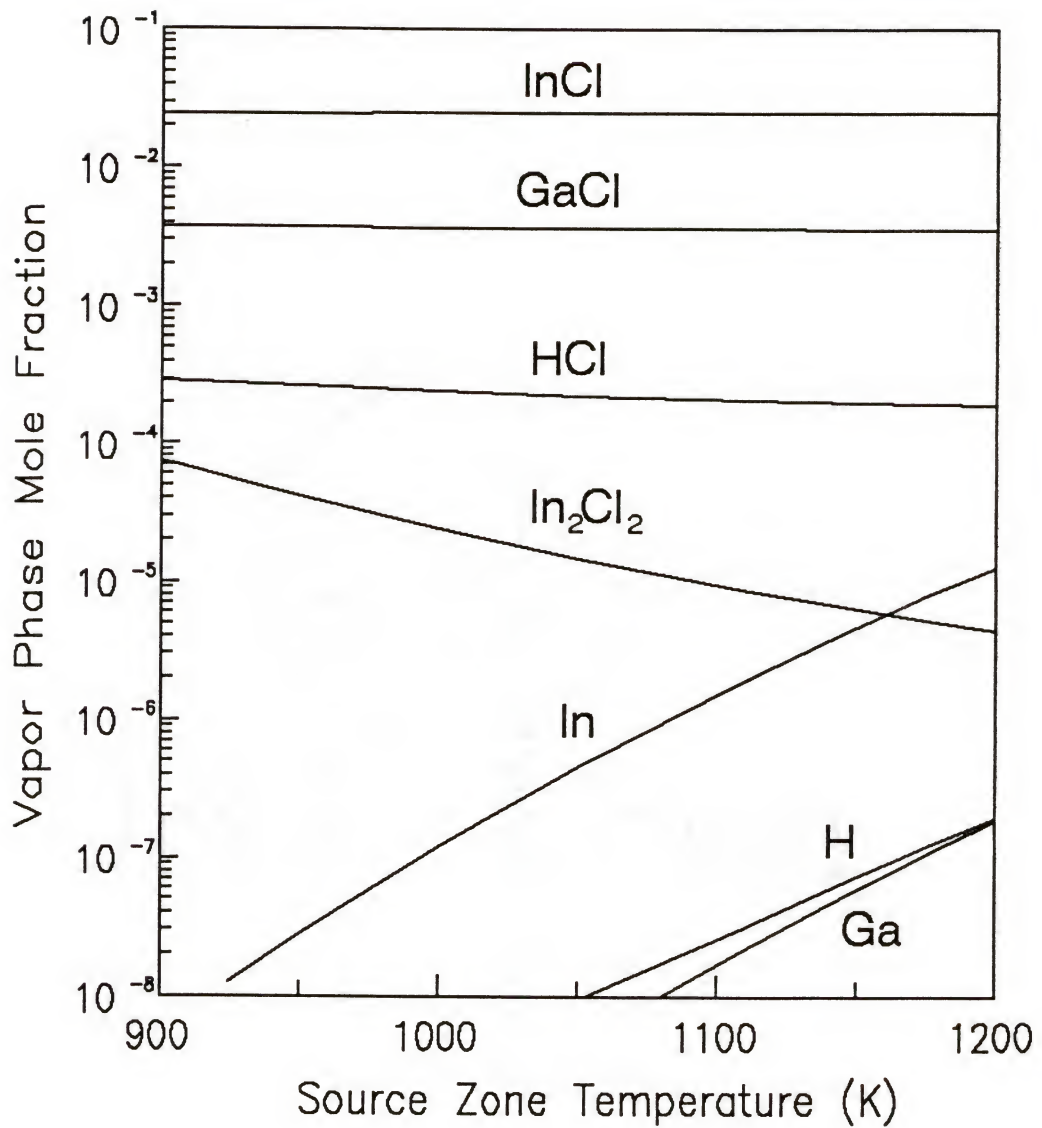


Figure 2-2: Equilibrium gas phase composition in the source zone versus the source zone temperature: $x_{\text{Ga}}(\text{l}) = 0.0869$; $\text{Cl}/\text{H} = 1.48 \times 10^{-2}$; $P_t = 1 \text{ atm.}$; Redlich-Kister liquid solution model.

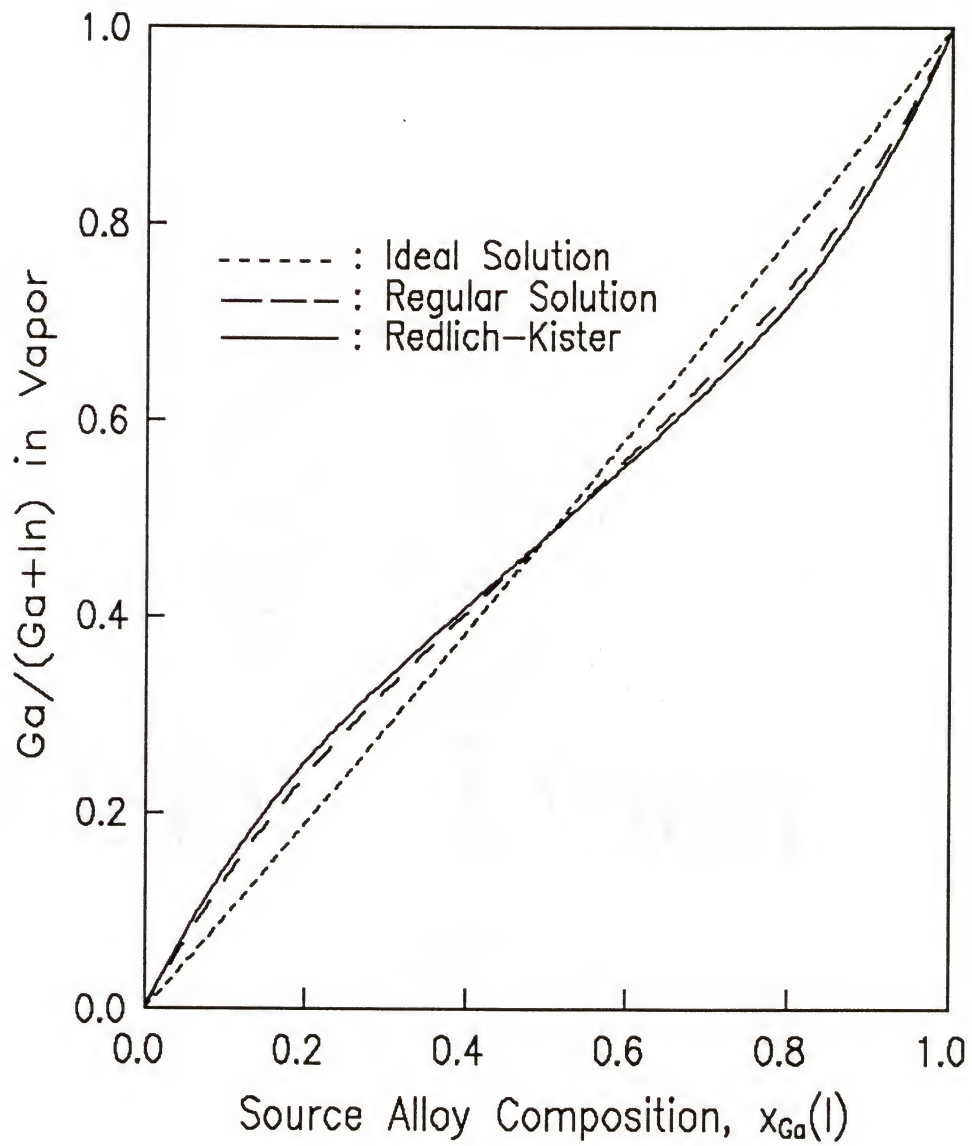


Figure 2-3: The vapor phase $\text{Ga}/(\text{Ga}+\text{In})$ molar ratio of the source zone versus the Ga content in the source alloy. Different liquid solution models are compared:
 $T_s = 838^\circ\text{C}$; $\text{Cl}/\text{H} = 1.48 \times 10^{-2}$; $P_t = 1 \text{ atm}$.

(1) The ideal solution model assumes the random mixing of Ga and In and zero enthalpy of mixing. Therefore, the activity coefficient of Ga in the liquid alloy is unity,

$$\ln\gamma_{\text{Ga}} = 0 \quad (2-2)$$

(2) The regular solution model assumes the random mixing of Ga and In, but an interaction between Ga and In exists. The activity coefficient of Ga is given by,

$$\ln\gamma_{\text{Ga}} = \Omega(1-x_{\text{Ga}})^2/RT \quad (2-3)$$

where Ω is the interaction coefficient between Ga and In. A value of 1066 cal/mol was used in the calculation as suggested from the fit of phase diagram data by Panish and Ilegems[49].

(3) The Redlich-Kister solution model was recently used by Anderson and Ansara[50] to optimize the Ga-In phase diagram and thermochemical property data. The activity coefficient of Ga takes the following form with the estimated parameter values,

$$\ln\gamma_{\text{Ga}} = [4450 + T(1.19185 + 0.25943 (3 - 4 (1-x_{\text{Ga}}))))](1-x_{\text{Ga}})^2/RT \quad (2-4)$$

As shown in Figure 2-3, the ideal solution model produces a gallium content in the gas phase slightly less than that in the liquid phase, whereas the regular solution model and the Redlich-Kister solution model produce a gallium content in the gas phase greater than that in the liquid phase for $x_{\text{Ga}}(\text{l}) < 0.5$ and less than that in the liquid phase for $x_{\text{Ga}}(\text{l}) > 0.5$. This is because the last two models calculate the gallium activity coefficient for $x_{\text{Ga}}(\text{l}) < 0.5$ greater than unity, thus the gallium yield is higher than the value calculated with the ideal model. The same effect is observed for indium when $x_{\text{Ga}}(\text{l}) > 0.5$. Around $x_{\text{Ga}}(\text{l}) = 0.20$, there is a 6% difference between the equilibrium gas phase Ga/(Ga+In) ratio calculated with the Redlich-Kister solution model and that with the ideal solution model. As discussed later, the solid composition in $\text{Ga}_x\text{In}_{1-x}\text{As}$ near the lattice matched value is very sensitive to the Ga/(Ga+In)

ratio exiting the source zone. This difference in $\text{Ga}/(\text{Ga}+\text{In})$ ratio is the largest one compared with the difference caused by changing the source zone operating parameters such as source zone temperature, Cl/H ratio, and total pressure, which was typically less than 2%. The small effect of source zone process parameters on this ratio was due to the almost complete conversion of HCl into group III metal chlorides. This fact alone shows the importance of selecting the right solution model for accurate equilibrium calculations. The Redlich-Kister solution model with the parameters given by Anderson and Ansara[50] was found to represent very closely the thermodynamic properties of the liquid $\text{Ga}_x\text{In}_{1-x}$ solution, therefore it was used for the source zone equilibrium calculation.

2.3.3 Deposition Zone Calculation

In the mixing zone, the vapor species generated in the source zone mix with AsH_3/H_2 and excess HCl and are transported to the deposition zone where the pseudobinary $\text{Ga}_x\text{In}_{1-x}\text{As}$ is deposited. The chemical system is constituted by five elements (Ga , In , As , Cl , and H) which form species in two phases (vapor and $\text{Ga}_x\text{In}_{1-x}\text{As}$ solid solution). Total pressure (P_1) was fixed at 1 atm and the other process parameters (*i.e.*, deposition temperature (T_d), inlet mole fraction of AsH_3 ($x_{\text{AsH}_3}^\circ$) and excess HCl ($x_{\text{HCl}}^{\text{add}}$)) were varied. Equilibrium calculations have been performed by using the elemental abundance determined from the results of the source zone calculation and by adding the required amount of arsine, hydrogen, and excess hydrogen chloride.

Figure 2-4 shows the composition of the gas phase in equilibrium with the $\text{Ga}_x\text{In}_{1-x}\text{As}$ solid solution ($x_{\text{GaAs}} = 0.37 - 0.77$) as a function of deposition temperature with the following process parameters: source alloy composition of 8.69 at.% Ga , source zone Cl/H ratio of 0.50×10^{-2} ($x_{\text{HCl}}^\circ = 2.4 \times 10^{-3}$; 10 sccm of HCl in 1000 sccm of H_2), and inlet mole fraction of AsH_3 of 3.4×10^{-3} (14 sccm of AsH_3 in total flow rate of 4200 sccm). Excess HCl was not added in this case. The main chloride species are InCl , GaCl , and HCl . The mole fraction of

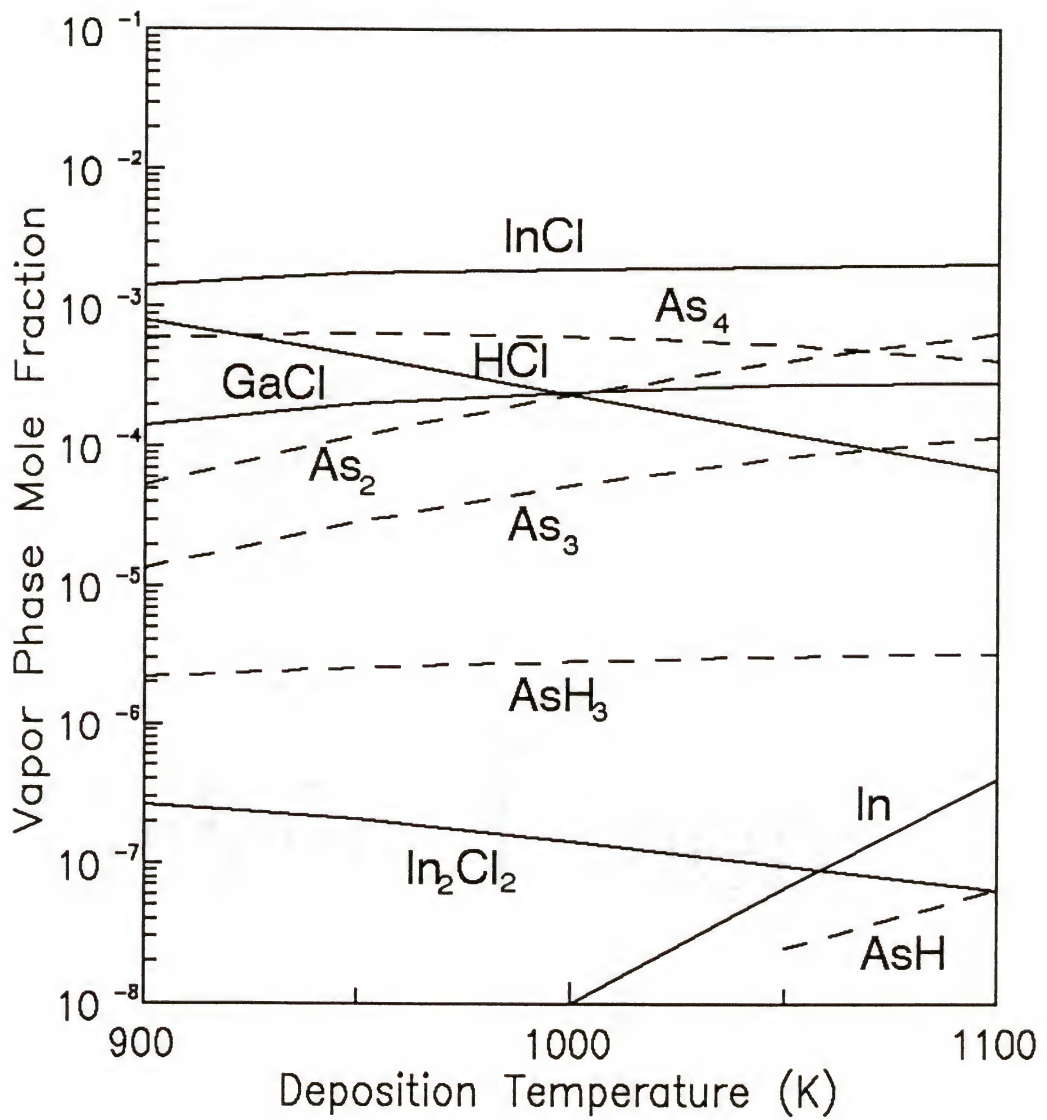


Figure 2-4: Equilibrium gas phase composition in the deposition zone versus deposition temperature: $x_{\text{Ga}}(\text{l}) = 0.0869$; $P_1 = 1 \text{ atm}$; $x_{\text{HCl}}^{\circ} = 2.4 \times 10^{-3}$; $x_{\text{AsH}_3}^{\circ} = 3.4 \times 10^{-3}$; strictly regular solution model with $\Omega = 3096 \text{ cal/mol}$.

InCl is obviously much higher than GaCl because GaAs is more easily deposited than InAs. The Gibbs energy of formation of GaAs at the typical deposition temperature from the monochloride is approximately 25 kJ/mol more negative than the value for InAs[48]. In_2Cl_2 is the only other chloride appearing in a noticeable amount ($> 10^{-8}$). The HCl partial pressure decreases when the deposition temperature increases, indicating that the deposition yield decreases. The main arsenide species are As_4 and As_2 with a small amount of As_3 and AsH_3 . It appears that arsine is almost completely decomposed at equilibrium.

The $\text{Ga}_x\text{In}_{1-x}\text{As}$ alloy is a pseudobinary solid solution with miscibility of GaAs and InAs in the solid state. Calorimetric and vapor pressure studies[48] indicate there is a miscibility gap in the solid solution in the composition range $0.27 < x_{\text{GaAs}} < 0.75$ at 950 K. Nevertheless, VPE or LPE experiments have demonstrated it is possible to grow $\text{Ga}_x\text{In}_{1-x}\text{As}$ solid solution of $x_{\text{GaAs}} = 0.47$ in the temperature range $900 < T_d < 1050$ K without indication of an immiscibility problem. Optimization of phase diagram data using solution models which assume total miscibility of the solid solution (for $T > 900$ K) have been able to describe quite successfully the solidus curve in the phase diagram of $\text{Ga}_x\text{In}_{1-x}\text{As}$.

Four different solid solution models are tested for the deposition zone calculation and compared with the experimental data: (1) the ideal solution model, (2) the strictly regular solution model, (3) the quasichemical solution model, and (4) the short range order parameter (SROP) model.

(1) The ideal solution model assumes total randomness of Ga and In on the sublattice ($\Delta S^{\text{ex}} = 0$) and zero enthalpy of mixing ($\Delta H^{\text{ex}} = 0$). The enthalpy between unlike pairs is the arithmetic average of the enthalpies of like pairs. Thus, the activity of GaAs is equal to the mole fraction of GaAs which gives a GaAs activity coefficient of unity[18],

$$\ln \gamma_{\text{GaAs}} = 0 \quad (2-5)$$

(2) The strictly regular solution model assumes random mixing of GaAs and InAs ($\Delta S^{\text{ex}} = 0$), but the interaction between neighboring unlike pairs exists. The excess enthalpy takes the form[48],

$$\Delta H^{\text{ex}} = \Omega x_{\text{GaAs}}(1-x_{\text{GaAs}}) \quad (2-6)$$

which is symmetric with respect to $x_{\text{GaAs}} = 0.5$. The activity coefficient of GaAs takes the form,

$$\ln \gamma_{\text{GaAs}} = \Omega(1-x_{\text{GaAs}})^2/RT \quad (2-7)$$

Ω is the interaction parameter between GaAs and InAs, and it can be a function of temperature (an assumption used in the simple solution model) or a function of composition (an assumption used in the generalized regular solution model). The strictly regular solution model limits the interaction parameter to be a constant value. The value of the interaction parameter is determined either by empirical models or by optimizing phase diagram and thermochemical data. Stringfellow[51] developed a delta lattice parameter (DLP) model to describe the enthalpy of mixing of semiconductor materials. In this model, the bonding energy is assumed to be approximately linearly dependent on the bandgap energy. The work of Philips and Van Vetchen[52] suggests that the average bandgap energy (E_g) is proportional to $a_o^{-2.5}$, where a_o is the lattice parameter of the III-V compound semiconductor. The DLP model proposes that the enthalpy of atomization H_{at} (and the bonding energy) can be approximated by

$$H_{\text{at}} = k a_o^{-2.5} \quad (2-8)$$

where k is the proportionality constant. This model gives the enthalpy of mixing nonstrictly symmetric to $x_{\text{GaAs}} = 0.5$, but Stringfellow[51] further assumed that the enthalpy of mixing is well described by the strictly regular solution. The Ω parameters are then directly proportional to the lattice parameters. For $\text{Ga}_x\text{In}_{1-x}\text{As}$ the obtained Ω parameter is,

$$\Omega_{\text{DLP}} = 2815 \text{ cal/mol} \quad (2-9)$$

Tmar[48] optimized the interaction parameter (Ω) by taking into account his critical review of the published phase diagram data and his activity measurement of the solid solution. The result of Tmar's assessments suggests the value of

$$\Omega = 3096 \text{ cal/mol} \quad (2-10)$$

These two different values were compared in the calculation and produced basically the same trend in the deposited solid solution composition, but Tmar's value better represented the experimental data of this study, therefore, it is selected for the calculation.

(3) The quasichemical solution model[53] discards the random distribution assumption by taking into account the preferential occupation of lattice sites by short range clustering of like pairs. The short range clustering occurs because it reduces the number of neighboring unlike pairs, thus decreasing the enthalpy of mixing and the total Gibbs energy. Onabe[54] described the second nearest neighbor pair distribution as a function of the (first) nearest neighbor pair distribution on the basis of a Bethe lattice model, neglecting the quasichemical nature of the second nearest neighbor pair distribution, and developed the first-order quasichemical solution model for quaternary III-V compound system of the $A_xB_{1-x}C_yD_{1-y}$ type. In the pseudobinary limit, the derived activity coefficient of GaAs takes the following form[55]:

$$\gamma_{\text{GaAs}} = \left[\frac{\beta - 1 + 2x_{\text{GaAs}}}{x_{\text{GaAs}}(\beta + 1)} \right]^{\left(\frac{z}{2}\right)} \quad (2-11)$$

with

$$\beta = [1 + 4x_{\text{GaAs}}(1 - x_{\text{GaAs}})(\eta^2 - 1)]^{0.5} \quad (2-12)$$

and

$$\eta = \exp\left(\frac{\Omega}{zRT}\right) \quad (2-13)$$

where the coordination number $z = 4$, and the interaction parameter $\Omega = 2800$ cal/mol[55].

(4) The short range order parameter (SROP) model used by Marboeuf and Guillaume[56] introduces the notion of clustering tendency in the III-V alloy by using the theory developed by Averbach[57]. In this model the interaction parameter (Ω) is a separable function of composition (x) and temperature (T).

$$\Omega = u + j(x) + g(T) \quad (2-14)$$

where u is some constant; j and g are arbitrary functions.

The short range order parameter is defined as

$$\alpha = 1 - \frac{P_1}{x_1} \quad (2-15)$$

where P_1 is the probability of finding the atom 1 as a nearest neighbor of atom 2, and x_1 is the concentration of atom 1 in the mixture. After developing the entropy of mixing by a statistical treatment with some adequate simplifications, Averbach[57] obtained the following expressions:

$$\Delta H^m = zN_o x_1 x_2 (1 - \alpha) [u + j(x)] \quad (2-16)$$

and

$$\Delta S^m = -k_B N_o (1 - \alpha) (x_1 \ln x_1 + x_2 \ln x_2) - zN_o x_1 x_2 (1 - \alpha) g(T) \quad (2-17)$$

where

$$\alpha = 2x_1 x_2 \frac{\Omega}{k_B N_o T} \quad (2-18)$$

N_o is the total number of atoms in unit volume, and k_B is the Boltzmann constant. These expressions have three parameters which cannot be immediately obtained from thermodynamic data. In III-V solid solutions, however, Ω is often quasiconstant, decreasing the number of parameters to one in the Averbach model. Marboeuf and Guillaume[56] assumed that the III-V lattice undergoes a very weak thermal dilatation, which suggest the enthalpy of mixing is weakly temperature dependent. In other words, the temperature dependence of the parameter $g(T)$ is neglected in equation (2-17). Then, the Stringfellow's DLP model[51] can be used in the ΔH^m expression and the excess entropy is reduced to the excess configurational entropy:

$$\Delta H^m = \Omega_{DLP} x_1 x_2 \quad (2-19)$$

and

$$\Delta S^m = -(1 - \alpha)(x_1 \ln x_1 + x_2 \ln x_2) \quad (2-20)$$

where

$$\alpha = 2x_1 x_2 \frac{\Omega_{DLP}}{zRT} \quad (2-21)$$

The derivation of the activity coefficient of GaAs is now straightforward, and it takes the following form:

$$\ln \gamma_{GaAs} = \frac{\Omega_{DLP}(1 - x_{GaAs})^2}{RT} \left[1 + \frac{2}{z}(2x_{GaAs} - 1) \ln(1 - x_{GaAs}) - \frac{4x_{GaAs}}{z} \ln x_{GaAs} \right] \quad (2-22)$$

Figure 2-5 shows the strong dependence of the deposited $Ga_xIn_{1-x}As$ composition on the Ga content in the source alloy. The experimental process parameters used for the calculation were the total pressure (P_t) of 1 atm, deposition temperature (T_d) of 700 °C, and inlet mole fractions of HCl (x_{HCl}^o) and AsH₃ ($x_{AsH_3}^o$) of 7.2×10^{-3} and 3.4×10^{-3} , respectively. The calculated results with four different solid solution models are shown with the

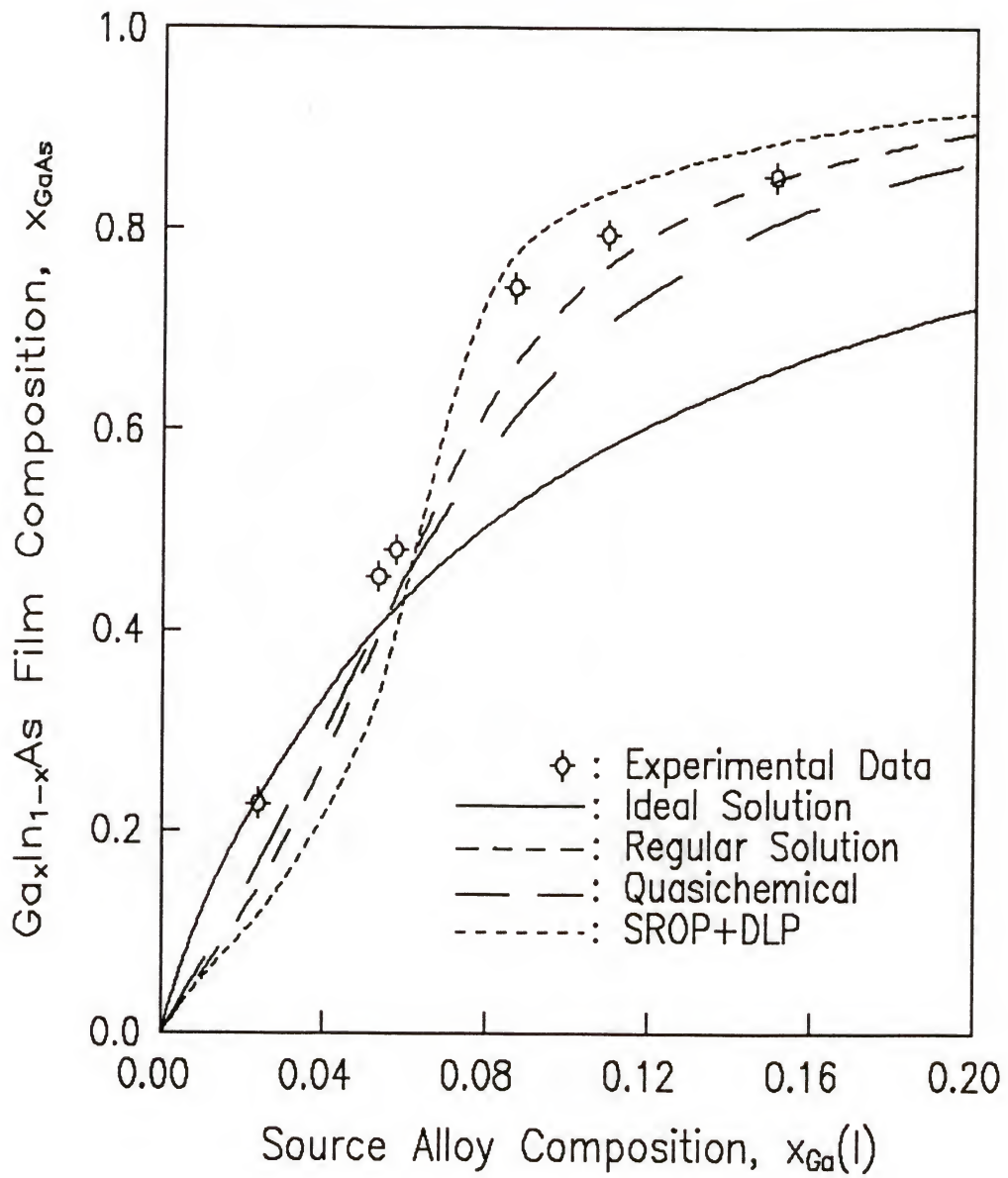


Figure 2-5: Calculated $\text{Ga}_x\text{In}_{1-x}\text{As}$ composition versus the Ga content in the source alloy: comparison between different solid solution models ($T_d = 700^\circ\text{C}$; $P = 1\text{ atm}$; $x_{\text{HCl}}^\circ = 7.2 \times 10^{-3}$; $x_{\text{AsH}_3}^\circ = 3.4 \times 10^{-3}$).

experimental data. Interestingly, all the solution models except the ideal model represent the experimental data reasonably well, considering the non-equilibrium factors involved in the experimental data. It must be mentioned that the difference in calculated solid solution compositions by using the different non-ideal solution models was much smaller than the difference by using the different set of thermochemical data for indium chlorides, gallium chlorides, GaAs(s), and InAs(s). The calculation with the old data set[37] could not represent the experimental data of this study very well even though the general trend in solid solution composition was the same.

The SROP model shows the largest deviation from the ideal model, and the quasichemical solution model and the strictly regular solution model with $\Omega = 3096$ cal/mol show a very similar behavior. The main difference between the last two models is that the quasichemical model assumes a nonrandom distribution of the solid solution which is manifested by a positive excess entropy. But the interaction parameter (Ω) of the quasichemical model is smaller than that of the regular solution model. These two effects seem to cancel each other. The different models chosen to describe the solid solution mainly affect the shape (steepness) of the curve $x_{\text{GaAs}} = f [x_{\text{Ga}}(\text{l})]$, and the nonrandom models are not very far from the strictly regular solution model with $\Omega = 3096$ cal/mol. Both the strictly regular solution model with $\Omega = 3096$ cal/mol and the quasichemical solution model were used for the equilibrium calculation of deposition zone to study the solid solution compositions as a function of process parameters, and the results are shown with the experimental data.

2.4 Results and Discussion

2.4.1 Parametric Studies

The growth rate of $\text{Ga}_x\text{In}_{1-x}\text{As}$ was studied as a function of deposition temperature in the range 674 to 719 °C, while maintaining other process parameters at the base values. An

Arrhenius plot of growth rate is shown in Figure 2-6. The growth rate shows two distinct segments with temperature: a strongly temperature-dependent growth rate at low temperatures and a weakly temperature-dependent growth rate at higher temperatures. At the lower temperatures, the apparent activation energy determined for the deposition of $\text{Ga}_x\text{In}_{1-x}\text{As}$ from a source alloy of 8.69 at.% Ga was 188 kJ/mol. This value is in close agreement with the values of 184 kJ/mol and 180 kJ/mol reported by Hyder *et al.*[58] and by Erstfeld and Quinlan[26], both on (100) InP substrates. These apparent activation energies are similar to those reported for the homoepitaxy of GaAs on (100) GaAs (203.8 kJ/mol[59] and 200.0 kJ/mol[60]), while the reported apparent activation energy for homoepitaxy of InAs has a higher value of 230 kJ/mol[61]. Since the growth rate is nearly independent of deposition temperature at higher temperatures, the deposition is apparently limited by mass transfer. Figure 2-6 shows that the growth is primarily limited by chemical reaction at the base temperature of 700 °C.

The change in the composition of the deposited layer with the deposition temperature is shown in Figure 2-7. The Ga content decreases with increasing temperatures for deposition in the reaction-limited regime (low growth temperatures). This observation is consistent with the lower apparent activation energy reported for homoepitaxial deposition of GaAs than for InAs[59-61]. The observed change in the film composition for growth in the mass transport limited regime (high growth temperatures) is smaller. The trends in the film composition as a function of the deposition temperature are opposite to those observed by Kordos *et al.*[24] and Hyder *et al.*[58]. Both the experimental results and equilibrium analysis of Kordos *et al.*[24] indicate the Ga content increases with increasing deposition temperatures. Hyder *et al.*[58] reported HCl flow rates in the In source boat required to maintain a constant film composition of $\text{Ga}_{0.47}\text{In}_{0.53}\text{As}$ at various growth temperatures. Their results show that an increase in the HCl flow rate was required with increasing growth temperatures, suggesting the Ga content increases with increasing deposition temperatures. The equilibrium analysis of this study using

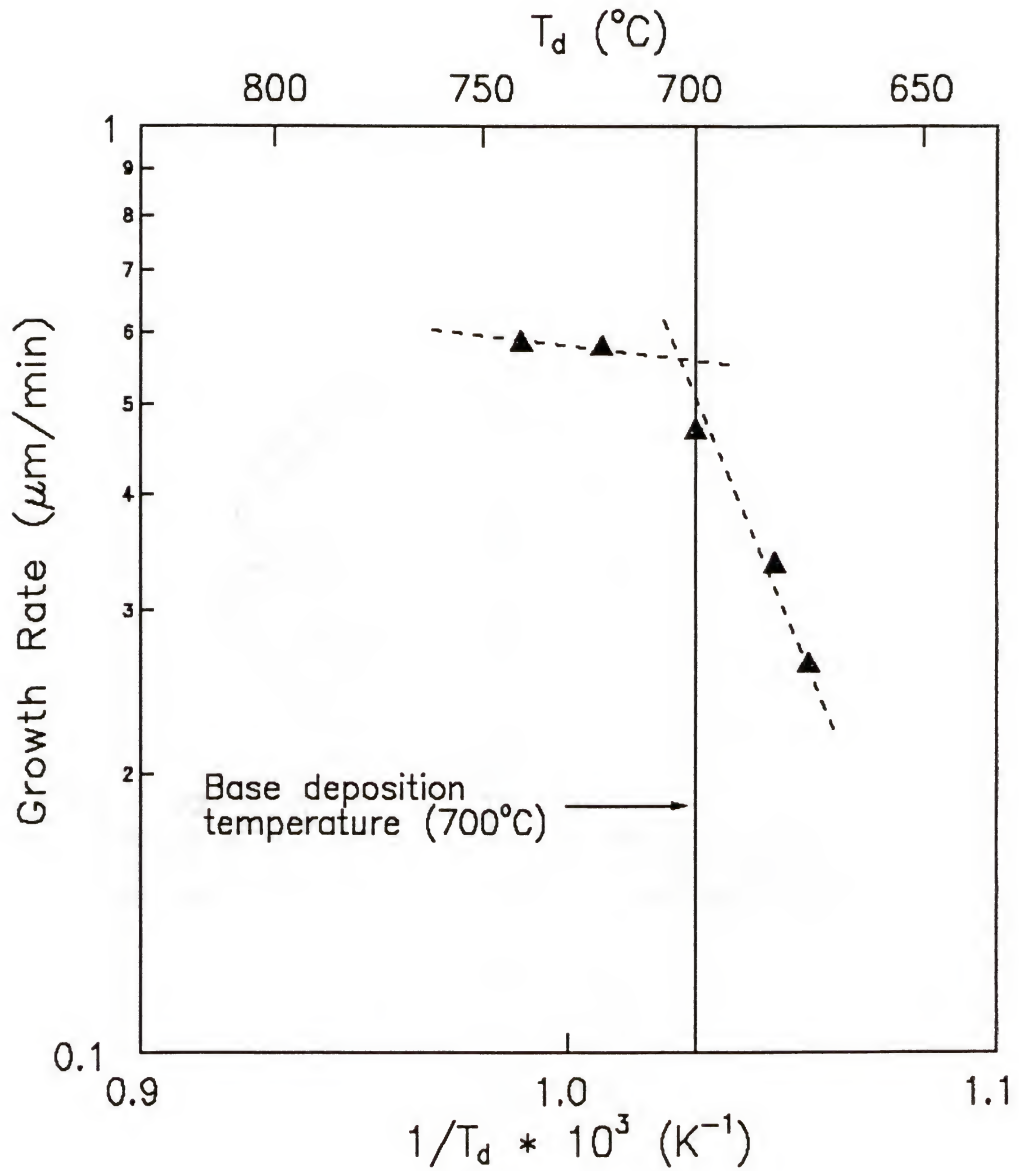


Figure 2-6: Arrhenius plot of growth rate of $\text{Ga}_x\text{In}_{1-x}\text{As}$ at $x_{\text{Ga}}(\text{l}) = 0.0869$, $x_{\text{HCl}}^\circ = 0.0024$, $x_{\text{AsH}_3}^\circ = 0.0034$, and total flow rate = 4200 sccm. The low temperature apparent activation energy is 188 kJ/mol.

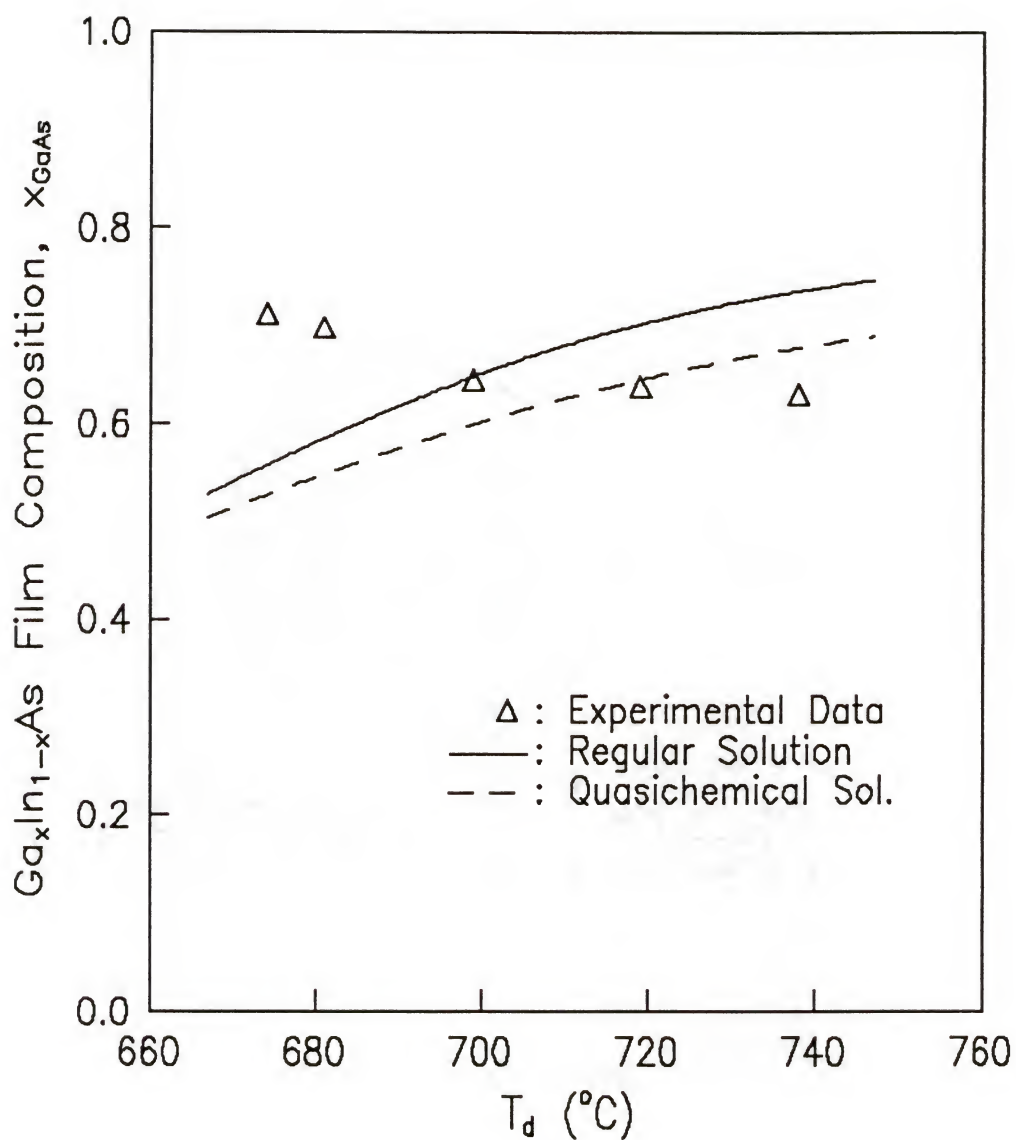


Figure 2-7: The film composition of $\text{Ga}_x\text{In}_{1-x}\text{As}$ as a function of deposition temperature at $x_{\text{Ga}}(\text{l}) = 0.0869$, $x_{\text{HCl}}^{\circ} = 0.0024$, $x_{\text{AsH}_3}^{\circ} = 0.0034$, and total flow rate = 4200 sccm.

two different non-ideal solid solution models also shows the same trend. This trend is a result of the enthalpy of formation of GaAs being more negative than the enthalpy of formation of InAs (Table 2-1). According to the Van't Hoff equation[62], an increasing temperature should favor the deposition of GaAs at equilibrium. The reason for these differences is not apparent, though the chloride VPE study by Coronado *et al.*[29] at film compositions close to the lattice matched value lends support to both of these observed trends. These investigators reported a broad minimum for the Ga content at a deposition temperature near 675 °C for an alloy source composition of 7 at.% Ga.

The influence of the source alloy composition on the film composition is shown in Figure 2-8. The plot shows that an alloy composition of 5.8 at.% Ga is necessary for the preparation of $\text{Ga}_{0.47}\text{In}_{0.53}\text{As}$ at these operating conditions. The Ga mole fraction in the epitaxial layer is considerably higher than the mole fraction of Ga in the alloy source. This behavior is expected on the basis of thermodynamics since the Gibbs energy of formation of InAs at the growth temperature from the monochloride is approximately 25 kJ/mol more positive than the value for GaAs[48]. Positive deviations from ideal-solution behavior in the In-rich alloy solution[50] further contribute to a distribution coefficient greater than one. The results of an equilibrium analysis using both the strictly regular solution model and the quasichemical solution model for the solid solution are shown in Figure 2-8. The calculated compositions are seen to accurately reproduce the trend in this intensive variable. The slope of the equilibrium curve is near its maximum value at the lattice-matched composition indicating this composition is very sensitive to changes in the alloy source concentration.

Figure 2-8 shows the results of several other investigators using an alloy source. The general trends are similar but the alloy composition required for lattice-matched growth varies between 3.2 to 12.2 at.% Ga. These results suggest that the composition of the film is influenced by the operating parameters and reactor design. In this study, for example, lattice-matched $\text{Ga}_{0.47}\text{In}_{0.53}\text{As}$ epitaxial layers could be grown with both 5.35 and 8.69 at.% Ga alloys

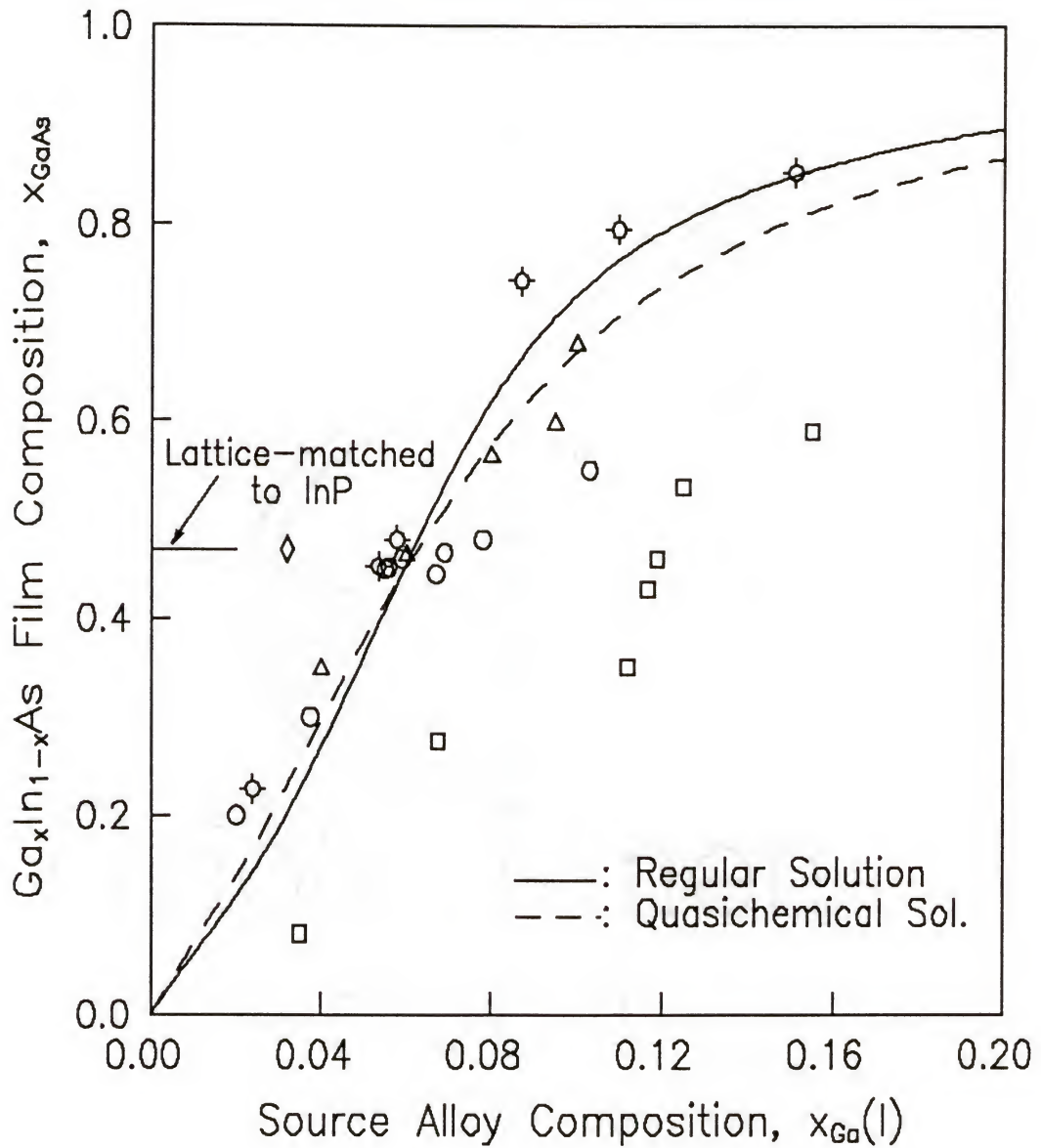


Figure 2-8: The film composition of $\text{Ga}_x\text{In}_{1-x}\text{As}$ as a function of the Ga mole fraction in the source alloy at $T_d = 700^\circ\text{C}$, $x_{\text{HCl}}^\circ = 0.0072$, and $x_{\text{AsH}_3}^\circ = 0.0034$. \odot , this study; \triangle , Jacobs *et al.*[28]; \circ , Kordos *et al.*[24]; \square , Erstfeld and Quinlan[26]; \diamond , Chatterjee *et al.*[25].

by adjustment of process parameters until 50% of the alloy source had been consumed. The optimum alloy composition for growth of a particular film composition should be based on other factors, such as photoelectrical properties. The observed differences in alloy composition required to grow lattice-matched layers among different investigators are consistent in sign when accounting for differences between stated operating conditions. Figure 2-9 shows that the growth rate decreases with increasing Ga mole fraction in the alloy source. This decrease is consistent with the growth rates reported for the separate binary compounds[59-61].

The effect of inlet AsH_3 mole fraction, $x_{\text{AsH}_3}^\circ$, on the composition and growth rate of the films grown from alloys containing 5.35 and 8.69 at.% Ga is shown in Figure 2-10 and Figure 2-11, respectively. The film composition (Figure 2-10) shows a small increase in InAs mole fraction and agrees with the results reported by several other investigators[63-66] as well as with the equilibrium analysis. The growth rate (Figure 2-11) increases slightly with increasing $x_{\text{AsH}_3}^\circ$. This result is also consistent with the prediction of an equilibrium analysis[67] which predicts an increase in the degree of supersaturation with increasing $x_{\text{AsH}_3}^\circ$.

The dependence of film composition on the inlet HCl mole fraction, x_{HCl}° , is shown in Figure 2-12, where the results for three different alloys, 15.10, 8.69, and 5.35 at.% Ga, are reported. The Ga content of the deposited layers increases with x_{HCl}° and exhibits a limiting value when x_{HCl}° is greater than 6×10^{-3} . The limiting film compositions of $\text{Ga}_x\text{In}_{1-x}\text{As}$ prepared from different alloy sources are $x_{\text{GaAs}} = 0.85, 0.74, \text{ and } 0.43$ for the alloy compositions 15.10, 8.69, and 5.35 at.% Ga, respectively. Increasing x_{HCl}° increases the group III transport rate and therefore the III/V ratio. The results shown in Figure 2-10 also represent changes in the III/V ratio. The direction of change in the film composition is in agreement between the results shown in Figure 2-10 and Figure 2-12, but the magnitude of the change is greater for variations in x_{HCl}° than $x_{\text{AsH}_3}^\circ$. A thermodynamic analysis predicts an increase of Ga in the deposited layer with increasing x_{HCl}° or equivalently Cl/H molar ratio. InCl is more stable than GaCl[47] and tends to remain in the vapor phase which increases the Ga content of $\text{Ga}_x\text{In}_{1-x}\text{As}$.

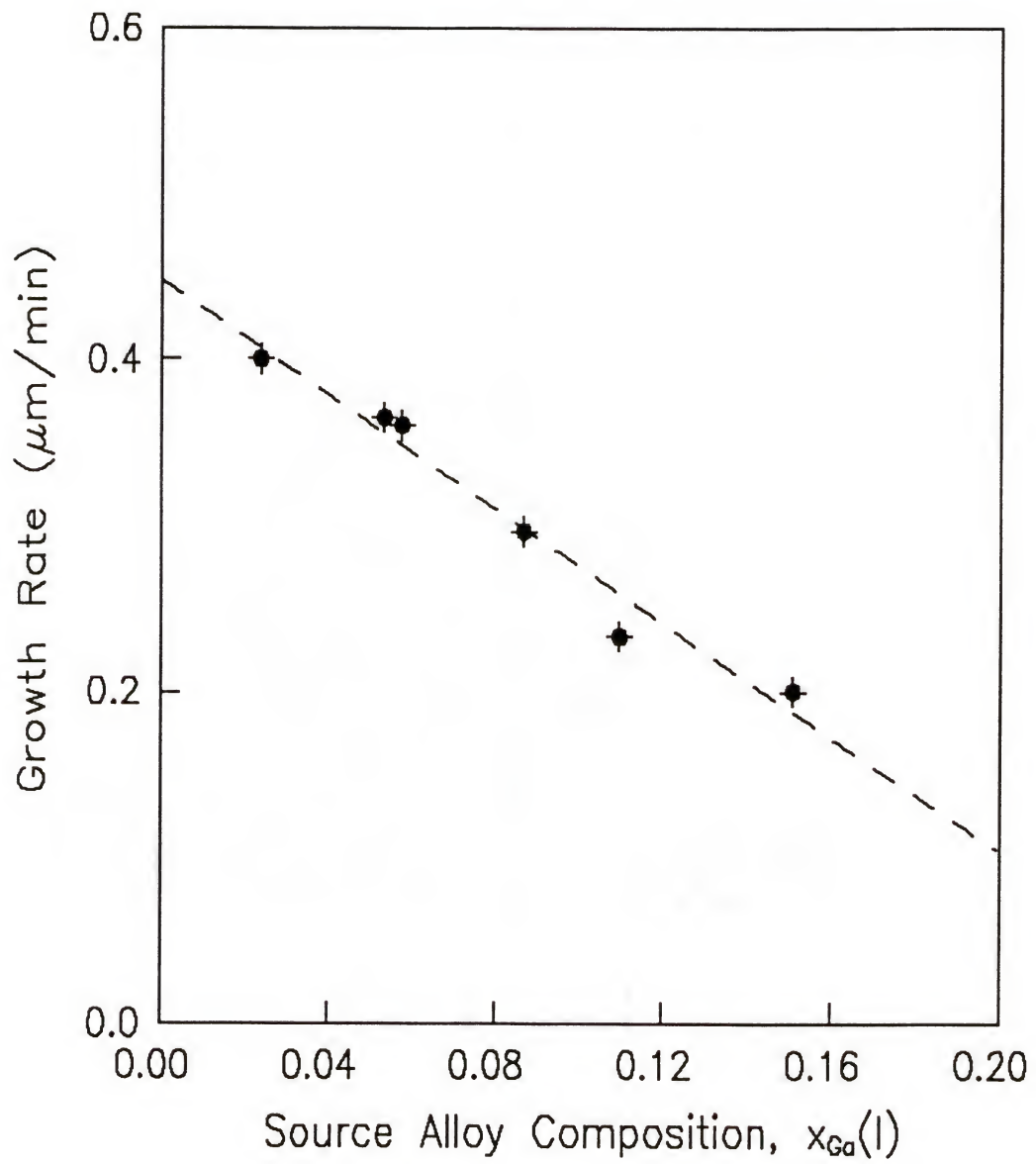


Figure 2-9: The growth rate of $Ga_xIn_{1-x}As$ as a function of the Ga mole fraction in the source alloy at $T_d = 700\text{ }^{\circ}C$, $x_{HCl}^o = 0.0072$, and $x_{AsH_3}^o = 0.0034$.

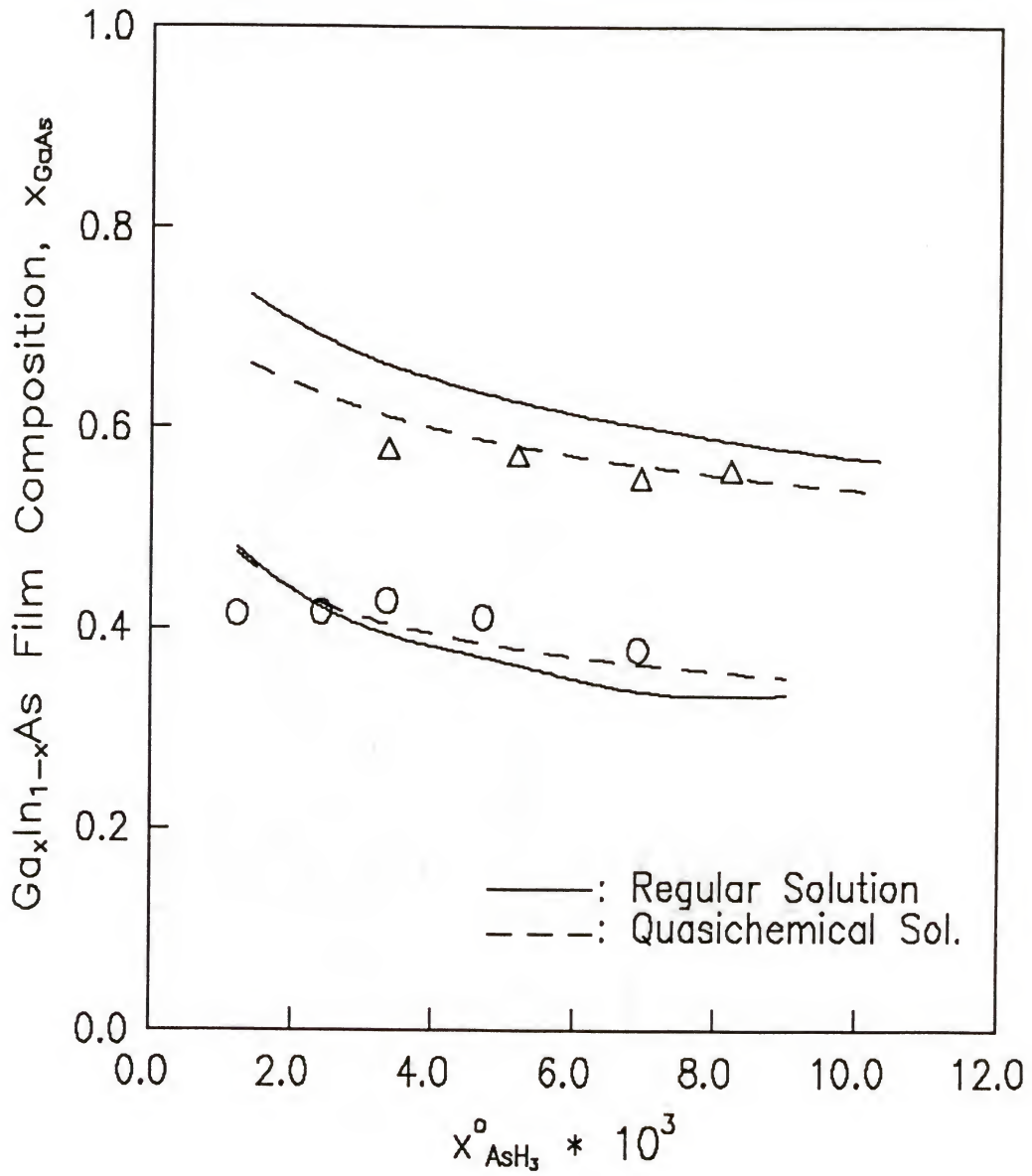


Figure 2-10: The film composition of $\text{Ga}_x\text{In}_{1-x}\text{As}$ as a function of inlet AsH_3 mole fraction. Deposition conditions: Δ , $T_d = 700^\circ\text{C}$, $x_{\text{Ga}}(l) = 0.0869$, $x_{\text{HCl}}^o = 0.0036$, total flow of $\text{H}_2 + \text{HCl}$ in the source = 523 sccm; O, $T_d = 700^\circ\text{C}$, $x_{\text{Ga}}(l) = 0.0535$, $x_{\text{HCl}}^o = 0.0072$, total flow of $\text{H}_2 + \text{HCl}$ in the source = 1045 sccm.

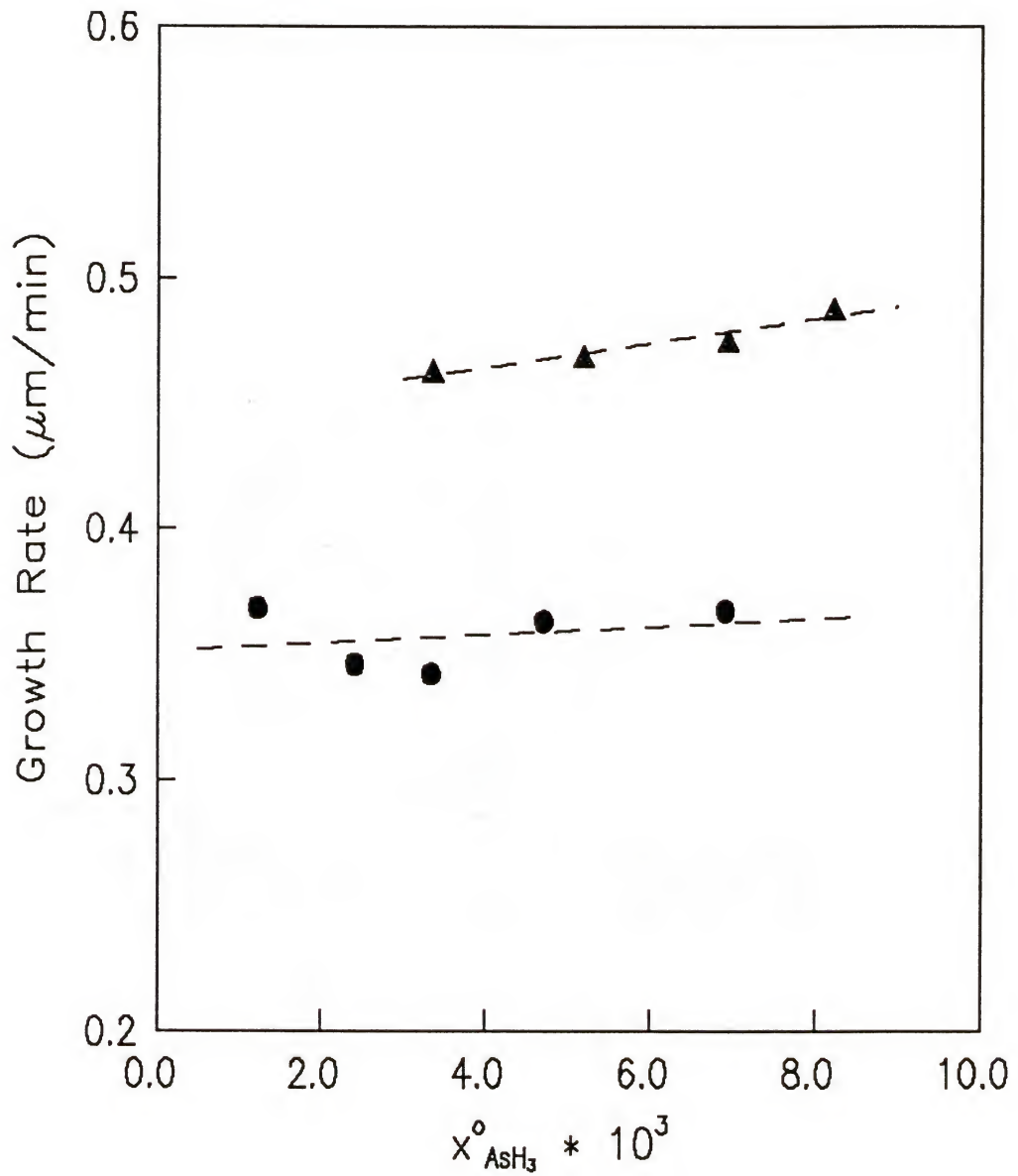


Figure 2-11: The growth rate of $\text{Ga}_x\text{In}_{1-x}\text{As}$ as a function of inlet AsH_3 mole fraction.

Deposition conditions: Δ , $T_d = 700^\circ\text{C}$, $x_{\text{Ga}}(\text{l}) = 0.0869$, $x_{\text{HCl}}^o = 0.0036$, total flow of $\text{H}_2 + \text{HCl}$ in the source = 523 sccm; \circ , $T_d = 700^\circ\text{C}$, $x_{\text{Ga}}(\text{l}) = 0.0535$, $x_{\text{HCl}}^o = 0.0072$, total flow of $\text{H}_2 + \text{HCl}$ in the source = 1045 sccm.

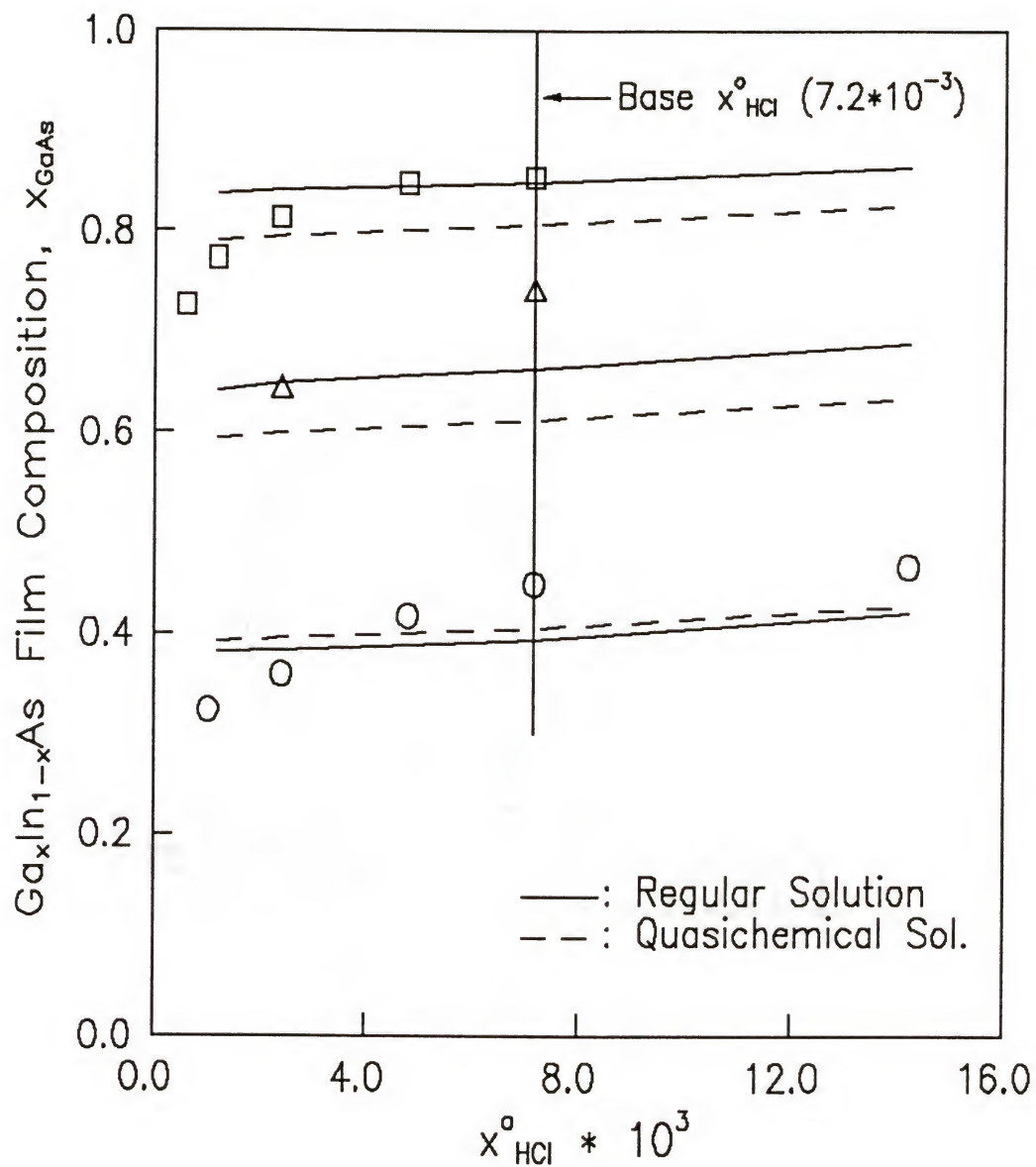


Figure 2-12: The film composition of $\text{Ga}_x\text{In}_{1-x}\text{As}$ as a function of inlet HCl mole fraction at $T_d = 700^\circ\text{C}$ and $x_{\text{AsH}_3}^o = 0.0033$. Source alloy compositions:

\square , $x_{\text{Ga}}(l) = 0.1510$; \triangle , $x_{\text{Ga}}(l) = 0.0869$; \circ , $x_{\text{Ga}}(l) = 0.0535$.

The large increase of Ga in the grown layer may also be related to a non-equilibrium conversion in the source zone which increases the amount of unreacted HCl in the deposition zone. The extra HCl in the deposition zone reduces the degree of supersaturation, which increases the Ga concentration in the film. This aspect is discussed in the following paragraphs.

The growth rate of $\text{Ga}_x\text{In}_{1-x}\text{As}$ as a function of inlet HCl mole fraction is shown in Figure 2-13. The growth-rate data exhibit a maximum for each of the three alloy compositions studied. The maxima occur at a III/V ratio of approximately one, corresponding to the stoichiometry of the film. The increase in growth rate at low values of inlet HCl mole fraction is the result of simply supplying more metal chlorides to the system. This is the region where the GaAs mole fraction is increasing in the film (Figure 2-12). At high values of inlet HCl mole fraction, the growth rate decreases as the III/V ratio increases, apparently first order in x_{HCl}^0 . This result is consistent with the explanation by Shaw[68] that the deposition rate of GaAs in the kinetically limited regime is controlled by competitive adsorption between metal chlorides, HCl, and arsenic species at As growth sites. Weyburne and Quinlan[64] also observed these phenomena in the growth of $\text{Ga}_x\text{In}_{1-x}\text{As}$ epitaxial layers. They suggested that above a threshold value of GaCl partial pressure, Langmuir adsorption of GaCl probably reaches saturation and growth depends on the dissociation of GaCl from the active arsenic sites.

The effect of adding excess HCl to the mixing zone on the film composition is shown in Figure 2-14. Injection of HCl to the mixing zone has been used to reduce Si background doping, reduce the growth rate, and eliminate wall deposition. The Ga content in the deposited layers increases slightly with increasing added HCl and eventually reaches a constant value. The gallium increase is more pronounced for films prepared from the source containing the smaller amount of Ga (5.35 at.% Ga). Quinlan and Erstfeld[27] and Buckley[66] have observed greater change in the Ga content of the film when HCl was added to the mixing zone.

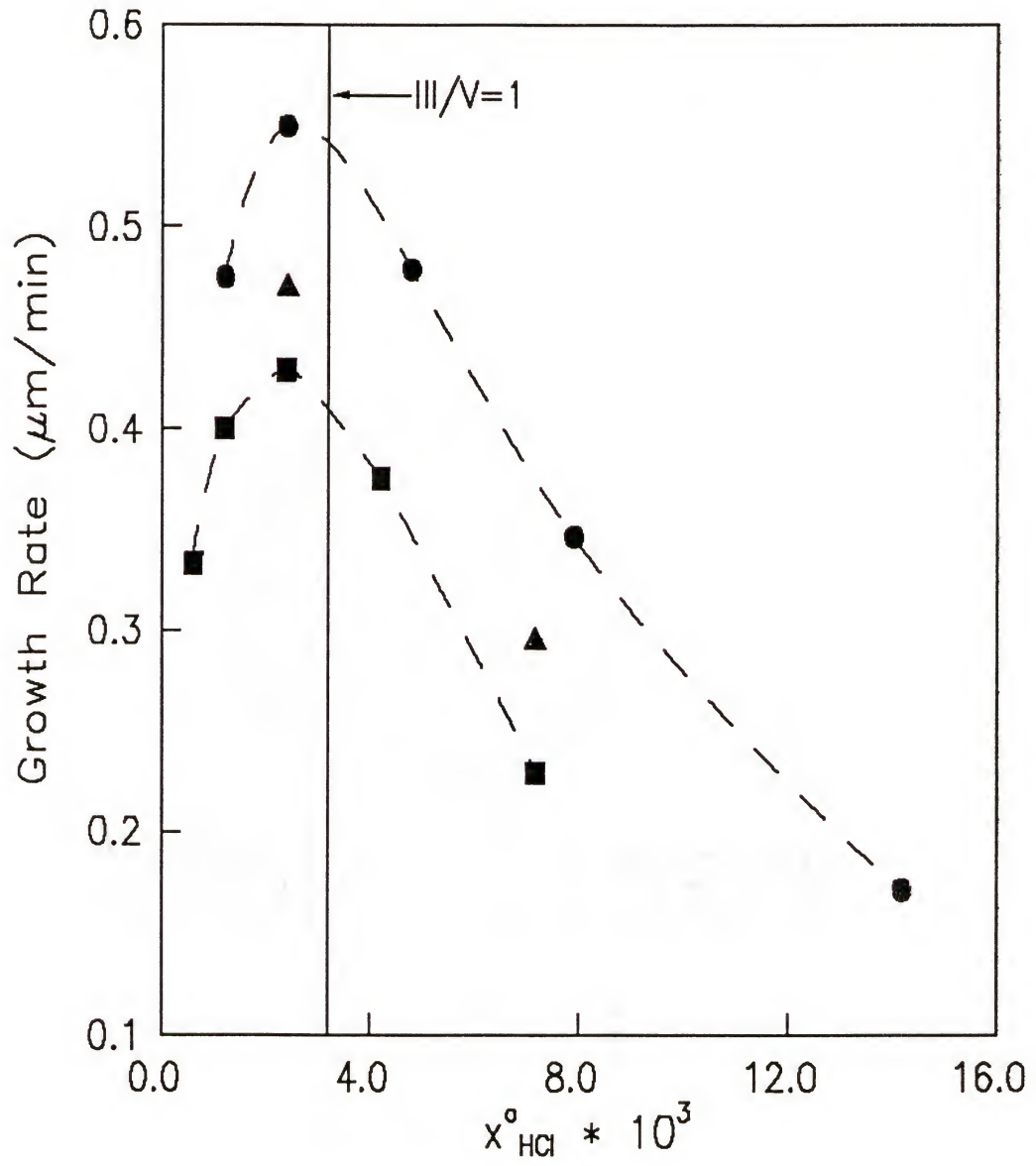


Figure 2-13: The growth rate of $\text{Ga}_x\text{In}_{1-x}\text{As}$ as a function of inlet HCl mole fraction at $T_d = 700^\circ\text{C}$ and $x_{\text{AsH}_3}^o = 0.0033$. Source alloy compositions:
 □, $x_{\text{Ga}}(\text{l}) = 0.1510$; △, $x_{\text{Ga}}(\text{l}) = 0.0869$; ○, $x_{\text{Ga}}(\text{l}) = 0.0535$.

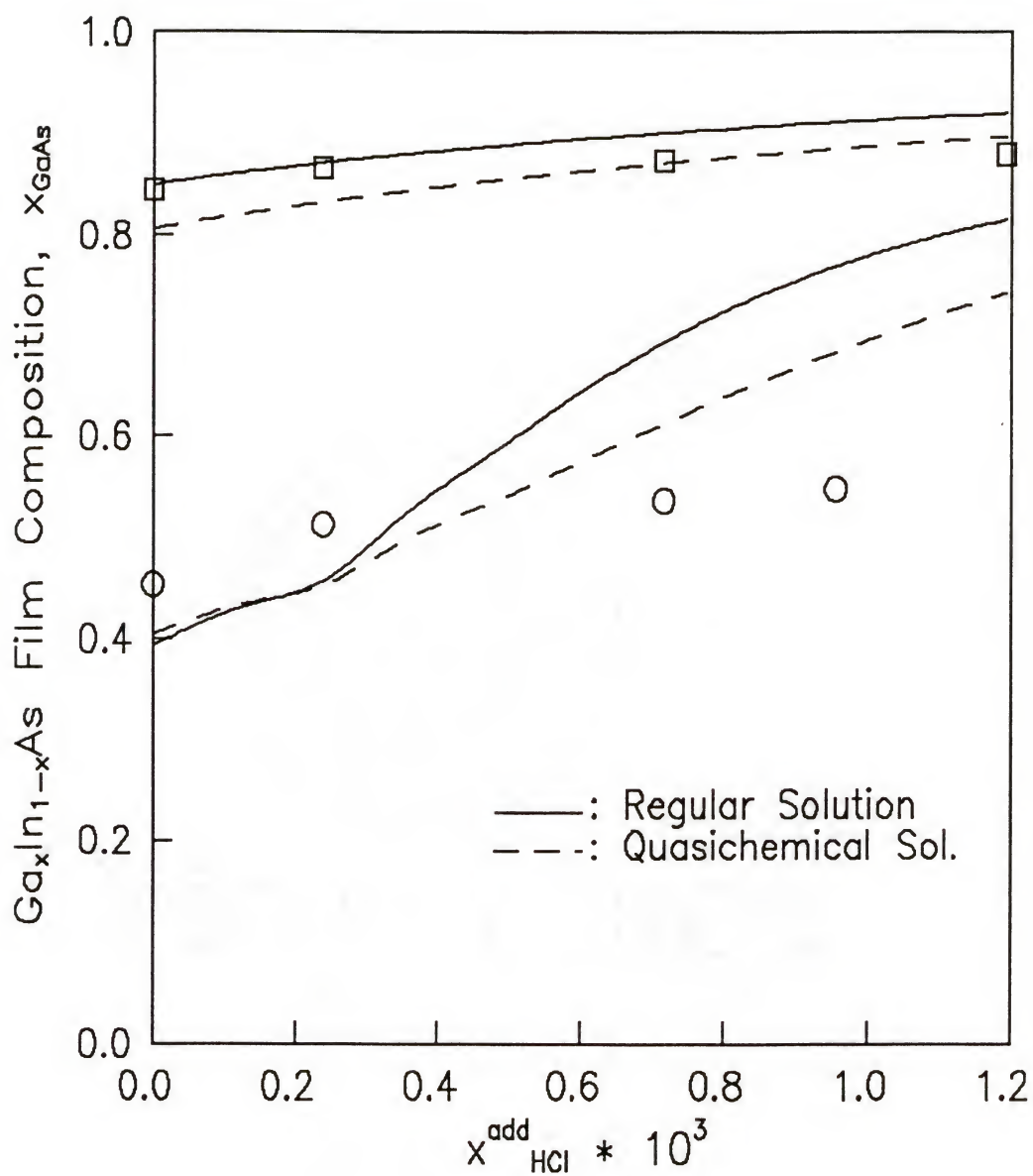


Figure 2-14: The film composition of $\text{Ga}_x\text{In}_{1-x}\text{As}$ as a function of added HCl mole fraction at $T_d = 700^\circ\text{C}$, $x_{\text{HCl}}^\circ = 0.0072$, and $x_{\text{AsH}_3}^\circ = 0.0033$. Source alloy compositions: \square , $x_{\text{Ga}}(l) = 0.1510$; \circ , $x_{\text{Ga}}(l) = 0.0535$.

As expected, the experimental results in the present study do not show this large Ga increase, since the base operating conditions gave GaAs mole fraction close to the limiting value (see Figure 2-12).

The effect of adding excess HCl to the mixing zone on the growth rate is shown in Figure 2-15. The decrease in growth rate with added HCl was first order. This decrease in growth rate was also observed by other investigators[27,65,66] when a threshold amount of HCl was exceeded. Jurgensen *et al.*[65] demonstrated that the threshold amount of HCl was dependent on source temperature. The authors showed that the decrease in growth rate occurred only after extraneous wall deposition was eliminated by sufficient HCl injection. These observations are consistent with the present work where no wall deposition was observed.

The present study showed that a limiting composition of $\text{Ga}_{0.88}\text{In}_{0.12}\text{As}$ was obtained with the 15.10 at.% Ga source alloy. This result agrees with the limiting value of $\text{Ga}_{0.87}\text{In}_{0.13}\text{As}$ reported by Quinlan and Erstfeld[27] with the use of a 11.8 at.% Ga source alloy. These authors reported the deposition of $\text{Ga}_{0.87}\text{In}_{0.13}\text{As}$ even in the etching regime of the growth curve. Similar studies with 5.35 at.% Ga alloy in the present investigation showed no deposition in the etching regime when the layers were analyzed with sputter Auger electron spectroscopy.

2.4.2 Source Zone Performance

A possible explanation for the dependence of the deposited film composition on the inlet HCl mole fraction is non-equilibrium conversion of HCl in the source zone. Experimental results[21,69-72] reported by previous investigators indicate that the reaction of HCl with liquid group III metals is not complete at all operating conditions for a tubular-shaped source zone. Ban *et al.*[69] reported a 78% conversion of HCl by reaction with indium at 800 °C with the value of P_{HCl}° equal to 3×10^{-2} atm. The conversion efficiency changed little with inlet HCl

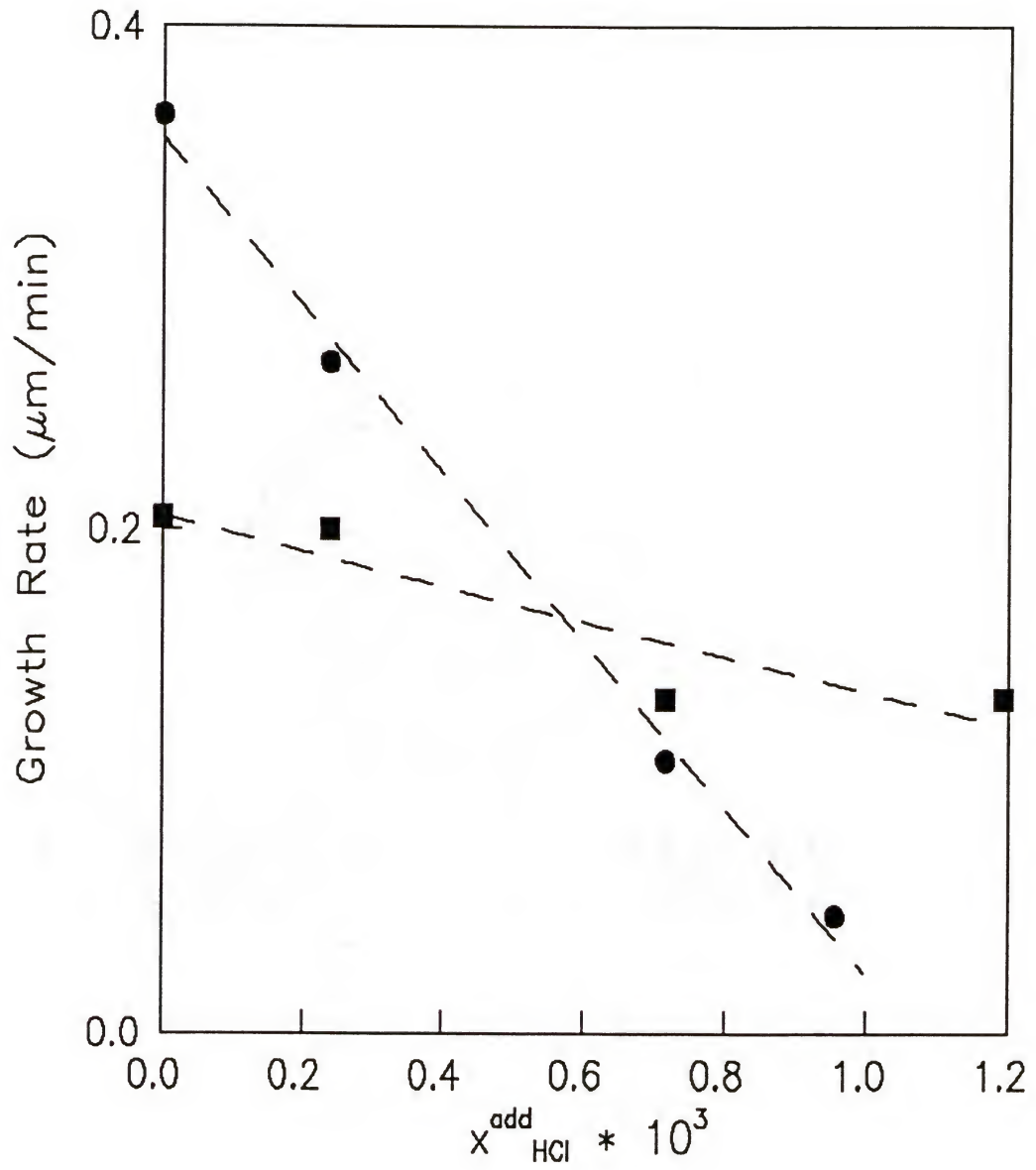


Figure 2-15: The growth rate of $\text{Ga}_x\text{In}_{1-x}\text{As}$ as a function of added HCl mole fraction at $T_d = 700^\circ\text{C}$, $x_{\text{HCl}}^\circ = 0.0072$, and $x_{\text{AsH}_3}^\circ = 0.0033$. Source alloy compositions: \square , $x_{\text{Ga}}(l) = 0.1510$; \circ , $x_{\text{Ga}}(l) = 0.0535$.

partial pressure in the range 3×10^{-3} to 3×10^{-2} atm. These results were recently confirmed by Hsieh[18] who showed that the reaction efficiency of HCl with Ga or In is not affected by the HCl inlet partial pressure. Though the reaction efficiency does not change with the HCl inlet mole fraction, the total amount of unreacted HCl transported to the deposition zone does change. These observations suggest that the dependence of the film composition reported in Figure 2-12 may result from incomplete conversion of HCl in the source zone.

A study was performed to demonstrate that non-equilibrium conversion of HCl occurs in this particular source-boat at typical operating conditions. Hsieh[18] demonstrated that mass transfer is the primary limitation for converting HCl to group III metal chlorides in the source zone. Therefore a change in the gas velocity in the source zone should affect the conversion of HCl if non-equilibrium conditions exist in the source. The gas velocity in the source zone was varied by changing the H_2 flow rate in the source while maintaining the flow rate of HCl at a constant value. A constant velocity in the mixing and deposition zones was maintained by changing the amount of H_2 added through a dopant line in the mixing zone. Film compositions and growth rates were measured as a function of gas velocity in the source zone for two alloy source compositions, 15.10 and 8.69 at.% Ga. As shown in Figure 2-16, the Ga mole fraction in the film increases with increasing volumetric flow rate in the source while the growth rate remains constant. The observed change in the film composition indicates that the gas velocity influenced the deposition process, presumably through a change in the HCl reaction efficiency. An increase in the volumetric flow rate in the source should give less HCl conversion. A decrease in the HCl conversion adds HCl to the deposition zone and produces a corresponding decrease in the group III transport rate. The variation of film compositions and growth rates with added HCl are given in Figure 2-14 and Figure 2-15, respectively, while the influence of changes in the group III transport rate is given in Figure 2-12 and Figure 2-13. Realizing that the base operating conditions corresponds to growth with a volumetric flow rate of 1000 sccm in Figure 2-16, an increase in the Ga mole fraction in the film is consistent with the results

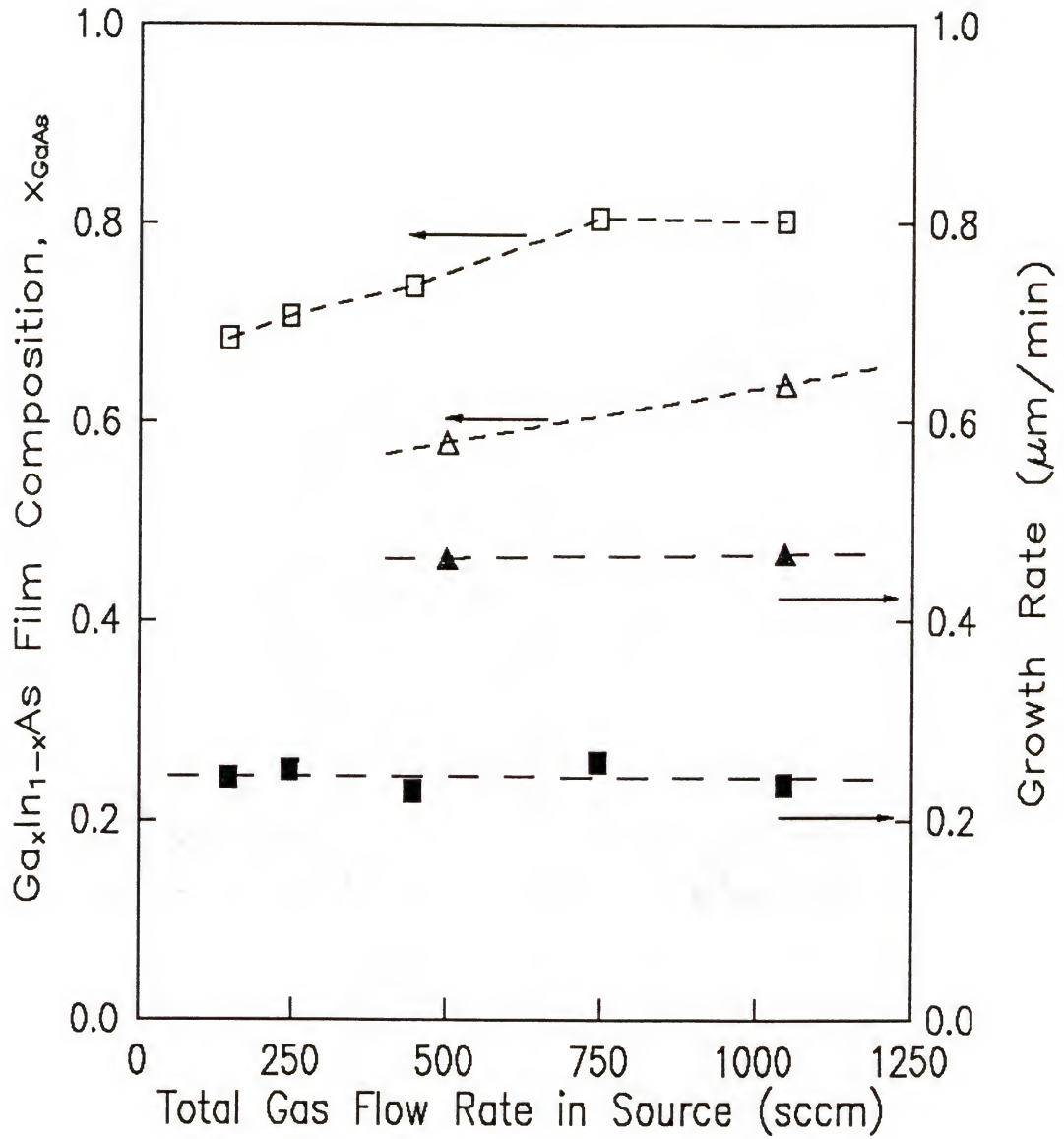


Figure 2-16: The film composition (open symbols) and growth rate (closed symbols) of $Ga_xIn_{1-x}As$ as a function of the total gas flow rate of $H_2 + HCl$ in the source zone at $T_d = 700\text{ }^\circ C$ and $x_{AsH_3}^o = 0.0033$. Source alloy composition and inlet HCl mole fraction: □, $x_{Ga}(l) = 0.1510$, $x_{HCl}^o = 0.0072$; △, $x_{Ga}(l) = 0.0869$, $x_{HCl}^o = 0.0036$.

shown in Figure 2-12 and Figure 2-14. The independence of growth rate with gas velocity is apparently a result of compensation between a decreasing growth rate with increasing group III transport rate (Figure 2-13) and an increasing growth rate with decreasing excess HCl (Figure 2-15).

In an attempt to improve the HCl conversion in the source zone a simple design change of the source boat was made. The modification made in the present study was to add a cover to the source boat to decrease the transverse diffusion length of reactant gases to the liquid surface. The modified structure of the boat is shown in Figure 2-17. The compositions and growth rates of the grown films as a function of linear gas velocity at constant x_{HCl}^0 using the modified source boat are shown in Figure 2-18. The space above the cover was used to add H_2 carrier gas to maintain a constant total flow rate in the deposition zone. Although the results of the film composition indicated less than complete conversion, the increase in growth rates with gas velocity were consistent with an improved HCl conversion. Experiments with the covered boat showed that there was insufficient HCl exiting the source zone to suppress wall deposition, resulting in higher growth rates[73]. Further improvements in HCl conversion could be gained by increasing the reactant residence time (decreasing the gas velocity, increasing the contact length), decreasing the transverse length scale further, and increasing the diffusivity and reaction rate at the liquid surface (decreasing the pressure, increasing the temperature).

A disadvantage of the VPE-hydride process with an alloy source is the decrease in Ga concentration in the alloy over a series of runs[25,26]. This complication may also be resolved with boat design. A study was made of the changes of compositions and growth rates over an extended series of runs using the same alloy. Figure 2-19 shows the results of the study. The abscissa in Figure 2-19 represents the cumulative HCl feed where 32 standard liters (sl) corresponds to approximately 40 one-hour runs. The alloy source (300g) was depleted by 50% after 32 sl. The results shows that the indium concentration in the deposited film increases in a

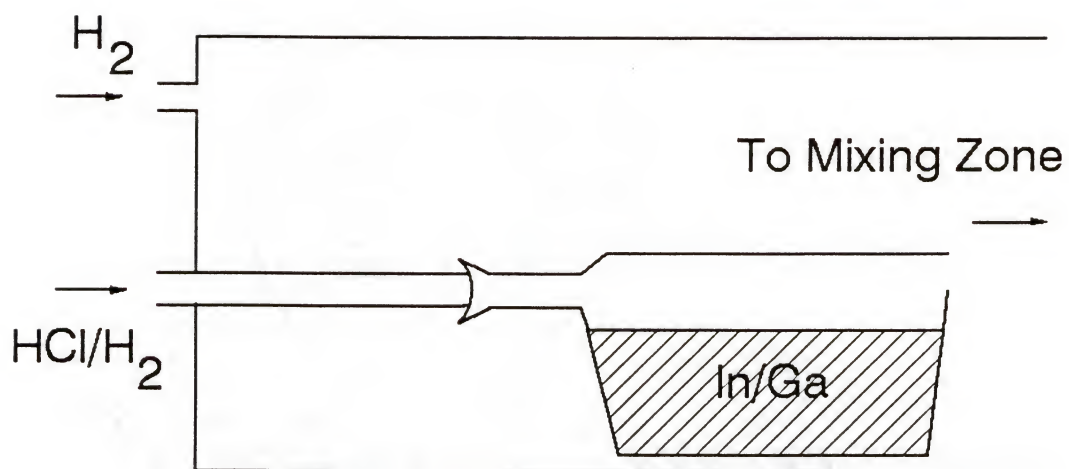


Figure 2-17: Schematic of the modified source alloy boat design.

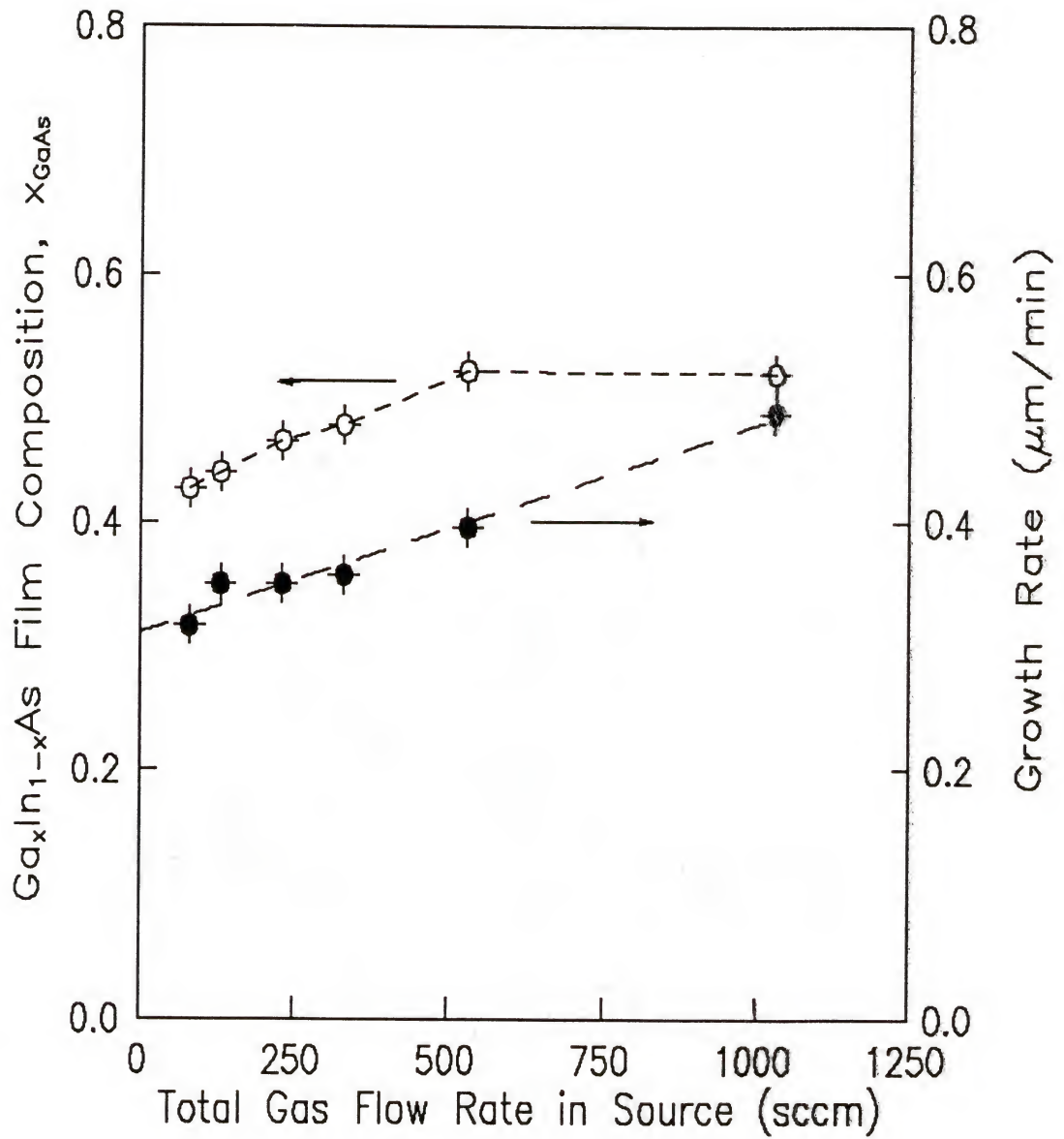


Figure 2-18: The film composition (open symbols) and growth rate (closed symbols) of $\text{Ga}_x\text{In}_{1-x}\text{As}$ as a function of the total gas flow rate of $\text{H}_2 + \text{HCl}$ in the source zone with the modified source alloy boat at $T_d = 700^\circ\text{C}$, $x_{\text{Ga}}^{\circ}(\text{l}) = 0.0661$, $x_{\text{HCl}}^{\circ} = 0.0048$, and $x_{\text{AsH}_3}^{\circ} = 0.0034$.

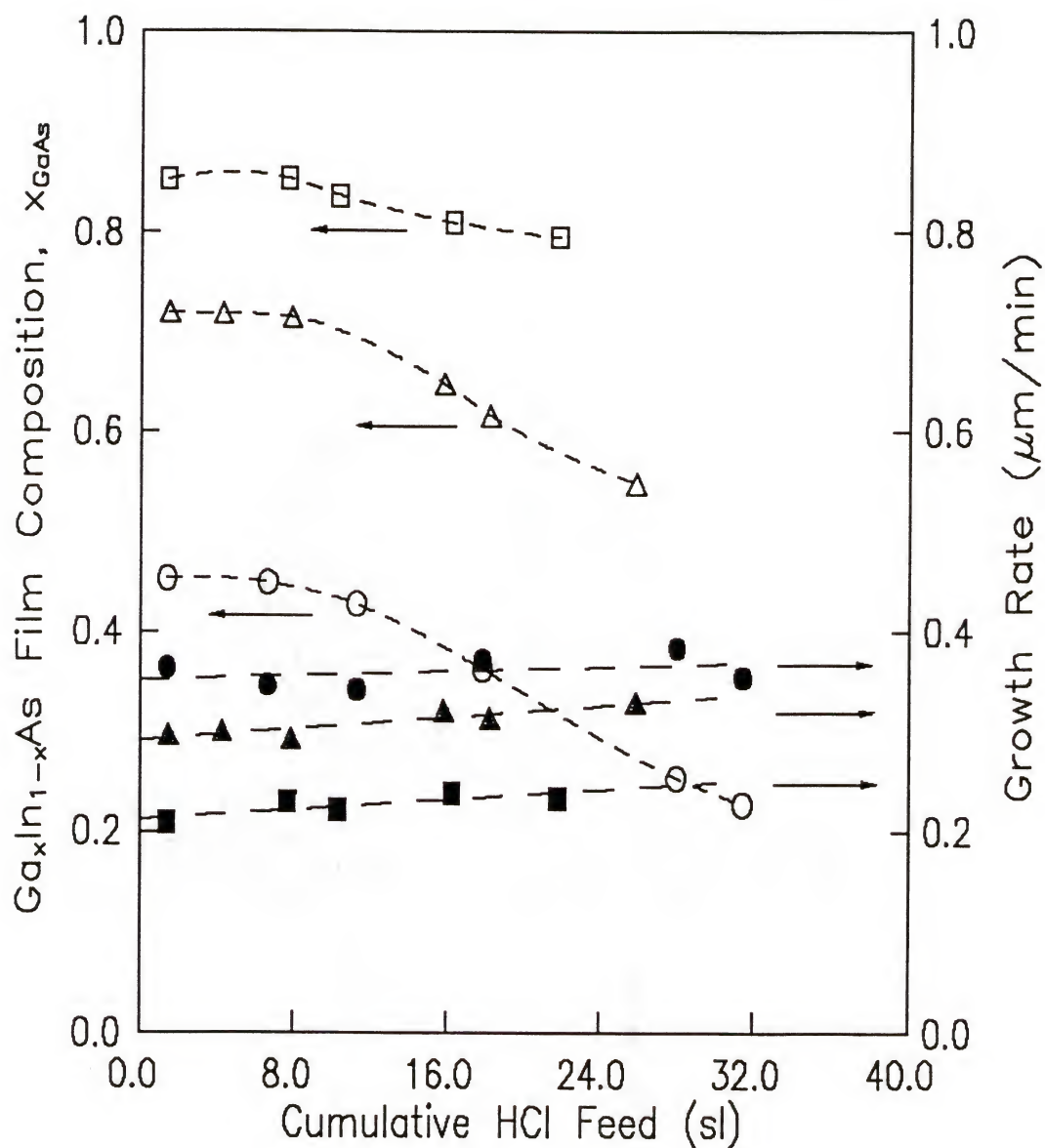


Figure 2-19: The film composition (open symbols) and growth rate (closed symbols) of $Ga_xIn_{1-x}As$ as a function of cumulative HCl feed at $T_d = 700\text{ }^{\circ}C$, $x_{HCl}^o = 0.0072$, and $x_{AsH_3}^o = 0.0033$. Source alloy compositions: \square , $x_{Ga}(l) = 0.1510$; \triangle , $x_{Ga}(l) = 0.0869$; O , $x_{Ga}(l) = 0.0535$.

quantitative fashion similar to the results in Figure 2-8. The increase in growth rate is consistent with the observation that the InAs growth rate is greater than GaAs. Figure 2-19 also shows that a constant composition of the ternary is obtained during approximately the first 10 runs. The decrease of Ga concentration in the alloy corresponding to the In increase in the ternary was confirmed with atomic absorption analyses of the alloy sources. The Ga depletion of the source probably results predominantly from the more efficient transport reaction of Ga than In[18,70]. A positive deviation from ideal solution behavior in the melt also contributes to a Ga-rich vapor at equilibrium if the liquid composition is less than 0.5[50].

2.5 Fabrication of *p-i-n* Photodetectors

Planar *p-i-n* photodetectors were fabricated with 3.5 μm active layers of $\text{Ga}_{0.47}\text{In}_{0.53}\text{As}$ grown from a 6.61 at.% Ga alloy source. The growth conditions of the active layers were identical to this study except the III/V ratio was 10/7. The active layers were grown between a 3.25 μm InP buffer layer and a 1.00 μm InP cap layer on a (100) S-doped InP substrate. After the growth, wafers were inspected for interface quality, layer thickness, and the composition of the $\text{Ga}_x\text{In}_{1-x}\text{As}$ layer. These wafers were fabricated into 75 μm InGaAs detectors that were spaced 600 μm center to center using the planar technology of the standard, ongoing EPITAXX process[74]. The structure of these detectors is schematically shown in Figure 2-20. The following process steps were enacted for the manufacture of the planar InGaAs photodetectors:

(a) A Si_3N_4 diffusion barrier film is deposited in a plasma enhanced chemical vapor deposition unit. Typical films are 700 - 1500 Å thick and have a refractive index of 1.95 - 2.10.

(b) A diffusion window is photolithographically defined using positive photoresist. The Si_3N_4 is removed by a Freon plasma etching, and the resist is stripped by an oxygen plasma.

(c) Zn diffusion is accomplished by heating a sealed ampoule in the range 500 to 550 °C. About 15 mg of Zn_3As_2 is placed into an ampoule as a source of Zn. The position of the

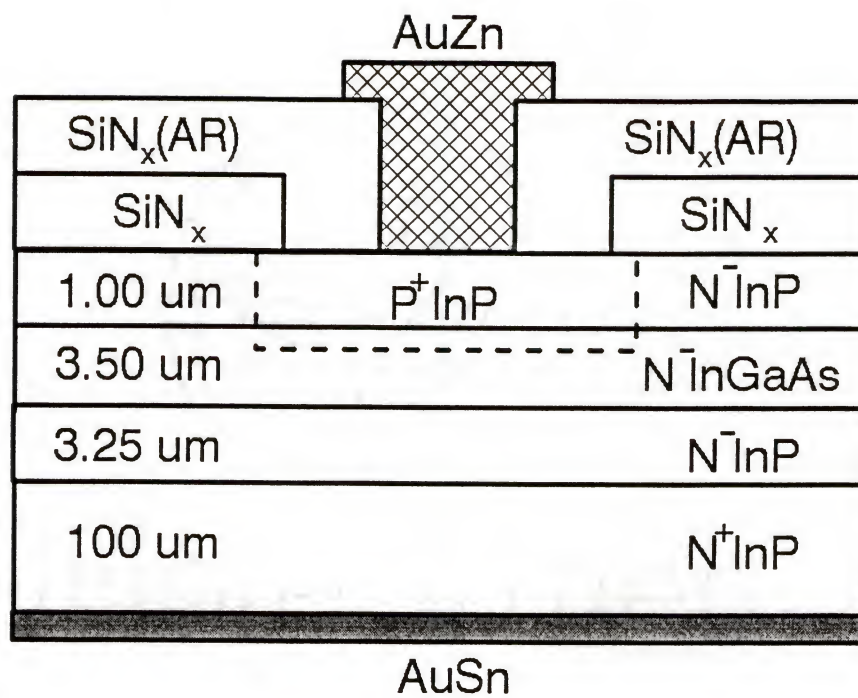


Figure 2-20: Schematic of planar InGaAs/InP *p-i-n* photodetector with active layer grown from Ga/In alloy source.

p-n junction is adjusted to 1000 - 1500 Å below the InP/InGaAs hetero-interface. The diffusion time thus depends on the thickness of an InP cap layer. Diffusion times ranged from 20 to 30 min at 550 °C.

(d) A second Si₃N₄ deposition is performed in the same plasma system. The thickness of this film is adjusted to give optimum anti-reflection properties in the wavelength range of interest.

(e) Following photolithographical definition, contact areas are opened. Si₃N₄ etching and resist stripping are as described in step (b).

(f) A thermally deposited AuZn alloy, subsequently annealed at 420 °C, forms the 45 µm diameter p-side contact.

(g) Wafers are lapped to a 100 µm thickness to facilitate subsequent scribing.

(h) Thermal deposition of a AuSn layer on the back of the wafer provides contact to n-side.

Detector testing was performed on an automated step and repeat prober (Allesi, Inc., Model REL-4500). Its essential parts are a precise x-y stage with a vacuum chuck for wafer holding; a fine diameter probe mounted on an x-y-z positioner connected to the appropriate measurement instruments (*e.g.*, model 617 Keithley electrometer for low current measurements) and a powerful long working distance microscope. The x-y station is computer programmed for controlled steps with precision of ± 1 µm. After testing, the following operations are enacted: (a) scribing and breaking, (b) sorting (*i.e.*, elimination of inked chips), (c) cosmetic inspection of chips, (d) chip mounting with AuSn performed onto ceramic submounts or TO packages, (e) wire bonding, (f) hermetic capping (TO packages), (g) testing (electrical, mechanical, cosmetic), (h) burn in, and (i) final testing and inspection.

The characteristics of the devices fabricated with the present technique compares favorably with InGaAs *p-i-n* photodetectors reported in the literature[75]. The fabricated photodetectors exhibited the following properties: dark current, 10 to 20 nA at -5 V;

capacitance, 0.88 to 0.92 pF; responsivity, 0.84 to 0.86 A/W at 1.3 μm ; and breakdown voltage, > 40 V. The data demonstrates that epitaxial layers of $\text{Ga}_{0.47}\text{In}_{0.53}\text{As}$ grown from Ga/In alloys are suitable for the production of state-of-the-art *p-i-n* photodetectors for fiber optic applications.

2.6 Summary

The VPE-hydride process using a Ga/In alloy source has been studied in detail for the preparation of epitaxial layers of $\text{Ga}_x\text{In}_{1-x}\text{As}$. The compositions and growth rates were measured as a function of the following process parameters: source x_{HCl}° , $x_{\text{AsH}_3}^\circ$, mixing zone x_{HCl}° , gas velocity, deposition temperature, alloy composition, and source geometry. The results revealed that reaction kinetics and mass transfer play important roles, particularly in determining the growth-rate behavior. An equilibrium analysis, nevertheless, could explain the film compositional behavior for most process parameter changes. Table 2-2 gives a qualitative summary of the effects of these parameters on the compositions and growth rates of the epitaxial layers. Lattice-matched $\text{Ga}_{0.47}\text{In}_{0.53}\text{As}$ epitaxial layers could be grown on InP substrates with alloys containing 5 to 8 at.% Ga. The study demonstrated that the VPE-hydride method with an alloy source can be successfully used to fabricate high quality *p-i-n* photodetectors. A problem with the technique is gallium depletion in the source with continued use. This problem is related in part to non-equilibrium conversion in the source zone. Improved reactor design for the source region with mixing zone HCl injection should extend the lifetime of an alloy source.

Table 2-2: Influence of Increasing Process Parameters on the Composition and Growth Rates of $\text{Ga}_x\text{In}_{1-x}\text{As}$ Grown from Ga/In Alloys.

Parameter	x_{HCl}° (added)	x_{HCl}°	gas velocity	$x_{\text{AsH}_3}^{\circ}$	T_d	number of runs
Film Composition (x_{GaAs})	↑	↑	↑	↓	↓	↓
Growth Rate	↓	↑ ↓	↔	↑	↑	↑

Legend: ↑ : increase in x_{GaAs} or growth rate
 ↓ : decrease in x_{GaAs} or growth rate
 ↔ : negligible change

CHAPTER III

BACKGROUND IMPURITIES IN INDIUM PHOSPHIDE EPITAXIAL FILMS GROWN BY HYDRIDE VPE

3.1 Introduction

Epitaxial layers of InP have become increasingly important, due primarily to their suitability in optoelectronic and microwave device applications. For devices such as transferred electron devices, MIS transistors, FETs, *p-i-n* photodiodes, and avalanche photodiodes, a high purity epitaxial layer of InP is a fundamental requirement. The hydride VPE process has been an important growth technique with certain advantages for large-scale production, including high growth rate and process controllability. A limitation of hydride VPE, however, is imposed by the relatively high level of background doping (typically on the order of $5 \times 10^{15} \text{ cm}^{-3}$, n-type), although lower values in the range $3 \times 10^{14} - 6 \times 10^{14} \text{ cm}^{-3}$ have been reported[76]. This compares with the other growth techniques such as the LPE and the chloride VPE in which the background electron concentrations of less than 10^{15} cm^{-3} are routinely obtained[77-78]. Control of the background doping in the deposited film is a prerequisite for production of quality devices.

The background impurities which are incorporated into the epitaxial layers during growth have different origins. Impurities contained in the source materials used in the hydride VPE process such as the source gases (HCl, PH₃, H₂), the source metal (In), and the substrate (InP) can be the sources of background impurities. The chemicals used in the substrate preparation can be another source of background impurities. It is generally believed that the HCl source is the main source of impurities when used from a high pressure gas cylinder. Zinkiewicz *et al.*[79] have studied the growth of InP and the ternary Ga_xIn_{1-x}As by hydride

VPE and reported that Zn, Cu, and Hg were present as unintentional donors. The work of Skromme *et al.*[80] identified some of the unintentional donors and acceptors in GaAs and InP prepared by the hydride VPE. They found C, Zn, Cu, and Mn as acceptors and Si, S, and Ge as donors in GaAs. Epitaxial films of InP were found to contain Zn, C or Mg, and unidentifiable acceptor along with Si and S as donors. Usui and Watanabe[81] analyzed the used indium by mass spectroscopy and detected a few ppm impurity contamination of Sn, Fe, and Cu which were hardly detected in the raw indium before the growth experiment. Their results showed that the In source has a gettering effect for impurities in the input gases, mainly cylinder HCl. This effect was enhanced by increasing the In source temperature. They also found that a controlled injection of O₂ into the deposition zone could reduce the background impurities in the InP film. This phenomenon has been recently confirmed by Iwata and Inossita[82], although a study of O₂ injection into the In source zone did not show any evidence of influencing the background doping[76]. The gettering of impurities by the In source has been also observed by Olsen[83] at elevated source zone temperature (800 to 900 °C or higher). McCollum *et al.*[76], however, observed that the level of background doping increases when the source zone temperature increases.

The use of a hot wall reactor (> 800 °C) is another potential source of the background impurities in hydride and chloride VPE processes. The interaction between the hot SiO₂ wall and the reactant gases may introduce Si as a background impurity. Cairns and Fairman [84,85] and DiLorenzo *et al.*[86] found that in the growth of GaAs by the chloride VPE technique, the unintentional impurity incorporation in the epitaxial layer decreased with the increase of AsCl₃ mole fraction in the inlet gas stream. DiLorenzo and Moore[87] identified the primary unintentional dopant as Si by the use of photoluminescence spectroscopy. Further, they proposed a thermodynamic model for the generation of vapor phase chlorosilanes as a result of the interaction of HCl with the quartz (SiO₂) reactor wall and presented an expression for the activity of solid silicon (*i.e.*, as an impurity) as a function of the partial pressures of the

chlorosilanes. This model showed that increasing the vapor HCl concentration (*i.e.*, as a result of AsCl_3 decomposition) decreased the condensed phase silicon activity by further stabilizing the silicon species in the vapor phase in the form of chlorosilanes. Additionally, their model predicted that the generation of vapor phase silicon species could be suppressed by the injection of H_2O vapor into the system. Many experimental and thermodynamic studies[88-99] confirmed this model, especially in the growth of GaAs[88-93] and InP[94-96] by chloride VPE and in the growth of GaAs[97-99] by hydride VPE.

Jones[100] performed a thermodynamic analysis of the InP hydride system in order to understand the effect of process parameters on the unintentional Si incorporation. The calculations predicted that decreasing temperatures lowered the Si activity in the epitaxial layer. Additionally, the Si activity was decreased by increasing the PH_3 and/or HCl inlet composition. Very little effect was noted when HCl was added downstream of the source zone. Meyer[37] also performed a comprehensive thermodynamic analysis of the InP hydride and chloride systems by using a stoichiometric algorithm (see chapter II). His results showed that the formation of vapor phase silicon species were greatly increased with an increase in the temperature in the source and mixing zones. The formation of silicon species could be suppressed by the addition of small amount of H_2O or by replacing the H_2 carrier gas with an inert. His results also showed that the unintentional incorporation of Si may be decreased by reducing the amount of silicon species in the vapor phase by shifting these silicon species from hydrogen rich to chlorine rich species through the addition of HCl. In general, the equilibrium behavior of Si incorporation in hydride VPE grown InP is explained by the simple model of Dilorenzo and Moore[87]. Some of the experimental studies of hydride VPE, however, are somewhat intriguing. Buckley[101] has studied hydride VPE of $\text{Ga}_x\text{In}_{1-x}\text{As}$ and found that the AsH_3 , not the HCl, is the main factor determining the level of unintentional doping of the grown layers under conditions of constant growth rate. An inverse proportionality between carrier concentration and growth rate was observed, and a model was developed to account for

this relationship which further supported his conclusion of AsH_3 being the main source of the unintentional dopant. However, the impurity species in the film were not identified. Anderson[102] has studied the growth of InP by hydride VPE in order to determine the effect of the HCl mole fraction, H_2 flow rate, and mixing zone temperature on unintentional impurity incorporation. These parameters were found to produce only minor changes in the electrical behavior of the InP epitaxial layers.

The unintentional doping of the epitaxial InP grown by the hydride VPE technique is revisited in the present study. The effects of inlet mole fraction of HCl (x_{HCl}°), inlet mole fraction of PH_3 ($x_{\text{PH}_3}^\circ$), and source zone temperature (T_s) on the extent of impurity incorporation were investigated in order to understand the chemistry involved in the background doping process. The variable temperature Hall effect was used to measure the net carrier concentration and mobility of InP films, and the results are interpreted with respect to the process variables. In addition, an attempt has been made to identify the major background impurities in the InP films. Low temperature Fourier transform photoluminescence (FTPL) spectroscopy was used for this purpose and the results are reported.

3.2 Experiment

The hydride VPE reactor used in this study was identical to the double-barrel reactor used for the alloy source experiment (Figure 2-1). The indium boat was inserted into one of the source barrels. The base operating conditions were as follows: source zone temperature, 838 °C; mixing zone temperature, 820 °C; deposition temperature, 700 °C; and total pressure, 1 atm. The III/V ratio was fixed at one (20 sccm of HCl and 200 sccm of 10% PH_3 in H_2) and the total volumetric flow rate was held constant at 4200 sccm (25 cm/s linear velocity). Deposition time was fixed at 10 min. The inlet mole fractions of HCl and PH_3 and source zone temperature were varied about these base operating conditions.

Phosphine was supplied as a 10% mixture in hydrogen (Airco, VLSI grade). The carrier hydrogen was purified by Pd-alloy diffusion. HCl (Airco, ULSI grade) was 99.999% pure, and indium (RASA industries) was 99.99999% pure. Substates grown by the LEC method were Fe-doped InP (Crystacomm), cut 2° off the (100) toward the nearest (110).

The substrates were etched and cleaned by the following procedure: (a) rinse with DI-water; (b) Caro's acid (5:1:1 H₂SO₄:H₂O₂:H₂O) etching for 3 min with stirring; (c) DI-water and methanol rinse; (d) 1% Br₂ in CH₃OH solution etching for 2 min with stirring; (e) methanol rinse; (f) N₂ spray dry. The etched substrate, typically about 1×1 cm², was placed into the reactor load-lock chamber and flushed with H₂ prior to opening the reactor. Reactant flows were initiated about 15 min prior to the insertion of substrates, and the substrate was preheated in a PH₃/H₂ mixture ($P_{\text{PH}_3}^\circ = 3.9 \times 10^{-2}$ atm) prior to deposition.

The layer thickness was measured by optical microscopy on cleaved and stained samples. Samples were stained by the solution of KOH(6 g):K₃Fe(CN)₆(4 g) in DI-water(50 cc). The background carrier concentration and mobility were measured by a variable temperature Hall effect system. The system was a custom design and its essential parts included a cryostage (CTI-Cryogenics) equipped with a resistive heater with temperature controller (Palm Beach Cryophysics) for temperature varying measurements, a magnet with constant current supply (Walker Scientific), and an electrometer (Keithley). Details of the system configuration, sample preparation procedure, and measurement procedure are described elsewhere[103]. Measurements were performed with magnetic flux density (B) of 4600 gauss.

The identification of background impurities was performed by a Fourier transform photoluminescence (FTPL) spectroscopy[104,105]. In FTPL spectroscopy, the photoexcited emission is analysed interferometrically rather than with a dispersive grating monochromator. The classical advantages of interferometry relative to monochromation were expressed by Jacquinot as the throughput advantage and by Fellgett as the multiplex advantage[106]. The most important manifestation of the throughput advantage to PL spectroscopy is that high

resolution measurements can be made while maintaining a large circular aperture. With a conventional grating monochromator, the power transmitted depends directly on the square of the slit area (in the case of equal slits). However, the resolution of a grating monochromator is inversely proportional to the slit width, hence, increasing resolution results in a concomitant decrease in transmitted power. For a given resolution then, the power transmitted is greater for an interferometer than for a grating monochromator. The second advantage of an interferometer, that of multiplexing, allows the entire spectrum within the bandwidth of the interferometer to be obtained in a single rapid scan of the interferometer. Another aspect of the multiplex advantage is that broad spectral bandwidths are obtainable with beamsplitters relative to diffraction gratings. Finally an advantage not explicit in the above is the high wavelength calibration precision that is obtainable with an interferometer as wavelength sampling is referenced to a HeNe laser. The luminescence was excited in the present system using an argon ion laser of wavelength at 514.5 nm. The laser at the sample was unfocused with a spot diameter of approximately 2 mm and a power density of typically 0.18 W/cm². Samples were placed in a bottom looking liquid helium immersion dewar and analysed in a backscattering configuration using f/1.2 collection optics. The measurement temperature was at 4.2 K. The interferometer employed for spectral analysis was the Twyman-Green version of the Michelson, that is, light from the source is collimated before being amplitude divided by the beamsplitter. A CaF₂ beamsplitter was used for studies in the 0.7 to 5.5 μm region, and a liquid nitrogen cooled Ge photovoltaic detector was employed for the 0.7 to 1.65 μm region. Interferograms were Fourier transformed using a cosine apodization function. Spectra were signal averaged 30 times. Energy calibration was made referenced to the HeNe vacuum wavenumber of 15798 cm⁻¹. A spectral resolution of 2 cm⁻¹ (0.25 meV) was used.

3.3 Results and Discussion

Epitaxial layers of InP, 6 to 13 μm in thickness, were grown using various inlet mole fractions of HCl (x_{HCl}°) and PH_3 ($x_{\text{PH}_3}^{\circ}$) and source zone temperature (T_s). Operating conditions of all the growth runs and the results are summarized in Table 3-1. In general, the growth rate was found to increase with increasing x_{HCl}° , indicating that the operating conditions used in this study are in the region where the HCl conversion in the source zone is far from completion. Previous studies with the identical hydride VPE reactor showed that there is a maximum in growth rate typically around the III/V ratio of one (see chapter II). The growth rate was, however, relatively independent of the inlet mole fraction of PH_3 ($x_{\text{PH}_3}^{\circ}$) and the source zone temperature (T_s). Samples were first analyzed by FTPL spectroscopy at room temperature (293 K). The measured values of the full width at half maximum (FWHM) of the room temperature PL peaks at 1.34 eV are also listed in Table 3-1. No distinct variation of this value was noticed with the change in the process variables, except for the sample #2729 (growth with the highest source zone temperature) which showed a relatively high value of the FWHM compared to the rest of the samples. Samples grown with extreme values of each process variable were selected for further characterization.

3.3.1 Hall measurements

The Hall data were obtained in the temperature range 35 to 300 K. Each InP sample was n-type. Figure 3-1 shows the net carrier concentration ($n = 1/eR_H$, where e is the electron charge and R_H is the Hall coefficient) plotted on a log scale versus inverse temperature $1/T$. Figure 3-2 shows a log-log plot of the electron mobility (μ) versus measurement temperature, T . Samples grown with different source zone temperatures were compared. Source zone temperature was varied at 770 °C, 838 °C, and 887 °C, while the inlet mole fractions of HCl and PH_3 were kept constant at 4.739×10^{-3} . Two samples were grown with source zone temperature of 838 °C, thus the data are represented with error bars. As clearly shown in

Table 3-1: Growth Conditions of the InP Characterization Samples and FWHM Values of the Room temperature (293 K) PL Peaks.
($P_t = 1$ atm; $T_d = 700$ °C; Deposition time = 10 min)

Sample No.	Source Temp.(°C)	x_{HCl}° ($\times 10^3$)	$x_{\text{PH}_3}^\circ$ ($\times 10^3$)	III/V ratio	Layer Thick.(μm)	FWHM (meV)
#2723	770	4.739	4.739	1/1	7.4	29.6
#2724	803	4.739	4.739	1/1	6.8	30.5
#2725 #2715	838	4.739	4.739	1/1	6.8 6.8	30.1 28.6
#2729	887	4.739	4.739	1/1	6.3	34.5
#2721	838	2.593	8.858	1/3	5.4	29.1
#2720	838	4.525	9.050	1/2	6.3	31.7
#2719	838	4.630	6.944	2/3	7.8	28.8
#2716	838	7.092	4.728	3/2	8.5	30.2
#2717	838	9.434	4.717	2/1	9.3	30.5
#2718	838	14.085	4.695	3/1	12.9	32.2

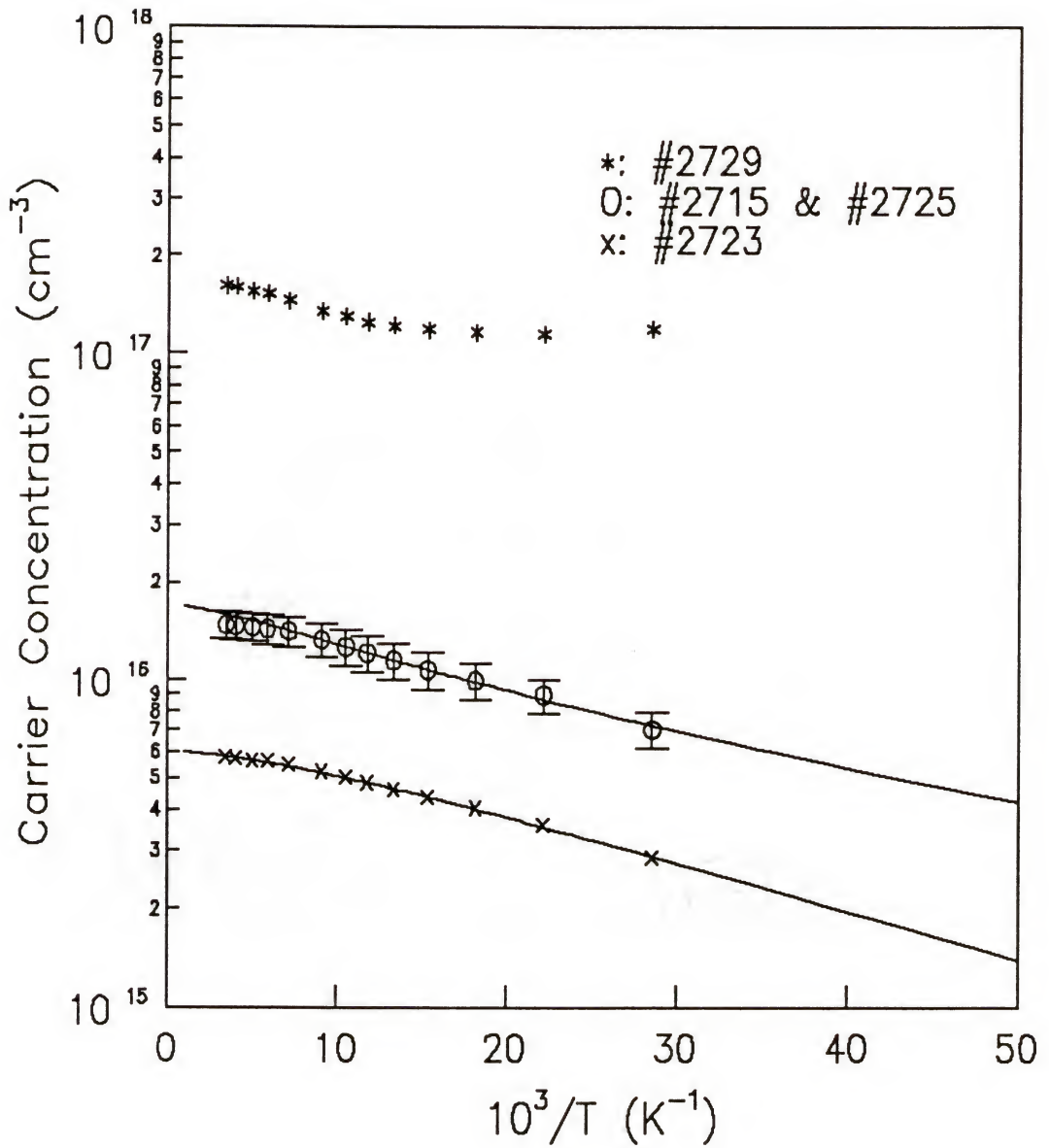


Figure 3-1: Temperature dependent Hall data of VPE InP layers: carrier concentration is plotted against $1/T$. Solid curves represent the theoretical data fit described in the text. Process conditions: $*$, $T_s = 887^\circ\text{C}$; O , $T_s = 838^\circ\text{C}$; x , $T_s = 770^\circ\text{C}$ at $x_{\text{PH}_3} = 4.739 \times 10^{-3}$ and $x_{\text{HCl}} = 4.739 \times 10^{-3}$.

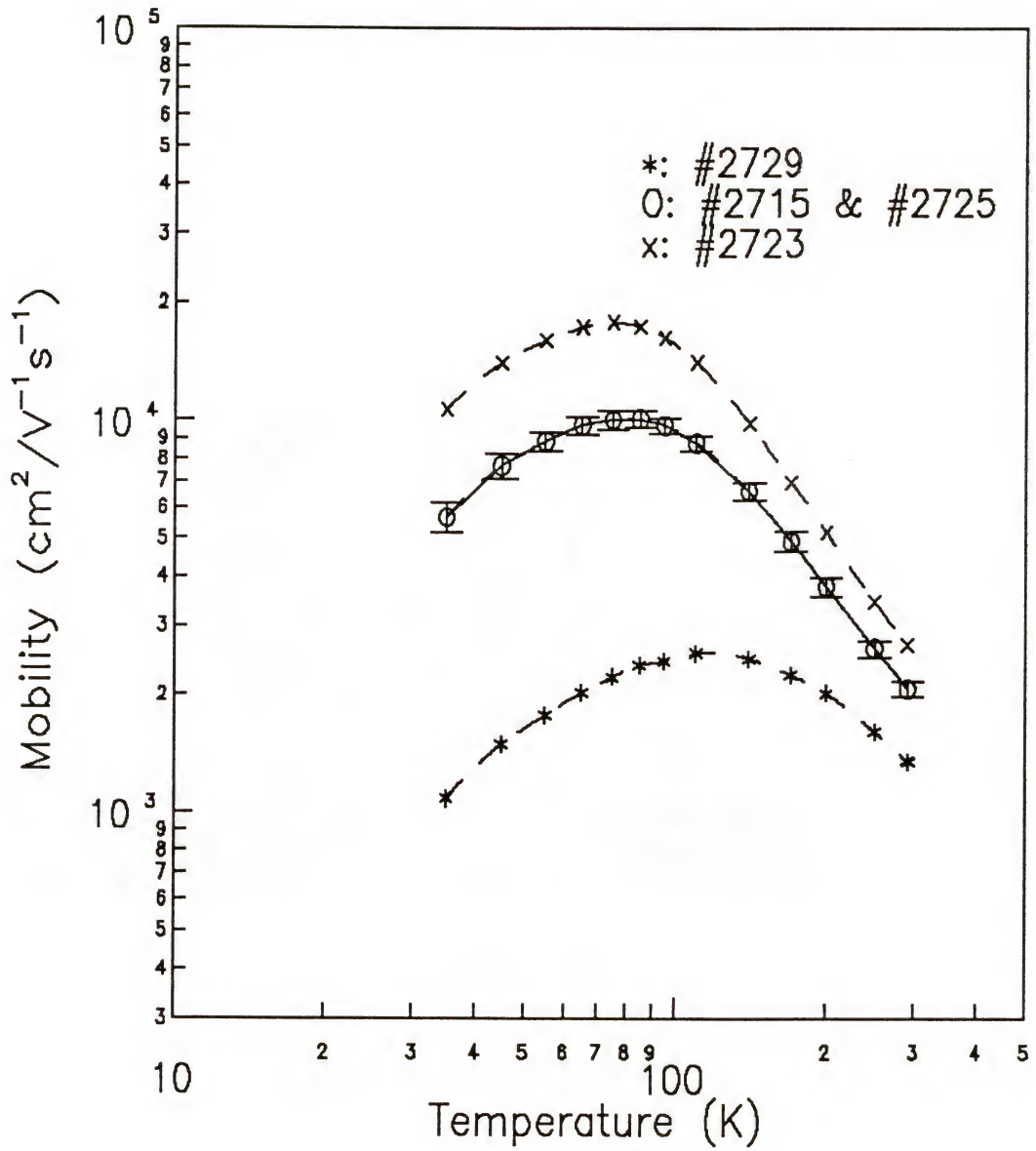


Figure 3-2: Temperature dependent Hall data of VPE InP layers: mobility is plotted against T . Dashed curves merely connect the experimental data points. Process conditions: *, $T_s = 887^\circ\text{C}$; O, $T_s = 838^\circ\text{C}$; x, $T_s = 770^\circ\text{C}$ at $x_{\text{PH}_3}^\circ = 4.739 \times 10^{-3}$ and $x_{\text{HCl}}^\circ = 4.739 \times 10^{-3}$.

Figure 3-1 and Figure 3-2, the background concentration of the InP film increases and the mobility decreases dramatically, as the source zone temperature increases. These results are consistent with an experimental observation by McCollum *et al.*[76]. A thermodynamic analysis[37] also predicts an increase in the background doping with increasing source zone temperature, since the formation of vapor phase silicon species increases with the increasing source zone temperature. Impurity gettering by the In source[81,83] was not observed in the present study.

The effect of varying the inlet mole fractions of HCl and PH₃ on the extent of impurity incorporation is shown in Figure 3-3 (carrier concentration) and Figure 3-4 (mobility). The background carrier concentration decreases and correspondingly the mobility increases with the increase of inlet mole fraction of HCl. This result is in agreement with many experimental and thermodynamic studies[88-99] for the growth of GaAs and InP by the chloride technique and for the growth of GaAs by the hydride technique, in the sense of Dilorenzo and Moore's model[87] in which the increased HCl lowers the background Si doping of the film by stabilizing the silicon species in the vapor phase in the form of chlorosilanes. This result is also a clear experimental evidence of the hydride VPE grown InP following the thermodynamic predictions[37,100]. The dramatic decrease in the background doping with lowered source zone temperatures (Figure 3-1) can also be explained in the same context that the reduced HCl conversion at lower source zone temperatures provides more HCl in the vapor phase. The background doping in the InP film seems not to be affected by the change in the inlet mole fraction of PH₃, although a thermodynamic study[100] predicts the decrease in Si incorporation with increasing $x_{\text{PH}_3}^0$. A slight decrease of background carrier concentration was observed with increasing $x_{\text{PH}_3}^0$ (Figure 3-3), but the magnitude of the change was within the error bar. The increase in the inlet mole fraction of PH₃ might have decreased the background doping, since the inlet mole fraction of HCl was also decreased in that case and the decrease in x_{HCl}^0 should have increased the background doping, but it is not clear.

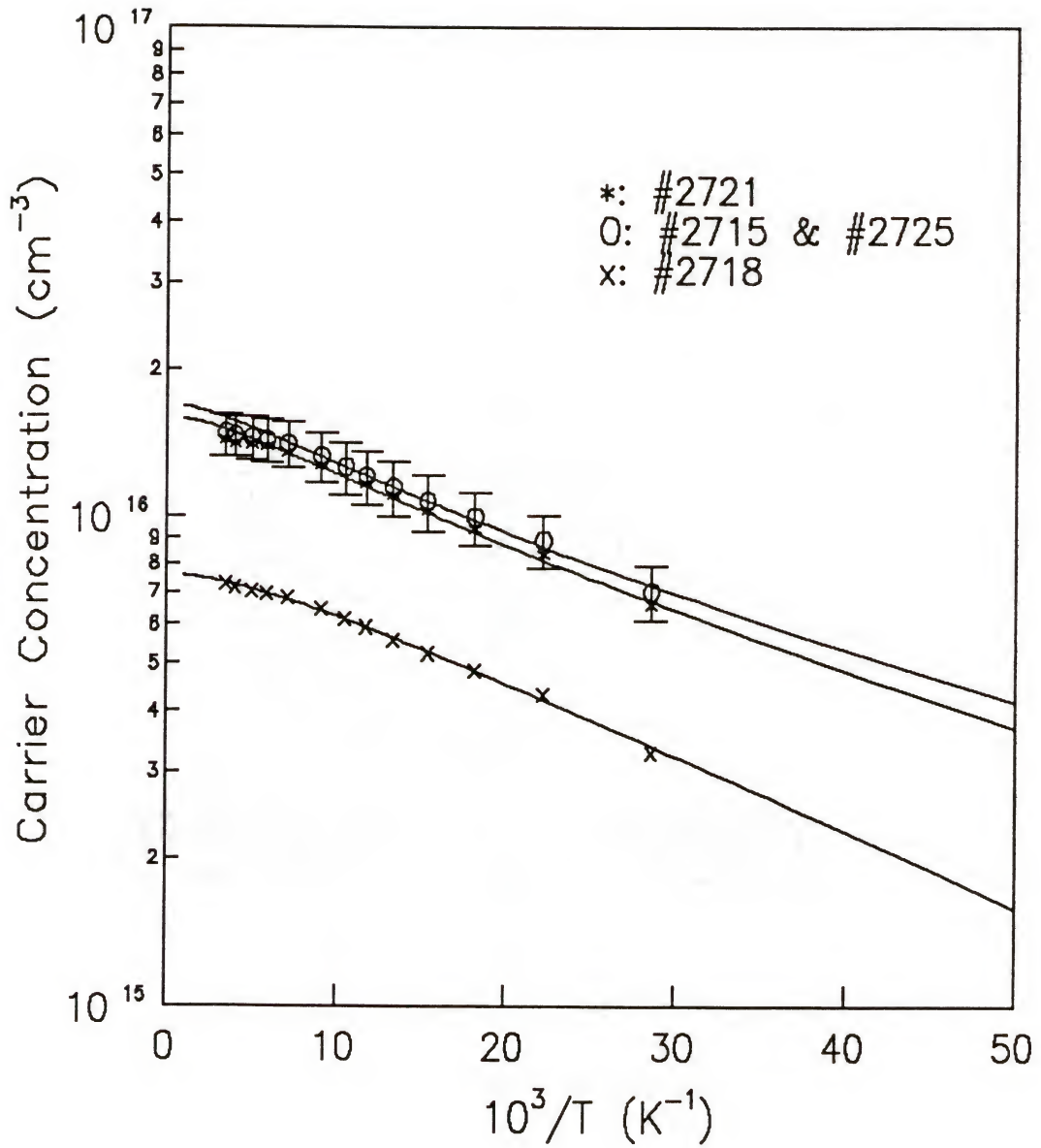


Figure 3-3: Temperature dependent Hall data of VPE InP layers: carrier concentration is plotted against $1/T$. Solid curves represent the theoretical data fit described in the text. Process conditions: O, $x_{\text{PH}_3}^0 = 4.739 \times 10^{-3}$ and $x_{\text{HCl}}^0 = 4.739 \times 10^{-3}$; *, $x_{\text{PH}_3}^0 = 8.858 \times 10^{-3}$ and $x_{\text{HCl}}^0 = 2.953 \times 10^{-3}$; x, $x_{\text{PH}_3}^0 = 4.695 \times 10^{-3}$ and $x_{\text{HCl}}^0 = 14.085 \times 10^{-3}$ at $T_s = 838^\circ\text{C}$.

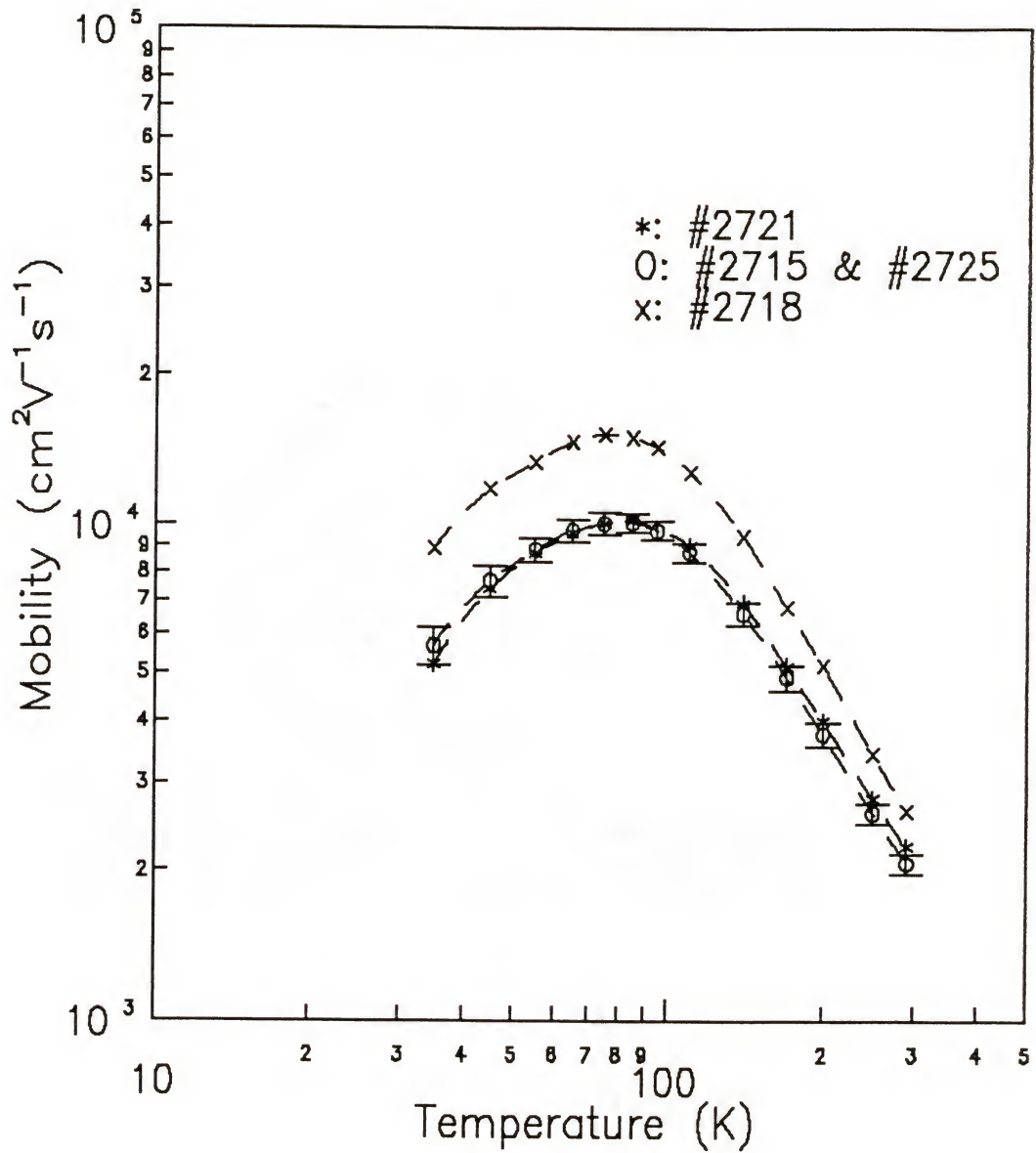


Figure 3-4: Temperature dependent Hall data of VPE InP layers: mobility is plotted against T. Dashed curves merely connect the experimental data points. Process conditions: O, $x_{\text{PH}_3}^\circ = 4.739 \times 10^{-3}$ and $x_{\text{HCl}}^\circ = 4.739 \times 10^{-3}$; *, $x_{\text{PH}_3}^\circ = 8.858 \times 10^{-3}$ and $x_{\text{HCl}}^\circ = 2.953 \times 10^{-3}$; x, $x_{\text{PH}_3}^\circ = 4.695 \times 10^{-3}$ and $x_{\text{HCl}}^\circ = 14.085 \times 10^{-3}$ at $T_s = 838^\circ\text{C}$.

A simple analysis was performed to extract the electrical parameters of the hydride VPE grown InP samples such as the electron concentration in the exhaustion region ($N_d - N_a$), the compensation ratio ($K = N_a/N_d$), and the ionization energy of donor level (E_d). N_d is the donor level density and N_a is the acceptor level density. An analytical formula[107] was used to fit the temperature dependence of electron concentration (n) (Figure 3-1 and Figure 3-3).

$$n(T) = 2(N_d - N_a) \left[\left[1 + \frac{N_a}{gN_c} \exp\left(\frac{E_d}{k_B T}\right) \right] + \left\{ \left[1 + \frac{N_a}{gN_c} \exp\left(\frac{E_d}{k_B T}\right) \right]^2 + \frac{4}{gN_c} (N_d - N_a) \exp\left(\frac{E_d}{k_B T}\right) \right\}^{0.5} \right]^{-1} \quad (3-1)$$

where g is the spin degeneracy factor which is equal to unity in the bands and 0.5 for donor levels, reflecting the fact that an unoccupied donor can receive only one electron, but of either spin (g can take other values for acceptor levels and has a distinct value for each charge state of a multivalent impurity, but it is not of a concern in this treatment of n-type III-V semiconductors); k_B is the Boltzmann constant. The effective density of states for conduction bands (N_c) is given by,

$$N_c = 2 (2\pi m_e k_B T / h^2)^{3/2} \quad (3-2)$$

where m_e is the electron band edge effective mass ($m_e = 0.08m_0$ is used in the calculation following the reference [107], where m_0 is the free electron mass.); h is the Planck's constant. When E_g (bandgap energy) $\gg k_B T > E_d$ (at high temperatures), n is constant and approximately given by $(N_d - N_a)$. This is known as the exhaustion region. As T falls, n reduces and finally varies as $\exp(-E/k_B T)$, where $E = E_d$ when $K = 0$ and $E = E_d/2$ otherwise. The temperature at which the transition between exhaustion and exponential behavior occurs increases with increasing compensation and so the relationship is a useful guide to the material's quality.

There are three unknowns in equation (3-1) which should be evaluated (*i.e.*, $(N_d - N_a)$, K , and E_d). From the experimental data, one can easily estimate the parameters E_d and $(N_d - N_a)$. E_d can be estimated from low-temperature slope and $(N_d - N_a)$ from electron concentration (n) in the exhaustion region extrapolating to high temperatures as $1/T \rightarrow 0$. Then the fitting procedure is rather simple because the estimates for E_d and $(N_d - N_a)$ are used in the first step. The fit is best done by eye using trial and error method, systematically changing the values of the parameters until satisfactory agreement is achieved. The parameters obtained by this procedure are given in Table 3-2.

This simple analysis ignores the temperature dependence of the Hall coefficient and E_d itself. E_d is not a fixed quantity but continuously decreases as the impurity density increases. In high carrier density samples ($> 3 \times 10^{16} \text{ cm}^{-3}$), the donor levels form a band and become degenerated with the conduction band; in this case n ($= 1/eR_H$) is only a weak function of T , and n behaves similar as in metals and it is of little value to continue the procedure in this direction. The deviation of the theoretical curve from the experimental data can also be caused by the temperature dependence of the Hall coefficient (R_H), which is governed by particular scattering mechanism. The combined effect of all these factors limits the range, to which this analysis procedure can be applied, to $(N_d - N_a) < 3 \times 10^{16} \text{ cm}^{-3}$. This condition is fulfilled for all the InP samples with the exception of the sample #2729. This is the reason why the parameters of this sample are not presented in Table 3-2 (Figure 3-1 does not show the theoretical data fit for the sample #2729). For all the other samples, very good fits were obtained over broad temperature range. The donor ionization energies of the InP samples were generally low compared to the values of higher purity InP films grown by the chloride VPE[107]. This is due to the fact that E_d depends on the concentration of impurities. It was shown that[107]

$$E_d = 7.4 [1 - 3.9R_o(N_d - N_a)^{1/3}] \quad (3-3)$$

Table 3-2: Electrical Characteristics of InP Samples
Grown by the Hydride VPE Technique.

Sample No.	n at 77 K (cm ⁻³)	μ at 77 K (cm ² V ⁻¹ s ⁻¹)	$N_d - N_a$ (cm ⁻³)	E_d (meV)	K
#2723	4.584×10^{15}	17788.8	6.0×10^{15}	2.4	0.31
#2715 #2725	1.146×10^{16}	10020.2	1.7×10^{16}	1.5	0.11
#2729	1.211×10^{17}	2214.6	1.8×10^{17}	N/A	N/A
#2721	1.101×10^{16}	10068.8	1.6×10^{16}	2.0	0.08
#2718	5.574×10^{15}	15228.1	7.6×10^{15}	2.6	0.25

Note: average values are listed for samples #2715 and #2725.

with

$$R_o = (m_o/m_e)\epsilon a_o \quad (3-4)$$

where a_o is the Bohr radius and ϵ ($= 12.2$) is the low frequency dielectric constant of InP. This intercepts the vertical axis at the donor ionization energy obtained optically[108] and the linear extrapolation goes to zero at $N_d - N_a = 3.4 \times 10^{16} \text{ cm}^{-3}$. As a self-consistency check on the validity of the analysis, the values of E_d obtained from the fitting to the Hall data on InP are plotted versus $(N_d - N_a)^{1/3}$ in Figure 3-5 and compared with the theoretical line given by the equation (3-3). It shows a reasonably good agreement, indicating the procedure of extracting the electrical parameters is self-consistent. The small ionization energies of donor level can be explained by the relatively high background concentrations in the samples of this study.

3.3.2 FTPL measurements

A lot of work has been done in the theory and experiment of electron-hole radiative recombination, with principal emphasis on processes which dominate the emission spectra in direct bandgap III-V compound semiconductors, and excellent reviews can be found in the literature[109-111]. The theory is fairly well developed, and the results are sufficiently simple to be directly used in analyzing empirical data, for simple processes such as (a) band to band, (b) free exciton, and (c) band to impurity recombination. For the more complex processes, *e.g.*, bound exciton recombination, only principles and general features are available.

Figure 3-6 schematically shows the relative emission energy for a number of zero-phonon recombination processes possible in direct bandgap III-V compounds. The energies indicated are appropriate to GaAs containing one species of donor and one species of acceptor impurity. Similar scheme can be drawn for any direct bandgap III-V material. It is possible to observe all of these emission lines simultaneously in one sample at relatively low temperatures. The relative strengths of the lines in the spectrum depend on temperature, impurity

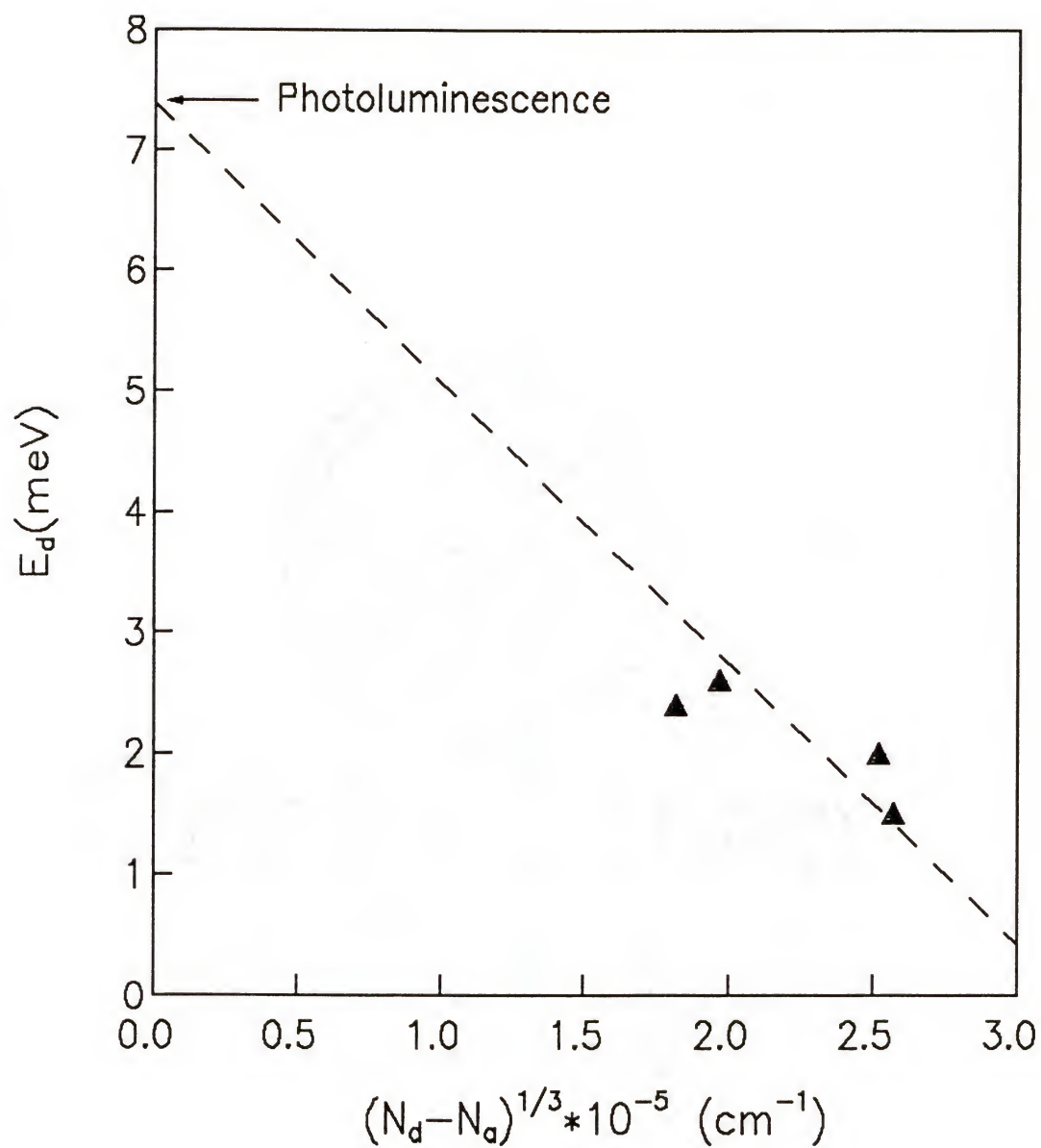


Figure 3-5: Effective donor ionization energy deduced from fits to InP Hall data plotted versus $(N_d - N_a)^{1/3}$. The slope of the line is $3.9R_0$. In the limit of no ionized impurities, E_d approaches the value obtained optically.

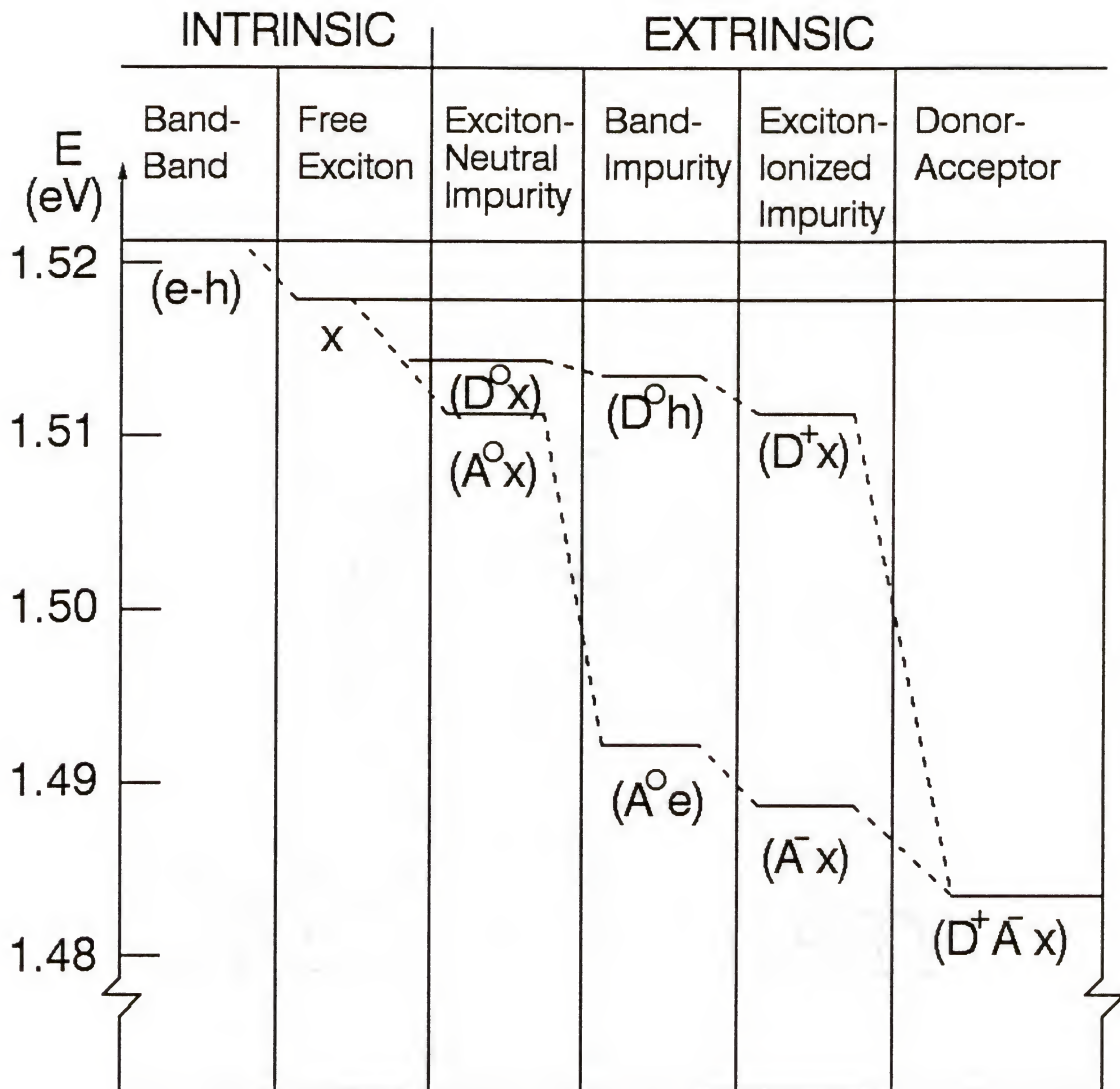


Figure 3-6: Possible no-phonon emission (and absorption) lines for III-V direct bandgap semiconductors neglecting impurity interactions (small impurity concentrations). (Reference [109])

concentration, excitation intensity, *etc.* Eight of the nine lines indicated have been at least tentatively identified in GaAs. Additional emission lines due to excited states, two-electron transitions, and acoustical and optical phonon replicas are also expected and observed[109]. Phonon and zero-phonon lines can be distinguished by comparing their absorption and luminescence energy positions. At low temperatures, phonon emission is much more probable than phonon absorption. While zero-phonon lines occurs at the same energy in absorption and emission, phonon-assisted lines are shifted by $2\hbar\omega_{ph}$ above the zero-phonon line in absorption, where ω_{ph} is phonon energy. At higher temperatures, phonon absorption can become comparable to phonon emission rates. Then phonon wings can occur both ω_{ph} above and ω_{ph} below the zero-phonon line (which may be absent) in absorption and luminescence spectra.

Photoluminescence has proved itself to be a very good tool for the assessment of semiconductor materials. For example, it can characterize impurities and native defects even at very low concentration. Photoluminescence spectra depend on the technique used for crystal growth and gives information on the quality of samples. The high crystalline quality and high purity samples exhibit very strong near-band-edge luminescence. The best results have been obtained on epitaxial films.

Fourier transform photoluminescence (FTPL) spectra were obtained for all the InP samples given in Table 3-1. A typical low-temperature luminescence spectrum is shown in Figure 3-7 for sample #2723. Four bands, peaking at 1.416, 1.401, 1.389 and 1.380 eV were easily identifiable. Another very broad and low intensity rise centered near 1.355 eV was also observed in all samples. The relative intensities of these bands are changed from sample to sample. To get more information about the correlation between luminescence intensity and impurity concentration and to obtain more accurate parameters of the luminescence peaks, all the spectra were decomposed into elementary peaks by using a commercial Spectra Calc curvefit program (Galactic Industries). It was assumed that there are four elementary peaks in the entire spectrum which have Lorentzian shape and are fully characterized by their three first

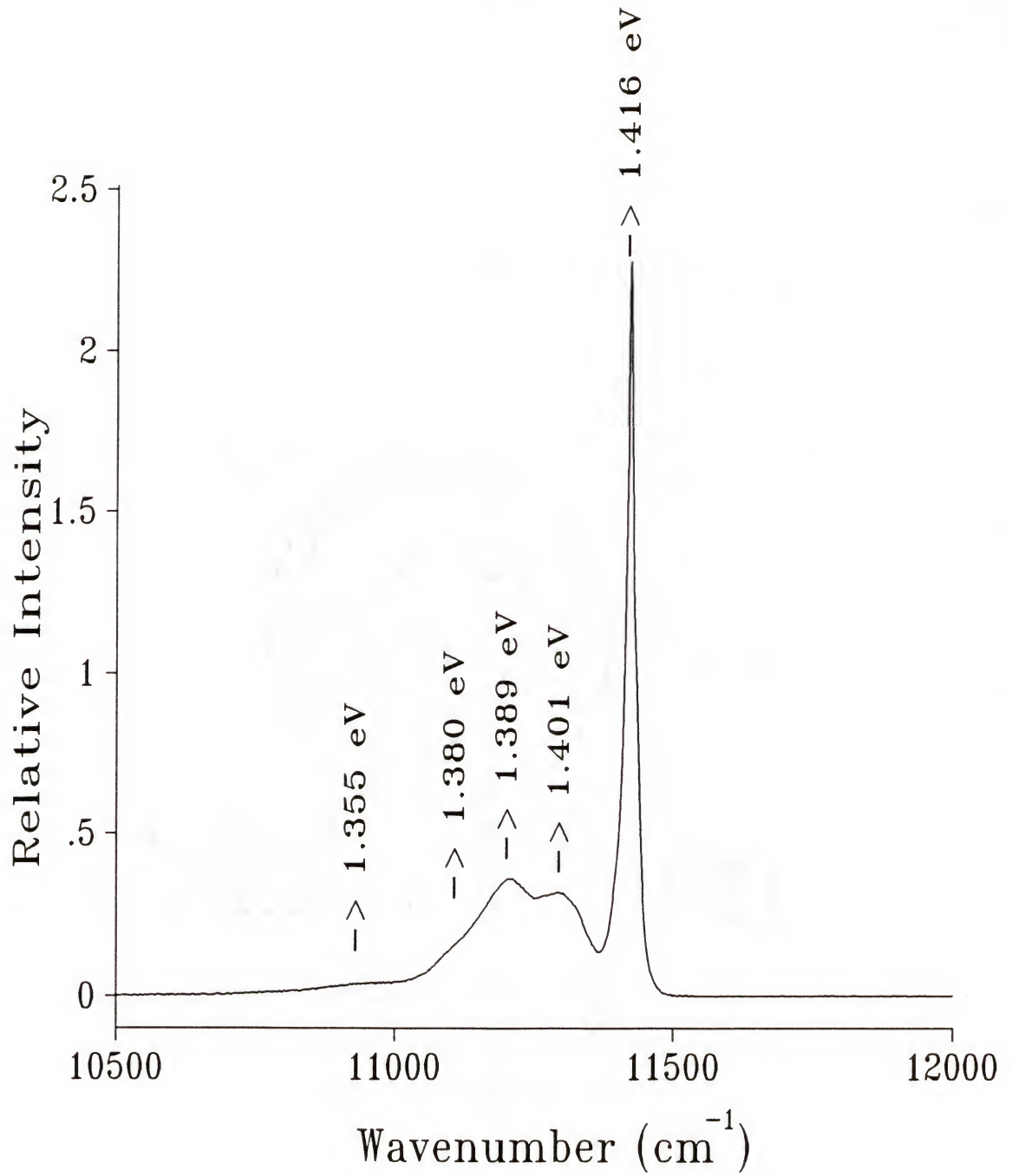


Figure 3-7: FTPL spectrum of sample #2723: $T = 4.2$ K; 0.18 W/cm²; 2 cm⁻¹.
Growth conditions are given in Table 3-1.

momenta, *i.e.*, area under the curve, position, and full width at half maximum (FWHM) of the elementary peaks. No other restrictions were made for the curvefit. The curvefit was very good for all the spectra, and the parameters obtained are listed in Table 3-3. The peak positions and their FWHM values of the elementary peaks did not change significantly for different samples, even though the entire spectrum changed its shape as a function of process parameters, indicating the consistency of the curvefit procedure. The change in shape of the entire spectrum was caused by the change in the areas of the elementary peaks. The area under peak curve is proportional to the concentration of the luminescence centers, and therefore it directly provides information on the impurity concentration.

Figure 3-8 shows a comparison between two different FTPL spectra for samples grown with different source zone temperature. It is obvious that the increased source zone temperature causes a remarkable change in the spectrum, and this is due to the increased area of peak #3 at 1.389 eV and peak #4 at 1.380 eV as shown in Table 3-3. This is also consistent with the high background carrier concentration obtained in the sample #2729 (Table 3-2). The area of peak #1 at 1.416 eV and peak #2 at 1.401 eV did not change significantly in these two samples. Figure 3-9 compares the two FTPL spectra of InP samples grown with different inlet mole fractions of HCl. Again, the area of peak #3 and peak #4 decreased with increased x_{HCl}^0 . This is also consistent with the decreased carrier concentration of the sample #2718. However, no apparent change in FTPL spectra was observed when the inlet mole fraction of PH_3 was varied.

The peak positions of the spectra were carefully compared with the published photoluminescence spectra of InP films grown by various techniques such as the LEC[112,122,124], the LPE[112,123], the hydride VPE[76,112], the chloride VPE[113-115], the OMCVD[105,116-120], and the MBE[121]. At the first sight we can see that elementary peaks which we obtained by decomposition of our experimental spectra are much broader than many results given in the literature. The purest samples ($n < 10^{14} \text{ cm}^{-3}$) reported in the

Table 3-3: Parameters of Elementary Peaks of FTPL Spectra.
($T = 4.2 \text{ K}$; 0.18 W/cm^2 ; 2 cm^{-1})

Sample No.	Peak #1			Peak #2			Peak #3			Peak #4		
	Pos. (eV)	FWHM (meV)	Area	Pos. (eV)	FWHM (meV)	Area	Pos. (eV)	FWHM (meV)	Area	Pos. (eV)	FWHM (meV)	Area
#2723	1.416	2.33	60.9	1.401	9.91	28.0	1.390	12.91	41.2	1.381	17.29	21.9
#2715	1.416	2.76	99.6	1.401	9.67	25.7	1.389	12.76	35.6	1.378	13.08	15.7
#2725	1.416	2.95	70.5	1.401	9.05	21.0	1.389	12.58	34.7	1.380	15.92	18.6
#2729	1.416	3.87	64.9	1.399	10.20	29.7	1.388	12.87	118.1	1.380	18.54	97.5
#2721	1.416	2.79	74.8	1.401	9.22	29.7	1.389	12.74	53.8	1.380	15.74	26.7
#2718	1.416	2.76	66.6	1.401	10.63	19.4	1.389	12.45	24.5	1.379	15.21	10.1

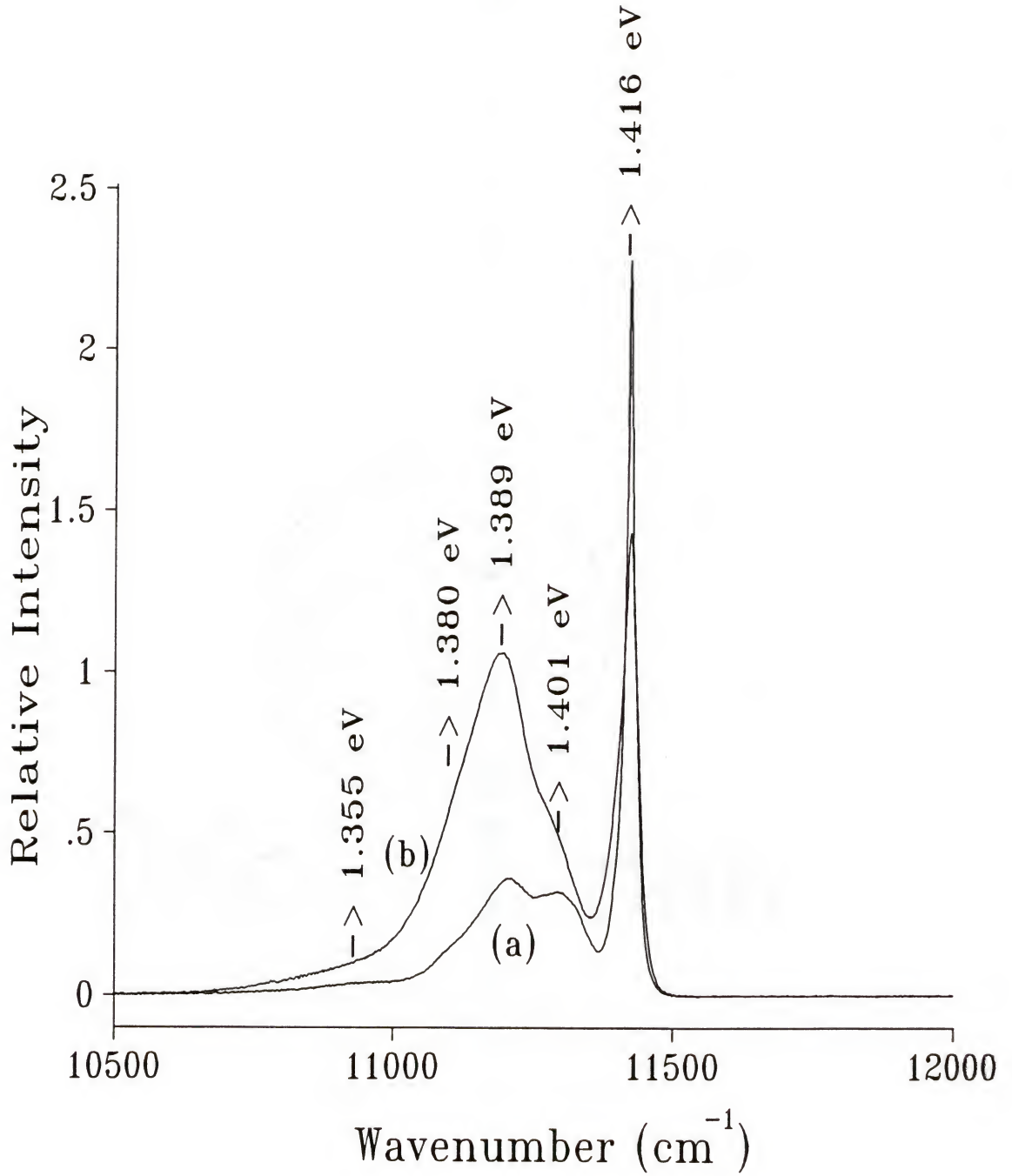


Figure 3-8: FTPL spectra of sample (a) #2723 ($T_s = 770^\circ\text{C}$) and (b) #2729 ($T_s = 887^\circ\text{C}$):
 $T = 4.2\text{ K}$; 0.18 W/cm^2 ; 2 cm^{-1} . Other growth conditions are given in Table 3-1.

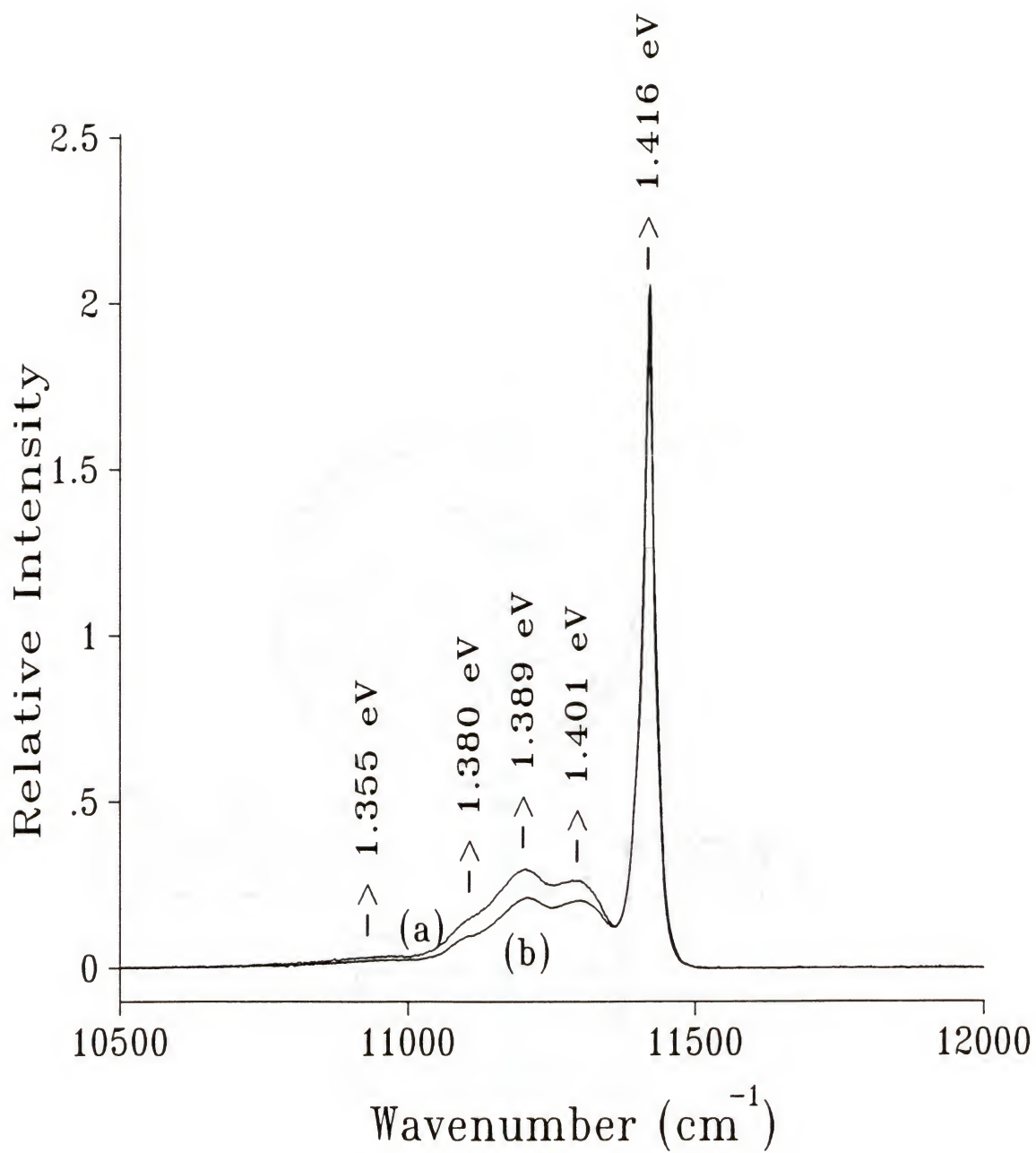


Figure 3-9: FTPL spectra of sample (a) #2725 ($x_{\text{HCl}}^{\circ} = 4.739 \times 10^{-3}$.) and (b) #2718 ($x_{\text{HCl}}^{\circ} = 14.085 \times 10^{-3}$): $T = 4.2 \text{ K}$; 0.18 W/cm^2 ; 2 cm^{-1} . Other growth conditions are given in Table 3-1.

literature[76,117] show a lot of very narrow lines. The large width of peaks in our case is due to relatively high impurity concentration which is also supported by electrical measurements discussed previously. At high carrier concentration ($> 3 \times 10^{16} \text{ cm}^{-3}$), the donor levels form a band. This fact complicates the assignment of the peaks because usually it is possible to find several peaks in the literature whose frequencies fall in the region of our broad peaks. The assignment of the five bands observed in this study was made according to the survey: peak #1 at 1.416 eV - an exciton bound to impurity level, D^+x or A^0x ; peak #2 at 1.401 eV - an excitation bound to deep level; peak #3 at 1.389 eV - donor-acceptor pairs due to Si substitution; peak #4 at 1.380 eV - an exciton bound to deep level (Zn), A^0_{Zn} ; Peak at 1.355 eV - phonon replica. The first two peaks are considered as tight excitons because their energies are lower than the typical values. The high impurity concentration causes that the high frequency shoulder be the only feature which remains from free exciton. The peak #3 is strongly dependent on the source zone temperature, and Si from quartz tube is a highly probable source of background doping. Zn, which is proposed to be responsible for peak #4, may come from In metal where it is present as an impurity.

The observed behavior of background doping is then clearly understood in the sense that Si acts as a major background impurity in the hydride VPE grown InP films. This study provides, for the first time, a clear experimental evidence that the background doping in the hydride VPE grown InP films agrees with the long-standing silicon incorporation model by Dilorenzo and Moore[87] and also with the thermodynamic predictions[37,100].

3.4 Summary

Background impurities in epitaxial layers of InP grown by the hydride VPE technique were studied to understand the chemistry of the unintentional doping process. The effects of source zone temperature and inlet mole fractions of HCl and PH_3 on the impurity incorporation were investigated by a variable temperature Hall measurement and a low temperature Fourier

transform photoluminescence (FTPL) spectroscopy. The background carrier concentration was found to decrease with decreasing source zone temperature and increasing HCl, but it was relatively independent of PH_3 for the range of mole fraction studied. The electrical parameters of the InP films were extracted from the temperature-dependent Hall data by performing a simple theoretical analysis. Background impurities were identified by analyzing the FTPL spectra of the InP films. It was found that Si donors and Zn acceptors are the major impurities in the hydride VPE grown InP films. The observed behavior of unintentional doping in the InP films followed the thermodynamic prediction and the Dilorenzo and Moore's Si incorporation model.

CHAPTER IV INVESTIGATION OF AN UPFLOW OMCVD REACTOR

4.1 Introduction

OMCVD (Organo-Metallic Chemical Vapor Deposition) has been one of the most important techniques to grow single or multi-heterostructures of semiconductor alloys for optoelectronic and electronic devices[125,126]. The technique is well-adapted for the growth of high purity, submicron epitaxial layers of uniform thickness and composition. In addition, it can produce abrupt composition changes in the succeeding epilayers.

OMCVD is based on the thermal cracking of organometallic compounds and hydrides on a heated substrate. In the case of InP deposition, for example, there is a co-pyrolysis of an organometallic compound, for example trimethyl indium (TMI), and phosphine (PH₃), by the following overall reaction:



The quartz reactor walls remain cold, and they provide deposition areas for the products of undesirable parasitic gas phase reactions. These reactions must be reduced as much as possible because the film uniformity and crystalline properties become poorer with the existence of these reactions. Epitaxial growth of compound semiconductors by the OMCVD technique is usually operated in the mass transport limited regime using low partial pressures of reactants and a relatively high substrate temperature. Consequently, the quality and uniformity of the deposited layers are determined largely by the gas dynamics in the reactor. The flow field in the reactor should be uniform so that deposition occurs at the same rate for

all points on the substrate. Furthermore it should be free of any laminar vortices in order to minimize gas residence time and thus maximize reactant switching times. Temperature profiles in the reactor are also crucial in achieving good epilayer qualities. Isotherms parallel to the substrate are desired to achieve uniform growth, and isotherms confined to the vicinity of the substrate are desired to minimize unwanted gas phase reactions. A large temperature gradient normal to the substrate surface can, however, produce buoyancy driven flow recirculations in the reactor causing growth rate variations, increased impurity incorporation, and graded heterojunctions[127]. Optimum design of an OMCVD reactor should be based upon the important criteria of good epilayer uniformity (thickness, composition, doping, *etc.*) and interface abruptness as well as low unintentional doping.

A stagnation point flow reactor, where cold gas flows up toward the heated substrate, is a good candidate. A stabilizing density gradient is expected with this configuration, thereby reducing the flow recirculation effects frequently encountered in other commercially adopted geometries such as horizontal and vertical downflow reactors. A mathematically well-defined experimental system can also be constructed with this geometry for kinetic studies[128]. Stagnation point flow reactors have been investigated by many workers[128-135], and their results have shown that there is a large difference in the importance of natural convection caused by the large temperature gradient in the reactor for different configurations of the reactor. Wahl[129] observed that flow recirculations developed in the entire operating range of his study and the flow patterns became more complex with the downflow geometry than with the upflow geometry. The calculated results were in good agreement with the flow visualization experiments by the $\text{TiCl}_4\text{-H}_2\text{O}$ method[136]. In their flow visualization study of vertical downflow reactor, Wang *et al.*[130] showed that the flow is strongly perturbed by thermally induced convection, which could be reduced by lowering the system pressure. They also indicated that the method of gas injection was crucial to vortex formation, which was minimized by using a porous plug. Fotiadis *et al.*[131,132] numerically examined the effects

of operating parameters, reactor geometry, and heat transfer characteristics on flow patterns and deposition uniformity, and found that two types of recirculation cells appeared in the vertical reactor, *i.e.*, natural convection and inertia driven cells. The natural convection driven cells could be reduced by increasing the inlet flow rate, rotating the susceptor, reducing the pressure, inverting the reactor, decreasing the distance between the inlet and the susceptor, introducing baffles, or reshaping the reactor wall. Some of their results were compared with flow visualization experiment; the results showed good agreement. Having an optimal reactor shape was critical to eliminating both natural convection and inertia driven cells by preventing flow separations associated with sudden expansions in the flow cross-sectional area. They also showed that an accurate treatment of the heat transfer characteristics in reactor models(*e.g.*, wall temperature) was essential to accurately predict the reactor performance. Lee *et al.*[135] actually grew GaAs using a vertical upflow OMCVD reactor and compared the experimentally observed growth rates with the calculated results. They indicated that a strong recirculation cell exists at high pressure(500 torr), but its magnitude is reduced at low pressure(15 torr). The importance of the heat transfer description of the reactor was emphasized again in explaining the discrepancies of observed growth rates from predicted ones.

Temperature distributions in OMCVD reactors have been experimentally investigated by several techniques, with Raman spectroscopy proven to be a good method for measuring the gas temperature inside a reactor[133,137-144]. Although most of the studies available in the literature were performed with horizontal reactors[136,138-143], two investigations were reported for a vertical reactor. Monteil *et al.*[133,138] studied a vertical downflow reactor by Raman spectroscopy and found that the use of a N₂ carrier gas produces a steeper temperature gradient normal to the susceptor surface than the use of a H₂ carrier gas. Susceptor rotation and increasing flow rate were found to improve the temperature uniformity close to the

susceptor. However, the vertical reactor with an upflow geometry has not been studied by this technique.

Understanding the transient switching response of the reactor is very important in achieving abrupt interfaces and in designing and controlling the growth runs. Sillmon *et al.*[145] used IR-diode laser spectroscopy to study the flow dynamics of gas switching systems in a vertical downflow reactor. Their results showed that extreme care must be taken in the design and operation of a conventional vent/run system to avoid distortions and instabilities of source concentrations in the reactor. The importance of gas pressure imbalance and dead space in the injection system was also emphasized. Hebner *et al.*[146] used UV absorption spectroscopy to study both a vertical upflow and a horizontal reactor. They found that the equilibration time for steady state flow conditions was decreased by increasing the carrier flow, decreasing the pressure, or decreasing the cross-section of the flow tube. The effects of dead volume in the system on the flow characteristics was also studied, and the utility of the technique was demonstrated by adjusting the flow conditions to reduce concentration gradients produced by improper settings on the downstream pressure control. Haspeklo *et al.*[147] studied the transient response of a horizontal reactor by mass spectroscopy, and found that the resolution of a pulse sequence of reactive gases was improved by using a low reactor pressure.

In this investigation, a vertical upflow OMCVD reactor was experimentally studied, and the results were compared to numerical predictions. The ultimate goal is to construct a mathematically as well as experimentally well-defined system for the study of reaction rates and consequently, the growth of InP epitaxial layers. Special focus was placed on the axial temperature profiles near the susceptor surface and the behavior of reactants in the reactor. The temperature of the gas inside the reactor was measured by pure rotational Raman scattering from the carrier gas molecules, N_2 or H_2 , as a function of the inlet flow velocity and aspect ratio. A two-dimensional axisymmetric model of the actual reactor geometry was

developed and used to predict the experimental observations. Vibrational Raman scattering from a tracer species, CH_4 , was used to investigate the behavior of reactants in the reactor. The use of a sweeping flow was investigated as a method of preventing the wall depositions. The transient switching response of the reactor was also studied, and the importance of the design of gas inlet is emphasized based on the results. Further improvements in the reactor design and modeling are suggested and discussed for the study of reaction rates and the growth of InP epitaxial layers.

4.2 Experiment

4.2.1 Experimental System

An upflow OMCVD reactor was designed and built. A schematic of the reactor is shown in Figure 4-1 with appropriate physical dimensions. It resembles the reactor used by Wahl[129], but the capability of sweeping flow was added to this reactor design. The reactor body was made of optically flat quartz and had a square cross-section to minimize the position-dependence of scattered light intensity due to irregular surface scattering. A cylindrical quartz tube was inserted into the reactor for the study of temperature profiles and the transient response of the reactor to simplify the reactor model and simulate a practical geometry. Four slits were open on the inserted tube which are symmetric to the centerline of the reactor. These slits permitted access of the laser beam to the reactor and to gather the scattered light from the reactor. Experimental measurements were performed along the centerline of the reactor. For the study of reactant behavior in the reactor, however, the insert was removed, and the reactor could be scanned in three directions. The reactor bottom and top parts were made of stainless steel 316 and had circular cross-sections. Viton O-rings were placed between the quartz and stainless steel to seal the reactor from the outside environment. The furnace, which is termed a "quartz envelope heater", was intruded from top of the

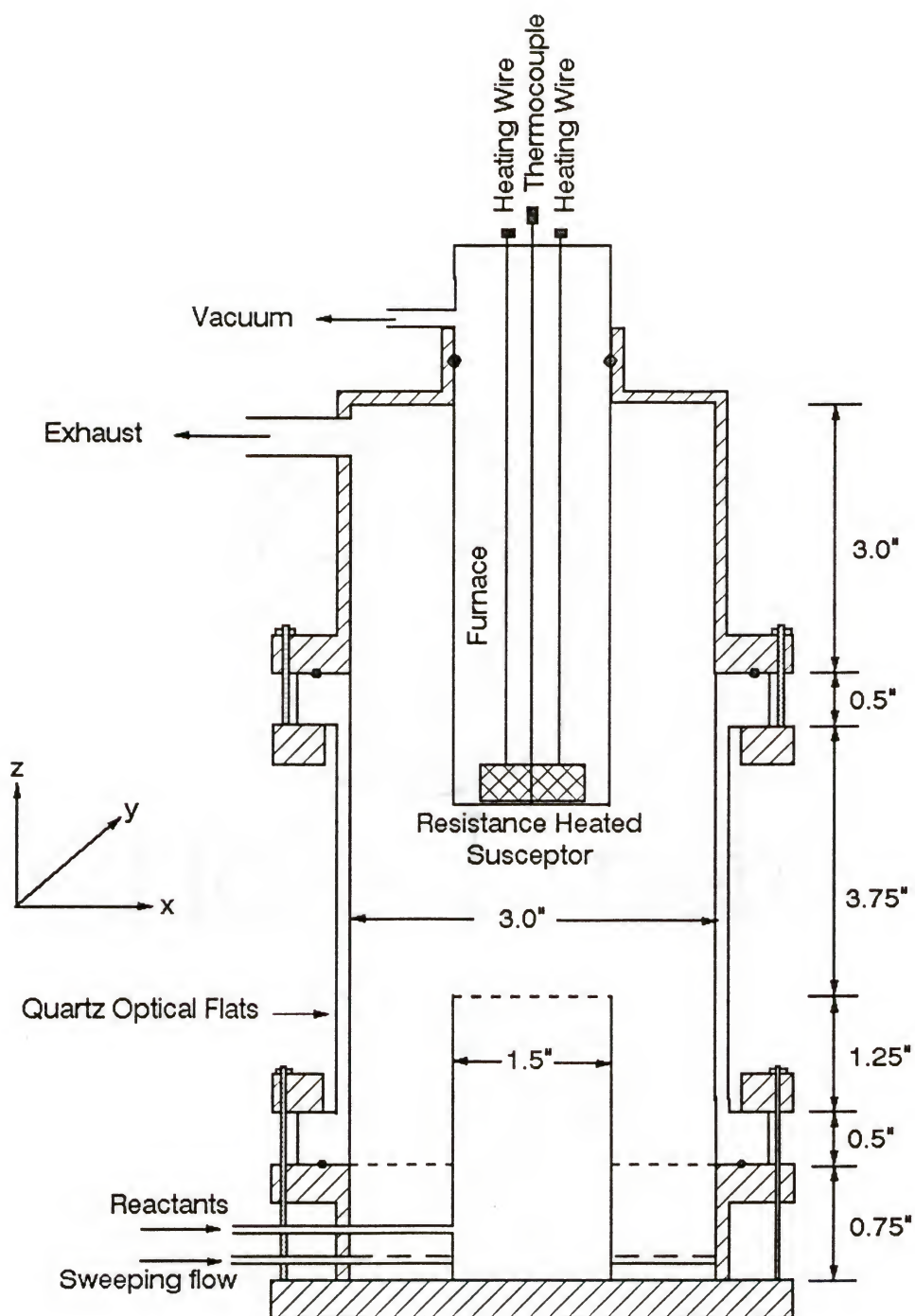


Figure 4-1: Schematic of a vertical upflow OMCVD reactor.

reactor. It contains a heating block which is heated by resistance heating. The body of the furnace was made of quartz with cylindrical shape (1.5" in O.D.), and the inside of the furnace was kept under vacuum (< 1 mtorr) by a diffusion pump to insulate the heating block from surroundings. The heating block makes a physical contact with the inside bottom of the furnace body. The set point temperature of the furnace was measured at the inside bottom wall of the furnace body by a K-type thermocouple, and the temperature was maintained at 650 °C for all experiments in this study except for the room temperature experiments. Details of the furnace design can be found elsewhere[148,149]. The aspect ratio (AR), which is defined as the ratio of the distance between the susceptor and the center inlet tube to the center tube diameter, could be varied by moving the furnace up or down. The carrier gas, N_2 or H_2 , was introduced into the reactor through 0.25" stainless steel tubings connected to the center and outer inlet tubes. A straight tube was directly connected to the center inlet tube, whereas a tube was inserted through the outer inlet tube and wound around the center tube. The end of the tube was capped and many small holes were opened on the tube to provide an uniform sweeping flow around the center flow. Stainless steel screens were placed on top of both inlet tubes to produce a linear velocity profile at each gas inlet. CH_4 was introduced into the reactor through the center tube whenever it was needed. The reactor was situated in the macro-chamber of the Raman spectrometer, and the whole reactor could be moved in three directions by a micrometer controlled x-y-z stage. The operating pressure of the reactor was kept at 1 atm for this study.

The flow system used in this study was a conventional OMCVD system which is capable of flowing group V reactants as hydrides and group III reactants as organo-metallic compounds. A schematic description of the system is shown in Figure 4-2. The system has a vent/run capability for reactant switching, and it also contains the make-up carrier gas flow lines to minimize flow disturbance during the switching operation. Organo-metallic sources were contained in stainless steel bubblers immersed in constant temperature baths as liquids.

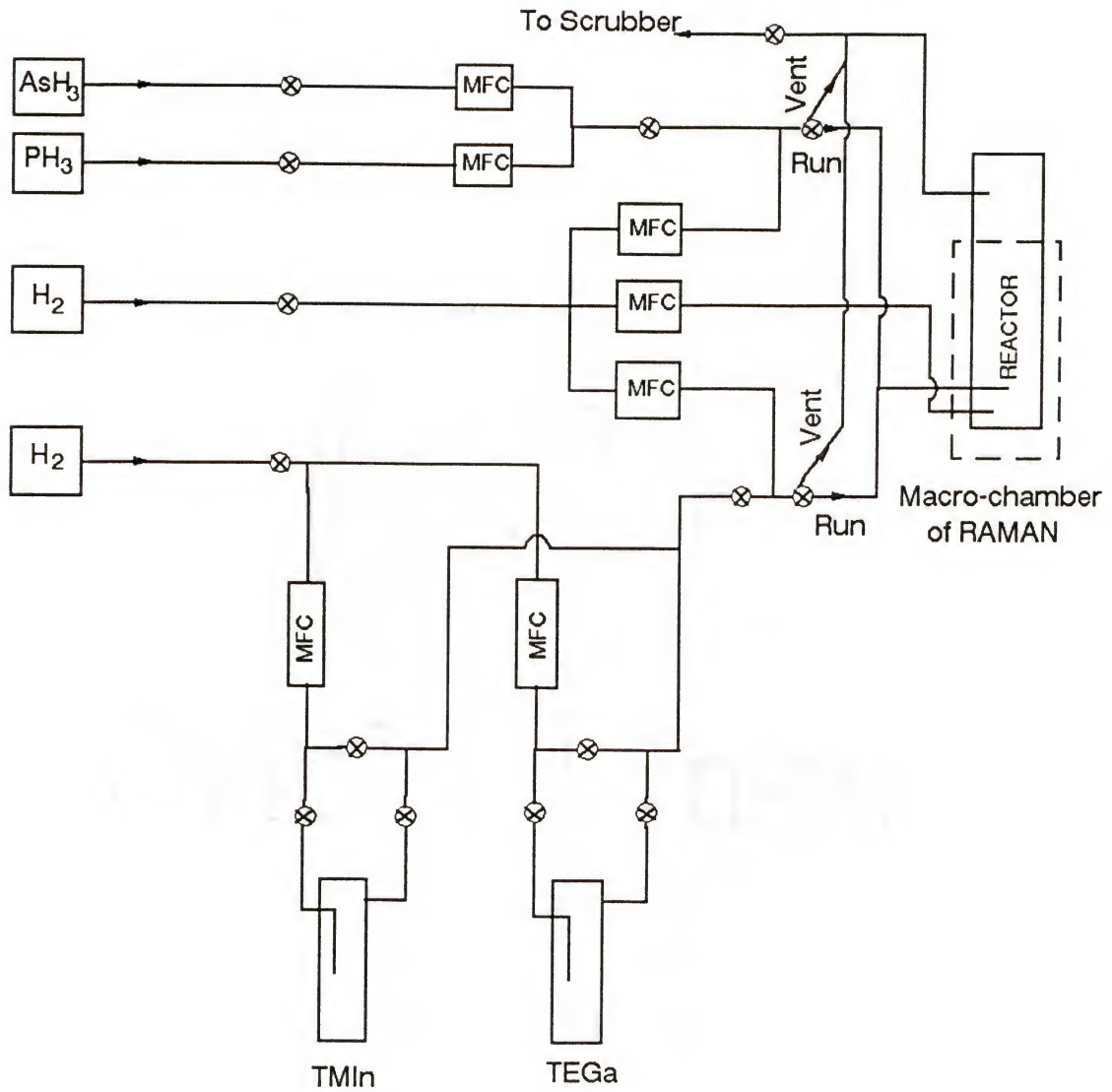


Figure 4-2: Schematic of the OMCVD system.

Metered quantities of high purity palladium-alloy diffused hydrogen acted as a carrier gas by passing through the liquid to transport the reactant organo-metallics to the reactor. Hydride sources were held in high pressure gas cylinders. Organo-metallics, hydrides, and hydrogen carrier gas flow through a network of high-purity welded stainless steel tubing and mix in the vapor phase at the entrance to the reactor. CH_4 was introduced through the organo-metallic line, and N_2 was replaced with H_2 whenever needed. The exhaust of the reactor was connected to an exhaust scrubber, and the scrubber exhaust was connected to the room vent, which was isolated from the vent in other rooms, pulled the room air and the treated reactor exhaust to the outside of the building. The exhaust scrubber was a commercial unit (Advanced Concepts, model 9625). It was a liquid based scrubber designed to scrub toxic gases and exhaust clean gases to the atmosphere. The scrubbing solution consisted of a 80:5:2 by volume mixture of water, 15% sodium hypochlorite, and 50% sodium hydroxide. The room air and reaction chamber were constantly monitored by a MDA toxic gas detector as well as a ppm scale hydrogen detector. The flow system also had sensors for gas line pressure at several locations. If one of these sensors was activated, the system was instructed to close all the gas line valves and turn on an audible/visual alarm.

A Ramanor U-1000 Raman spectrometer (ISA, Inc.) was used in this study, and its schematic is shown in Figure 4-3. It is a conventional Raman spectrometer with a double monochromator and is capable of analyzing gas, liquid, or solid samples. In this investigation, the reactor was situated in the macro-chamber, and the Raman scattering was performed in a 90° configuration. The excitation laser was introduced in the -x direction (Figure 4-1), and the scattered light was detected in the +y direction forming a xy scattering plane. The cw argon ion laser of wavelength at 488 nm was used as the excitation source with laser power of 1 W. Polarization of the incident laser was in the z direction, but the scattered light polarization was not analyzed. A photomultiplier tube (PMT) was used as a detector, and

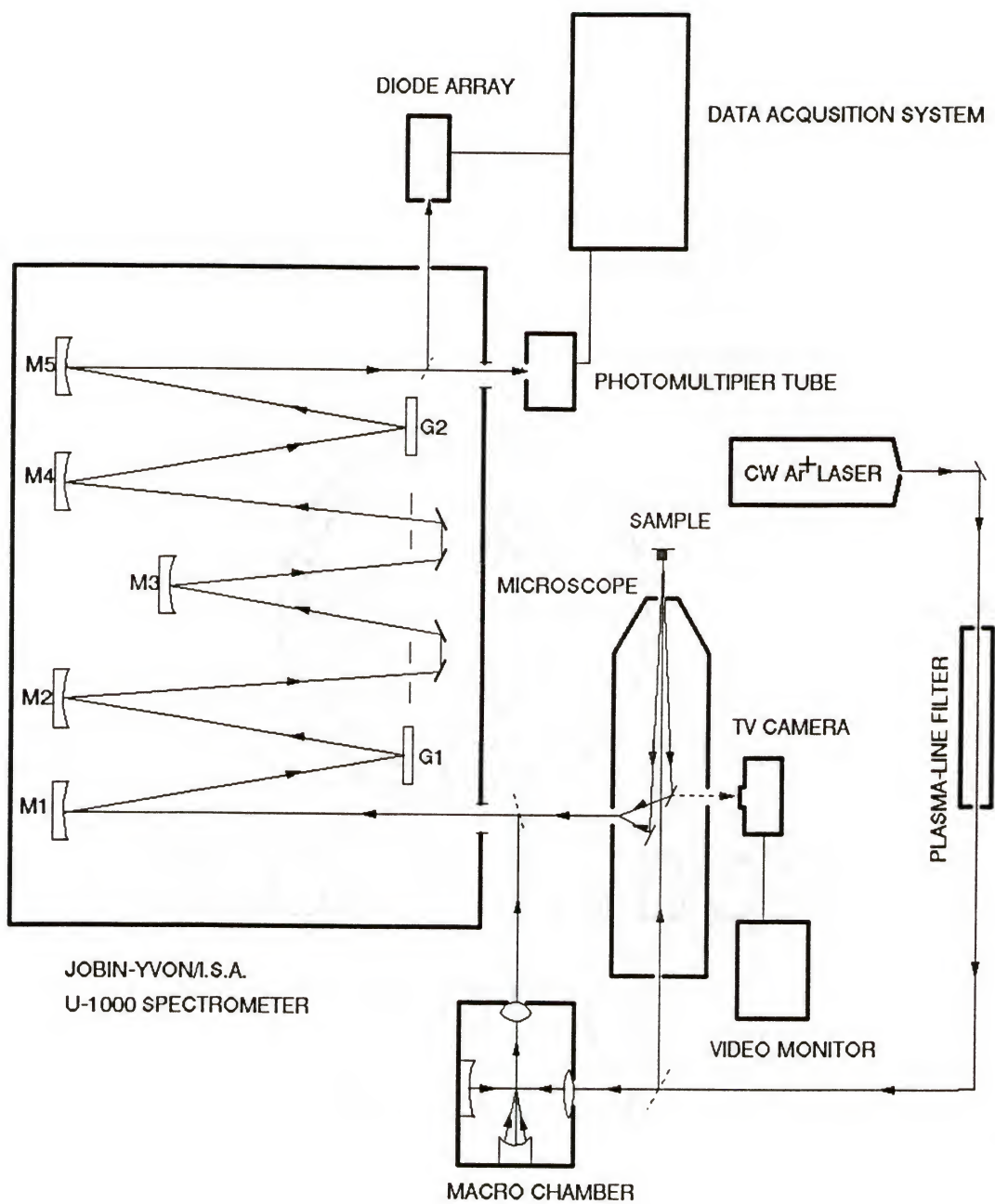


Figure 4-3: Schematic of the laser Raman spectrometer system.

photon counting electronics were employed. Control of the spectrometer and data processing were done by an IBM compatible Personal Computer (PC).

4.2.2 Temperature Measurement

The temperature distribution in the reactor was measured by pure rotational Raman scattering from the carrier gas molecules flowing inside the reactor. This technique has the advantage of not disturbing the flow field as compared to the use of a thermocouple[150], and it provides a spatial resolution in three dimensions better than interference holography[151]. In this investigation, the spatial resolutions of about 30 μm in the y and z direction and about 3000 μm in the x direction could be obtained, where the values were calculated with the assumption of a focal cylinder[152]. In addition, measurements as close to the susceptor surface as 0.3 mm could be performed. The determination of the origin could be easily reproduced by monitoring the intensity decrease pattern as the laser path intersected with the edge of the susceptor surface upon translation in the +z direction.

The theory of Raman scattering is very well developed for diatomic molecules[152]. Assuming thermal equilibrium for the rotational modes (Boltzmann equilibrium distribution function), one can obtain the equations describing the scattering intensities for rotational Raman scattering from an assembly of randomly oriented (*e.g.*, gas) diatomic molecules[153]. The assumption of thermal equilibrium is reasonable in this study since the temperature and pressure are high. For a total number of N molecules in their non-degenerate electronic and vibrational ground state, the pure rotational Raman scattering intensity for a transition between a state characterized by quantum number J to state J+2 ($I_{J \rightarrow J+2}^{\text{meas}}$), with a 90° scattering configuration (xy scattering plane) and vertical polarization (z) of the incident laser, can be written as follows:

$$\ln \left[\frac{I_{J \rightarrow J+2}^{\text{meas}} R(\tilde{\nu})}{(\tilde{\nu}_o - \varepsilon \tilde{\nu}_o')^3 S(J) f(J) g_J} \right] = \frac{hc}{k_B T} F(J) + \ln \left[\frac{2^4 \pi^4 N}{45 hc} \frac{7(\gamma_o')^2 C_{\text{exp}}}{Q_R} I_o \right] \quad (4-2)$$

with

$$\tilde{\nu} = \tilde{\nu}_o - \varepsilon \tilde{\nu}_o' \quad (4-3)$$

where $\tilde{\nu}_o$ is the incident laser frequency (20492 cm⁻¹); $\tilde{\nu}$ is the scattered light frequency; $\tilde{\nu}_o'$ is the wavenumber shift associated with a pure rotational transition (J→J+2); and $\varepsilon = +1$ for a Stokes line and $\varepsilon = -1$ for an anti-Stokes line; In equation (4-2), S(J) is the Raman line strength.

$$S(J) = \frac{3(J+1)(J+2)}{2(2J+3)} \quad (4-4)$$

F(J) is the energy of the rotational level as given by,

$$F(J) = B_o J(J+1) - D_o J^2(J+1)^2 + H_o J^3(J+1)^3 \quad (4-5)$$

The rotational constants were the experimentally determined values. For N₂[157], B_o = 1.989574 cm⁻¹, D_o = 5.76×10⁻⁶ cm⁻¹, and H_o = 0. For H₂[158], B_o = 59.3357 cm⁻¹. D_o = 0.0458 cm⁻¹, and H_o = 4.65×10⁻⁵ cm⁻¹.

$$\begin{aligned} \tilde{\nu}_o' &= F(J+2) - F(J) \\ &= (4B_o - 6D_o + \frac{27}{4}H_o)(J+\frac{3}{2}) - (8D_o - 34H_o)(J+\frac{3}{2})^3 + 12H_o(J+\frac{3}{2})^5 \end{aligned} \quad (4-6)$$

$$Q_R = \sum_J g_J (2J+1) \exp[-hcF(J)/k_B T] \quad (4-7)$$

The term f(J) is a correction term to the anisotropy of polarizability tensor, $(\gamma_o')^2$, and it accounts for the effect of molecular non-rigidity. For N₂[154], this function is given by,

$$f(J) = 1 + 4\chi^{-1}(B_e/\omega_e)^2[J(J+1) + (J+2)(J+3)] \quad (4-8)$$

where $\chi = 0.45$ and $B_e/\omega_e = 8.476 \times 10^{-4}$ [155]. In the case of H_2 , this term has been shown to be substantially different from 1, and the experimentally determined values[156] were used.

The term g_J is the nuclear spin degeneracy. For N_2 , $g_J = 3$ for odd J and $g_J = 6$ for even J . For H_2 , $g_J = 3$ for odd J and $g_J = 1$ for even J . The h and k_B are the Planck and Boltzmann constants, respectively; c is the speed of light, T is the temperature in Kelvin; I_o is the irradiance of the incident laser (power density); Q_R is the rotational partition function; C_{exp} is an experimental constant which accounts for the efficiency of the detection system as determined by the geometry of the collection optics, slit widths, spectrometer f value, phototube characteristics, etc. $R(\tau)$ is the spectral response of the spectrometer and detection system and was obtained by using a standard tungsten strip lamp traceable to the National Bureau of Standards[159].

Figure 4-4 and Figure 4-5 show typical examples of pure rotational Raman spectra for N_2 and H_2 , respectively. The spectra were obtained with a laser excitation of 1 W at the wavelength of 488 nm, 1.5 cm^{-1} resolution, and 1 second integration time. Spectrometer frequencies were calibrated by a neon emission line at 5400.6 \AA . In the case of N_2 , transitions from $J = 0$ to 20 are clearly observed, where J represents the rotational quantum number of the initial level for the Stokes band and the final level for the anti-Stokes band. The 2:1 intensity alternation is due to the nuclear spin. For N_2 , the Stokes bands alone were sufficient to determine the temperature. For H_2 , however, only four Stokes and two anti-Stokes bands had a significantly large signal to noise ratio to be useful. Thus all 6 bands were included in the analysis to determine the temperature. The intensity was measured from the height of the band, and the temperature was determined from a linear least-squares fit of the experimental data by using equation (4-2) with equations (4-3) to (4-8). Figures 4-6 and 4-7 show two examples of such a data-fit for N_2 and H_2 , respectively. The data obtained in this study

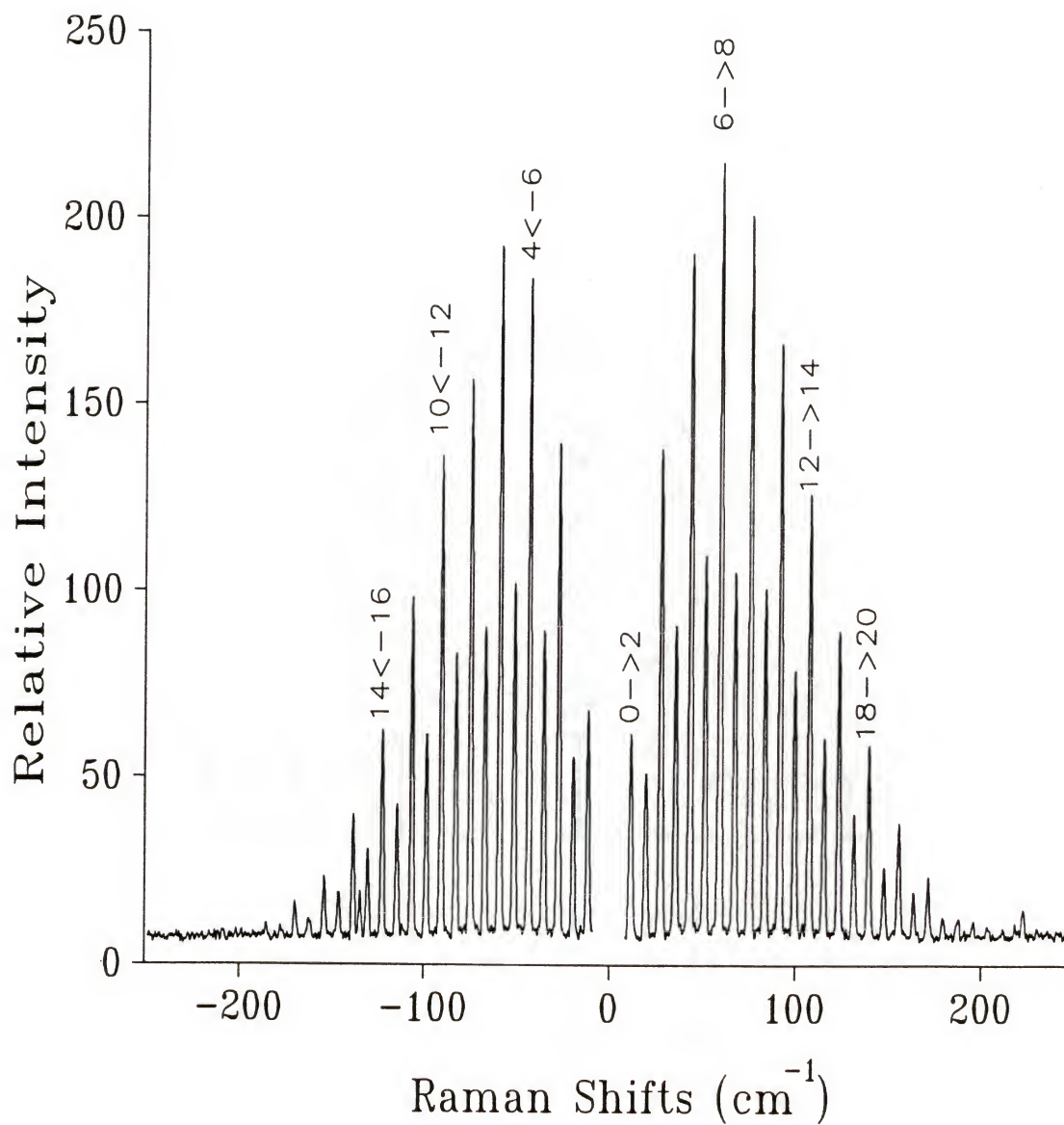


Figure 4-4: Pure rotational Raman spectrum of nitrogen at 25 °C and 1 atm:
 Laser excitation was 1 W at 488 nm; The monochromator slit widths were 150 μm
 (1.5 cm⁻¹ resolution); and the integration time was 1 s.

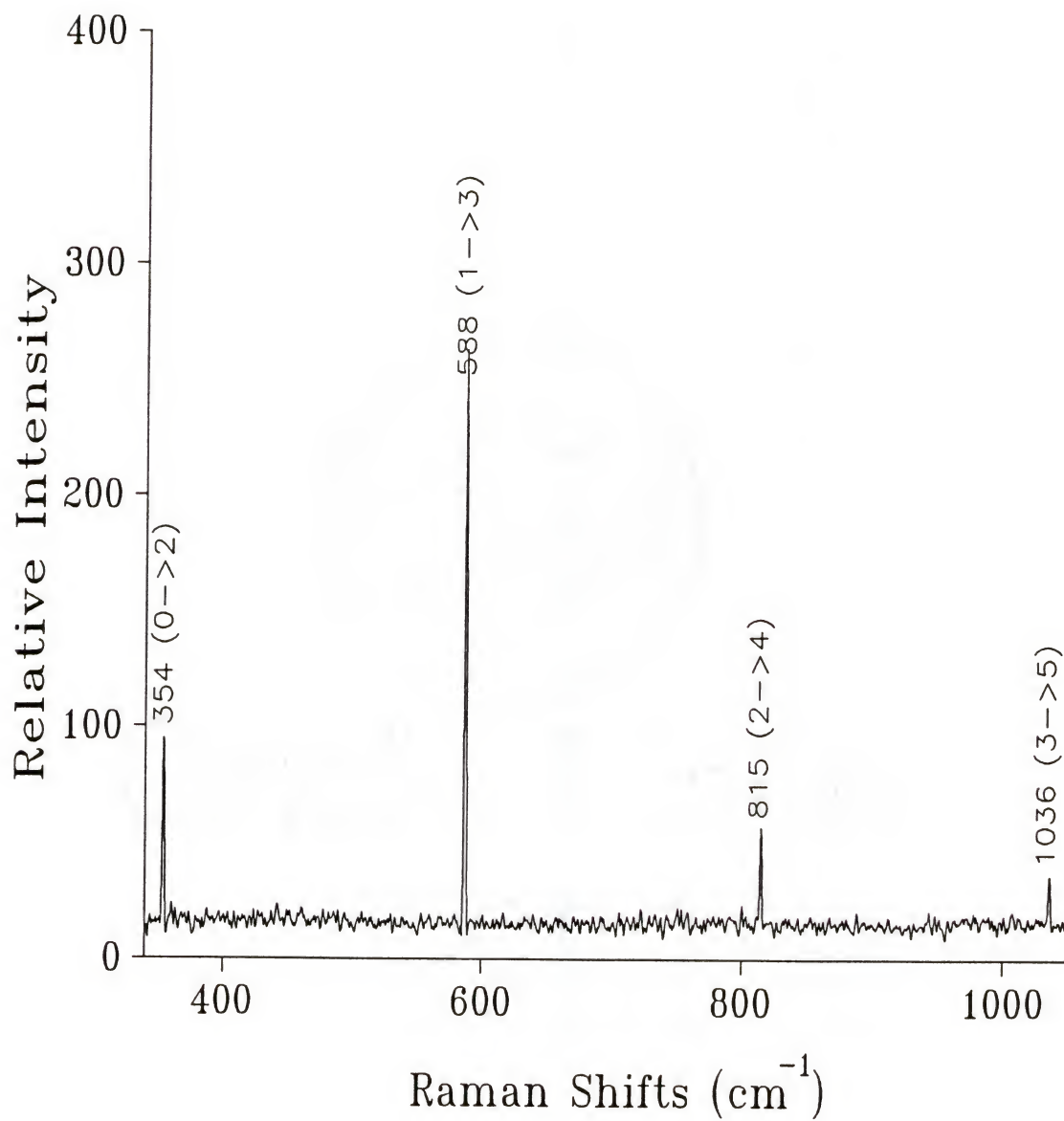


Figure 4-5: Pure rotational Stokes-Raman spectrum of hydrogen at 25 °C and 1 atm:
Laser excitation was 1 W at 488 nm; The monochromator slit widths were 150 μm
(1.5 cm^{-1} resolution); and the integration time was 1 s.

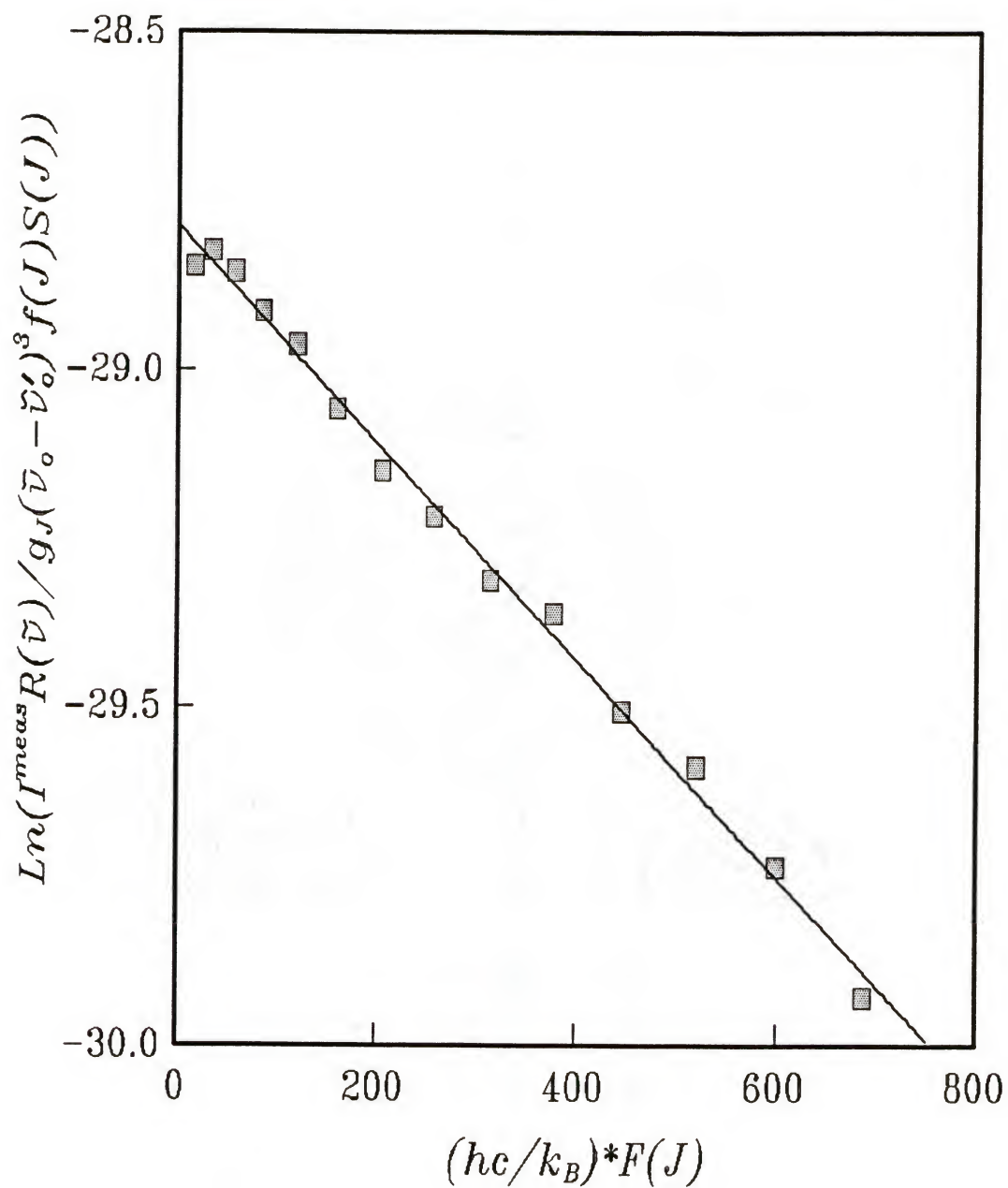


Figure 4-6: A plot of the left hand side of equation (4-2) as a function of $hc/k_B F(J)$ for N_2 :
 The slope of this line is equal to the reciprocal of the absolute temperature ($T = 347.9 \text{ }^\circ\text{C} \pm 12.9 \text{ }^\circ\text{C}$). The uncertainty was one standard deviation calculated from the linear least-squares fit of line.

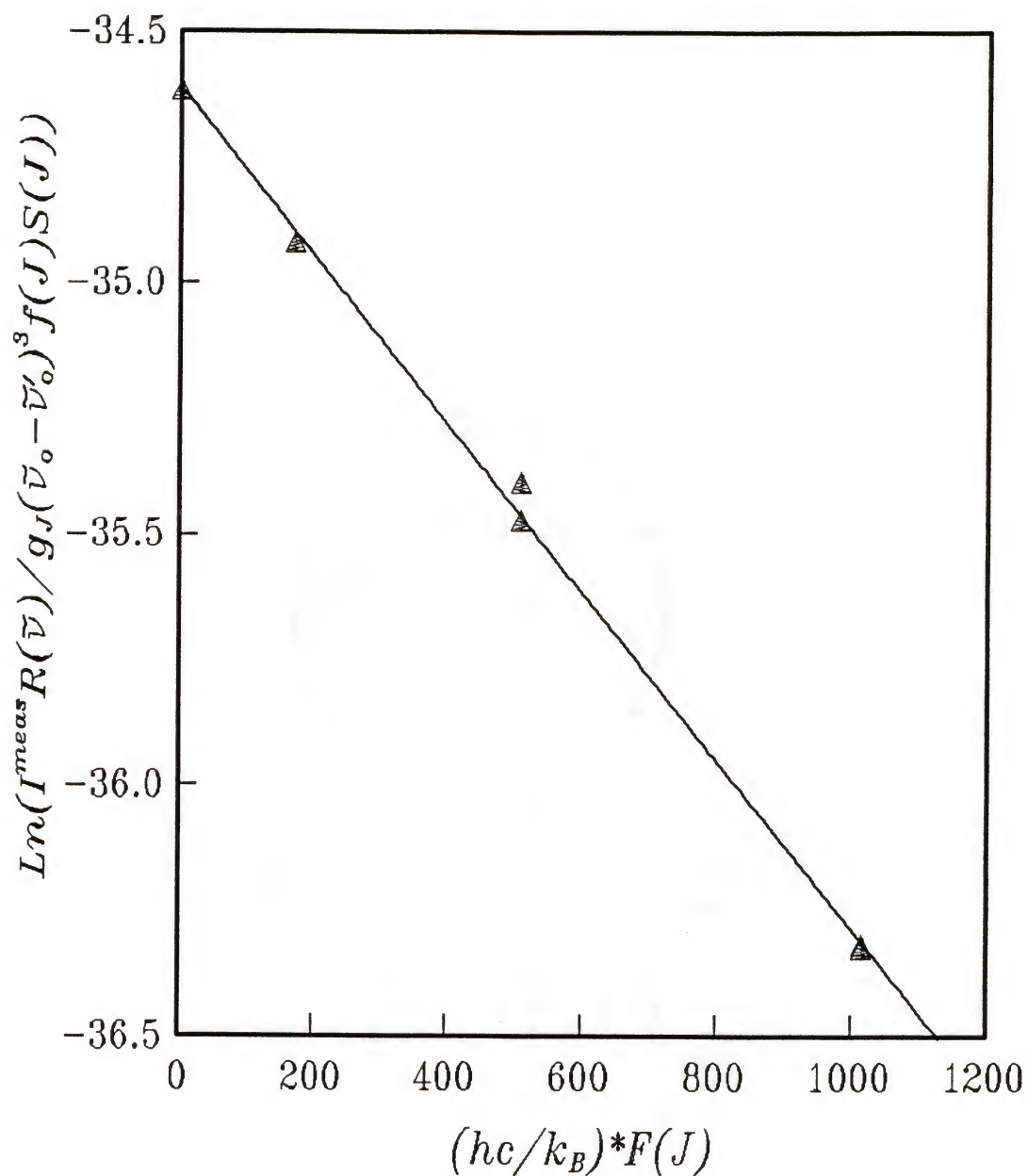


Figure 4-7: A plot of the left hand side of equation (4-2) as a function of $hc/k_B F(J)$ for H_2 :
 The slope of this line is equal to the reciprocal of the absolute temperature ($T = 324.1 \text{ }^\circ\text{C} \pm 13.8 \text{ }^\circ\text{C}$). The uncertainty was one standard deviation calculated from the linear least-squares fit of line.

showed a very good linear relationship, indicating that the assumption of a Boltzmann population of the occupied rotational energy levels was reasonable. The accuracy of the measured temperature depends on the signal to noise ratio which decreases with increasing temperature. When the furnace temperature was higher than 800 °C, the radiation from the heating block increased the noise level, especially when the laser probe was near the susceptor surface. At the furnace temperature of this study (650 °C), the radiation was insignificant, and the spectra obtained in this study had sufficient signal to noise ratios ($> 8:1$). Uncertainty of the temperature was defined as the one standard deviation as calculated from the linear least-squares fit of the line; it was less than ± 20 °C for most cases of this study. The temperature of N_2 was more accurately determined than that of H_2 , because more data points were available for N_2 .

4.2.3 Tracer Experiment

The structure of reactant streamlines in the reactor was investigated by using an inert molecular tracer species, CH_4 , which was introduced with the center inlet carrier gas flow. This technique has the advantage of monitoring the behavior of the tracer species in the reactor even at high temperatures compared to the frequently used flow visualization technique using tracer particles (*e.g.*, micro-sized TiO_2 particles[136]). The particle tracer method is not accurate in the presence of high temperature gradients because of the thermophoretic transport of particles from hot regions towards cold regions. The CH_4 tracer technique also has the advantage of higher spatial resolution compared to interference holography[151] which only gives the spatially averaged density gradients. Nevertheless, care must be taken in interpreting the experimental observation by the molecular tracer technique, since the dispersion of the tracer species may be significant.

Both the center inlet flow and the annular sweeping flow (no tracer) were established for 5 min to achieve steady state conditions, and the whole reactor was scanned from $y = 0$ (center of the susceptor) to $y = +34$ mm (4 mm from the reactor wall) at fixed values of $z = 4, 11, 18,$ and 27 mm as measured from the center tube inlet. The aspect ratio (AR) was fixed at the value of 0.9. The Raman probe frequency was set at 2917 cm^{-1} which corresponds to the symmetric stretching vibrational frequency of the C-H bond. The height of the band at 2917 cm^{-1} was used to monitor the intensity of CH_4 signal for the room temperature experiment since it is directly proportional to the number density of CH_4 in the probe volume. The mole fraction of CH_4 had to be measured when there exists a temperature profile in the reactor to account for the thermal expansion of the gas molecules. The mole fraction of CH_4 was determined from the ratio of the area of CH_4 vibration band divided by the relative differential scattering cross-section of CH_4 (8.233)[153] with respect to N_2 , to the sum of the area of CH_4 vibration band and the carrier gas (N_2 or H_2) vibration band which is divided by its relative differential scattering cross-section[153] with respect to N_2 . A mole fraction of 0.046 CH_4 in N_2 was measured by this method for a nominal input mole fraction of 0.05 CH_4 in N_2 as adjusted by the mass flow controllers.

The transient switching response of the reactor was also investigated by using the molecular tracer species method. The laser probe was fixed at the vertical positions of 2 mm or 12 mm from the susceptor surface with a fixed lateral position ($y = 0$, centerline of the reactor). The center inlet flow containing the CH_4 was switched on or off by using the vent/run 3-way valves (see Figure 4-2). The rise and fall of the CH_4 signal (2917 cm^{-1}) was monitored as a function of the operating parameters such as the inlet gas flow velocity and the velocity ratio of center flow to sweeping flow. A make-up flow containing only the carrier gas was turned on at the same time the center flow was turned off. The make-up flow had the same velocity as the center flow velocity to minimize the flow disturbance during the

switching operation. The annular sweeping flow was continuously flowing. The upstream gas line pressures were controlled at a constant value to minimize differential pressure effects.

4.3 Reactor Modeling and Simulation

A 2-dimensional axisymmetric stagnation point flow model was developed. The result obtained was used to compare with the experimentally observed temperature profiles. The model, in turn, can serve as a preliminary for the comprehensive model, which will be developed in the future, for extracting the kinetic data from the kinetic experiment measuring the reaction rates.

Modeling a real OMCVD process requires solving the balance equations for momentum, mass, energy, and species simultaneously. The problem however can be simplified due to the typical operating conditions involved in most OMCVD processes. Time dependent terms in the balance equations are neglected, since the growth rates are several orders of magnitude smaller than the gas velocities. The momentum and energy equations can be solved independently from the species balance equations, since reactants are typically dilute in the OMCVD technique with a carrier gas (usually H_2) in large excess. The assumption of dilute reactants leads to a significant reduction in the scale of the numerical problem by removing the dependence of the fluid flow on the species balance which includes the reaction term. Therefore, it is sufficient to deal only with the carrier gas to describe the temperature and velocity profiles in an OMCVD reactor. The reactor geometry used in this study allowed further simplification of the problem to an axisymmetric analysis (*i.e.*, 2-D in r and z). This assumption has shown to be a good one in modelling the vertical reactors except under conditions where strong natural convection exists[132]. The flow is laminar, since low flow rates are typically used in OMCVD technique. The Reynolds number in this study was less than 250 for N_2 and less than 70 for H_2 . The carrier gas is assumed to be a perfect gas but

with no effect of pressure on density, since the flow velocity is much less than the speed of sound (*i.e.*, the Mach number $\ll 1$).

With the above-mentioned assumptions, the momentum balance equations take the following form in cylindrical coordinates[160]:

r - momentum equation:

$$\frac{1}{r} \left[\frac{\partial}{\partial r}(r\rho v_r^2) + \frac{\partial}{\partial z}(r\rho v_z v_r) \right] = -\frac{\partial P}{\partial r} + \frac{1}{r} \left[\frac{\partial}{\partial r}(r\mu \frac{\partial v_r}{\partial r}) + \frac{\partial}{\partial z}(r\mu \frac{\partial v_r}{\partial z}) \right] - \frac{2\mu v_r}{r^2} \quad (4-9)$$

z - momentum equation:

$$\frac{1}{r} \left[\frac{\partial}{\partial r}(r\rho v_r v_z) + \frac{\partial}{\partial z}(r\rho v_z^2) \right] = -\frac{\partial P}{\partial z} + \frac{1}{r} \left[\frac{\partial}{\partial r}(r\mu \frac{\partial v_z}{\partial r}) + \frac{\partial}{\partial z}(r\mu \frac{\partial v_z}{\partial z}) \right] - \rho g \quad (4-10)$$

where v_r is the radial velocity; v_z is the axial velocity; P is the pressure; ρ is the density of the carrier gas; μ is the viscosity of the carrier gas; r and z are the radial and the axial coordinate, respectively; g is the acceleration of gravity.

The continuity equation becomes:

$$\frac{\partial}{\partial r}(r\rho v_r) + \frac{\partial}{\partial z}(r\rho v_z) = 0 \quad (4-11)$$

The ideal gas law is used to compute the density as a function of temperature:

$$\rho = \frac{PM}{RT} \quad (4-12)$$

where M is the molecular weight of the carrier gas; R is the gas constant; and T is the absolute temperature. The pressure used in equation (4-12) is assumed to be constant at 1 atm. The pressure drop will only affect the flow (*i.e.*, velocity).

The energy equation takes the following form:

$$\frac{1}{r} \left[\frac{\partial}{\partial r} (r \rho v_r T) + \frac{\partial}{\partial z} (r \rho v_z T) \right] = \frac{1}{r} \left[\frac{\partial}{\partial r} \left(\frac{rk}{c_p} \frac{\partial T}{\partial r} \right) + \frac{\partial}{\partial z} \left(\frac{rk}{c_p} \frac{\partial T}{\partial z} \right) \right] \quad (4-13)$$

where c_p is the heat capacity per unit mass of the carrier gas, and k is the thermal conductivity of the carrier gas. The terms involving viscous heating, heat of chemical reactions, and Dufour (thermodiffusion) flux are omitted in the formulation of the energy equation, since they are negligible for typical OMCVD conditions[131,160,161].

The temperature dependence of the transport properties is assumed to follow a power law[134]:

$$\mu = \mu_o (T/T_o)^{0.648} \quad (4-14)$$

$$k = k_o (T/T_o)^{0.691} \quad (4-15)$$

where the reference values are the experimentally determined values for N_2 and H_2 [162]. For H_2 , $\mu_o = 0.876 \times 10^{-4} \text{ g cm}^{-1} \text{ s}^{-1}$ at $T_o = 293.85 \text{ K}$, and $k_o = 4.4632 \times 10^{-4} \text{ cal s}^{-1} \text{ cm}^{-1} \text{ K}^{-1}$ at $T_o = 299.85 \text{ K}$; for N_2 , $\mu_o = 1.781 \times 10^{-4} \text{ g cm}^{-1} \text{ s}^{-1}$ at $T_o = 300.55 \text{ K}$, and $k_o = 0.624 \times 10^{-4} \text{ cal s}^{-1} \text{ cm}^{-1} \text{ K}^{-1}$ at $T_o = 299.85 \text{ K}$. The c_p is assumed to be constant, since it is only a weak function of temperature in the temperature range of this study. For H_2 , $c_p = 3.4 \text{ cal g}^{-1} \text{ K}^{-1}$; for N_2 , $c_p = 0.243 \text{ cal g}^{-1} \text{ K}^{-1}$ [162].

Figure 4-8 gives a schematic representation of the reactor model with thermal boundary conditions as follows:

On the walls and the susceptor surface, the normal and tangential velocities are zero:

$$v_r = 0, v_z = 0 \quad (4-16)$$

At the inlets, the fluid has only an axial velocity:

$$v_r = 0, v_z = v_o \quad (4-17)$$

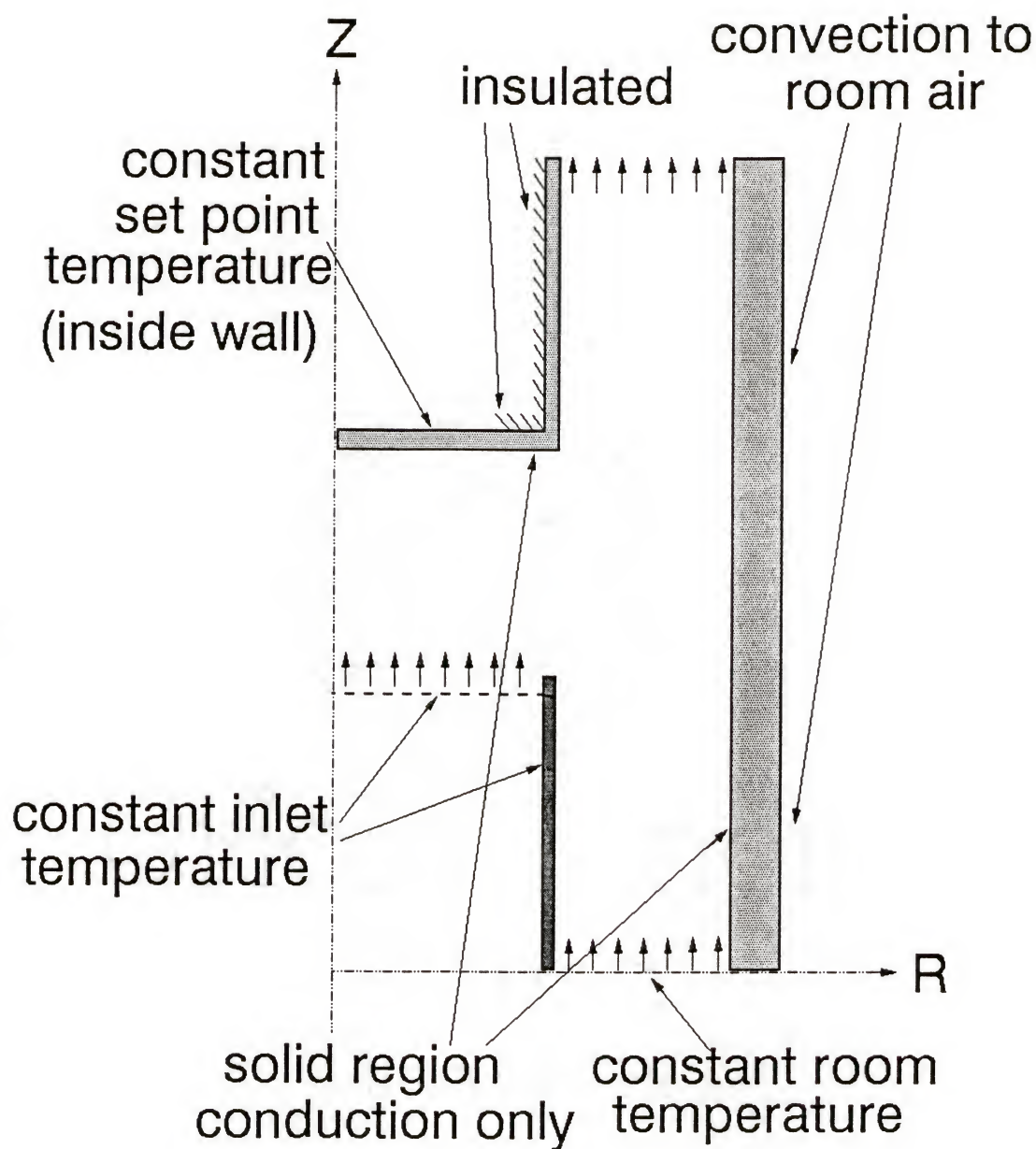


Figure 4-8: Schematic of the reactor model with thermal boundary conditions.

where v_o is given by:

$$v_o = Q/A \quad (4-18)$$

Q is the volumetric flow rate of center or sweeping flow, and A is the cross-sectional area of center or sweeping flow inlet.

Since the reactor is assumed to be axisymmetric, the centerline conditions are:

$$v_r = 0, \frac{\partial v_z}{\partial r} = 0, \frac{\partial v_r}{\partial r} = 0, \frac{\partial T}{\partial r} = 0 \quad (4-19)$$

At the outlet, the velocity and temperature fields are assumed to be fully developed:

$$\frac{\partial v_r}{\partial z} = 0, \frac{\partial v_z}{\partial z} = 0, \frac{\partial T}{\partial z} = 0 \quad (4-20)$$

The temperature at the inlets are assumed to be constant:

$$T = T_o \quad (4-21)$$

where T_o is equal to a constant temperature at the center flow inlet and at the wall of stainless steel center tube which could be different from room temperature because of radiation heating, and T_o is equal to the room temperature at the sweeping flow inlet.

The temperature boundary conditions for the furnace are specified at the inside wall of the furnace. The bottom of the inside wall which is in contact with the heating block (1.08" in diameter) is at constant set point temperature, and the rest of the inside wall is assumed to be insulated, since the inside of the furnace is under vacuum:

$$T = T_{set} \quad \text{from } r = 0 \text{ to } r = 1.37 \text{ cm at the bottom of the inside wall} \quad (4-22a)$$

$$\frac{\partial T}{\partial r} = 0 \text{ at the rest of the inside wall} \quad (4-22b)$$

The furnace wall and the reactor wall were included in the computational domain. It was assumed that conduction is the only way for heat to transfer in those areas. The heat conduction is described by the equation:

$$\frac{1}{r} \frac{\partial}{\partial r} (rk_w \frac{\partial T}{\partial r}) + \frac{\partial}{\partial z} (k_w \frac{\partial T}{\partial z}) = 0 \quad (4-23)$$

where k_w is the thermal conductivity of the quartz.

The outside of the reactor is blanketed with a room temperature air, and heat is transferred to the surrounding air by Newton's law:

$$-k_w \left(\frac{\partial T}{\partial n} \right) = h(T_w - T_{\text{room}}) \quad (4-24)$$

where T_w is the wall temperature, T_{room} is the ambient temperature, and $h = 1.226 \times 10^{-4} \text{ cal} \cdot \text{s}^{-1} \cdot \text{cm}^2 \cdot \text{K}^{-1}$ is an overall heat transfer coefficient[163].

A computational fluid dynamics software, PHOENICS, was used to carry out the numerical simulations of the OMCVD reactor. PHOENICS employs the SIMPLE (Semi-Implicit Method of Pressure Linked Equations) algorithm to solve the governing equations listed above. First, the velocity components were solved from the momentum equations based on a guessed pressure distribution (uniform field in our calculations). Since the guessed pressure field in general is not the same as the real one, the obtained velocity will not satisfy the continuity equation. The residue, which came from substituting the nonconverged velocity values into the continuity equation, then was used to correct the pressure field. This velocity-pressure correction process was repeated many times until a velocity value satisfying both momentum and continuity equations was obtained. Because the pressure variation in the reactor is much less than the pressure itself, it was assumed that density was a function of temperature only and could be determined from the state equation of a perfect gas. The energy

equation was solved for temperature whenever a velocity value was obtained. This temperature value then was used to determine the density as well as the viscosity and conductivity which are also a function of temperature and appear in the momentum and energy equations. A very deep under-relaxation had to be used in order to get a converged solution. This also caused a large number of velocity-pressure corrections, around 1500, in most of our calculations.

4.4 Results and Discussion

4.4.1 Temperature Distribution in the Reactor

The axial temperature profile in the reactor was measured for N₂ and H₂ carrier gas as a function of the inlet gas flow velocity and the aspect ratio. Figure 4-9 shows the axial temperature profiles of the reactor for N₂ carrier gas and H₂ carrier gas at the same operating conditions (*i.e.*, inlet gas velocities of 3.0 cm/s of both the center and the sweeping flow, aspect ratio (AR) of 1, set point temperature of the furnace of 650 °C). It is clearly shown in the figure that the use of a N₂ carrier gas produces a steeper temperature gradient normal to the susceptor surface than the use of a H₂ carrier gas. This result agrees with the results obtained by other investigators[137,138] in their study of horizontal[137] and vertical downflow[138] reactors. The unwanted gas phase reactions can be suppressed by making the temperature gradient near the susceptor steeper, thus keeping the reacting species cold during their transport to the growth surface. The result is easily understood by considering the about 8 times higher thermal conductivity of H₂ ($k = 4.4632 \times 10^{-4} \text{ cal s}^{-1} \text{ cm}^{-1} \text{ K}^{-1}$) compared with that of N₂ ($k = 0.624 \times 10^{-4} \text{ cal s}^{-1} \text{ cm}^{-1} \text{ K}^{-1}$). Heating of the gas is more efficient in H₂ than in N₂. The N₂ temperature remains low in a larger volume below the susceptor even for the low gas flow velocities used in this study.

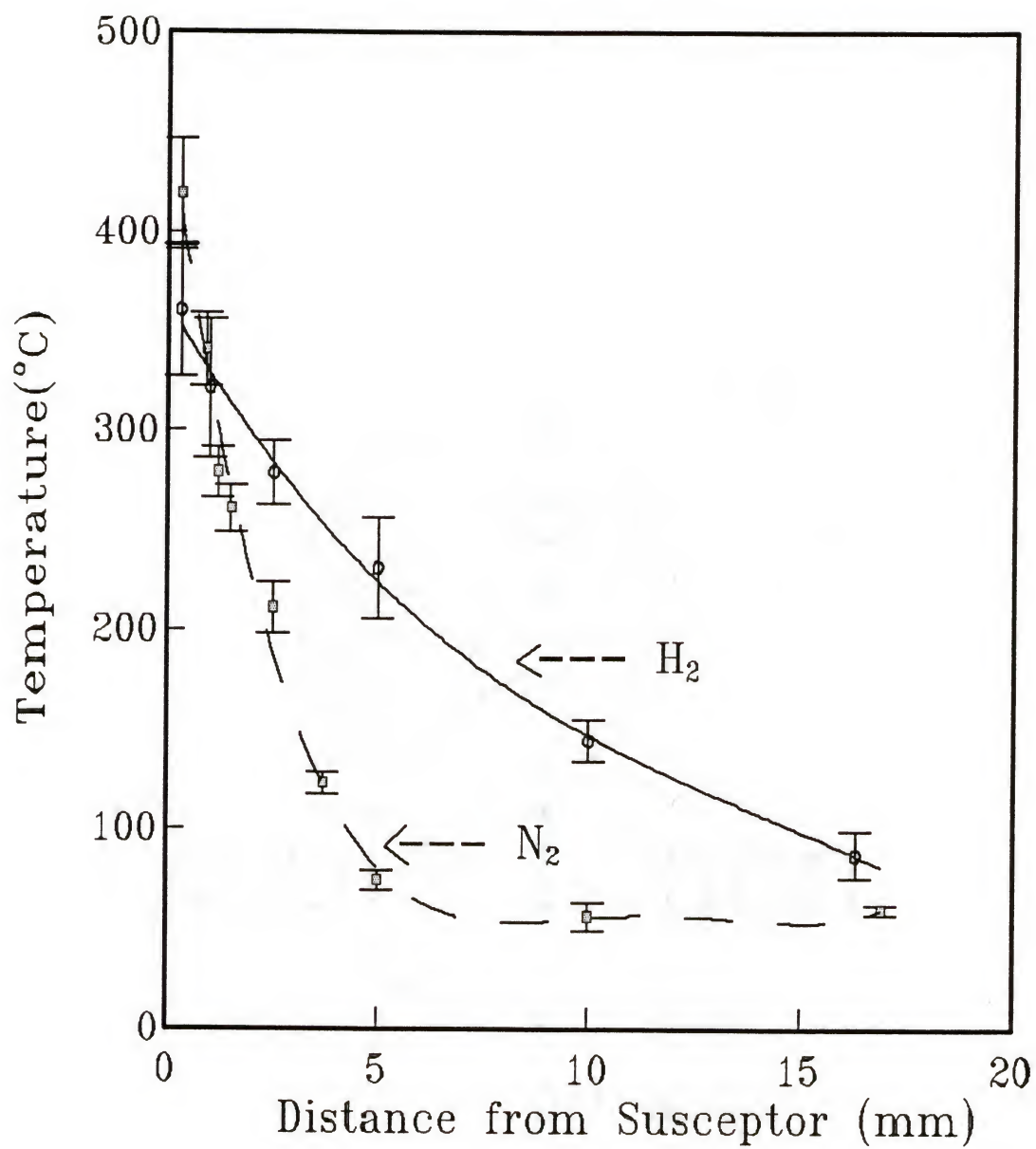


Figure 4-9: Axial temperature profiles of the reactor for nitrogen and hydrogen:
 $AR = 1$; $v = 3.0$ cm/s (center and sweeping); $T_{set} = 650$ $^{\circ}C$.

The extrapolated temperature at the susceptor surface was considerably lower than the set point temperature which is measured at the inside bottom wall of the furnace, indicating that there may exist a significant thermal contact resistance between the heating block and the furnace wall. Rough surfaces of the heating block and the furnace wall can introduce a large thermal contact resistance. A similar phenomenon has been observed by Koppitz *et al.*[137]. In their study of a horizontal reactor, they observed an approximately 200 °C temperature drop near the susceptor (graphite) surface from the susceptor set point temperature. Their susceptor was also heated by a resistance heating, and the thermocouple was located on the back of the susceptor, which is similar to this study. Other researchers[138,139], however, did not observe this phenomena. This emphasizes the importance of the furnace design in monitoring the surface temperature, since the large deviation in the measured surface temperature can cause a large error in the data obtained from kinetic experiments. An attempt has been made to measure the surface temperature of the outside wall of the furnace by a thermocouple which was bonded onto the susceptor surface by a ceramic epoxy. The measured temperature provided a lower value because of the significant temperature drop caused by a contact resistance. The thermocouple revealed a surface temperature even lower than the extrapolated surface temperature. The in-situ temperature measurement by Raman spectroscopy seems to be a very accurate technique in this sense.

The temperature near the center tube inlet was higher than the room temperature, and this was conceivably caused by the radiation heating of the stainless steel center tube from the hot susceptor. Error bars are also shown in Figure 4-9, and it is seen that the measurement of temperature is more accurate in the case of N₂ carrier gas than in the case of H₂ carrier gas due to the more rotational bands being available for N₂.

The effect of changing the aspect ratio on the centerline temperature profile was investigated and is shown in Figure 4-10. A larger aspect ratio produced a larger temperature gradient, and this is presumably due to the decrease in the radiation heating of the center tube

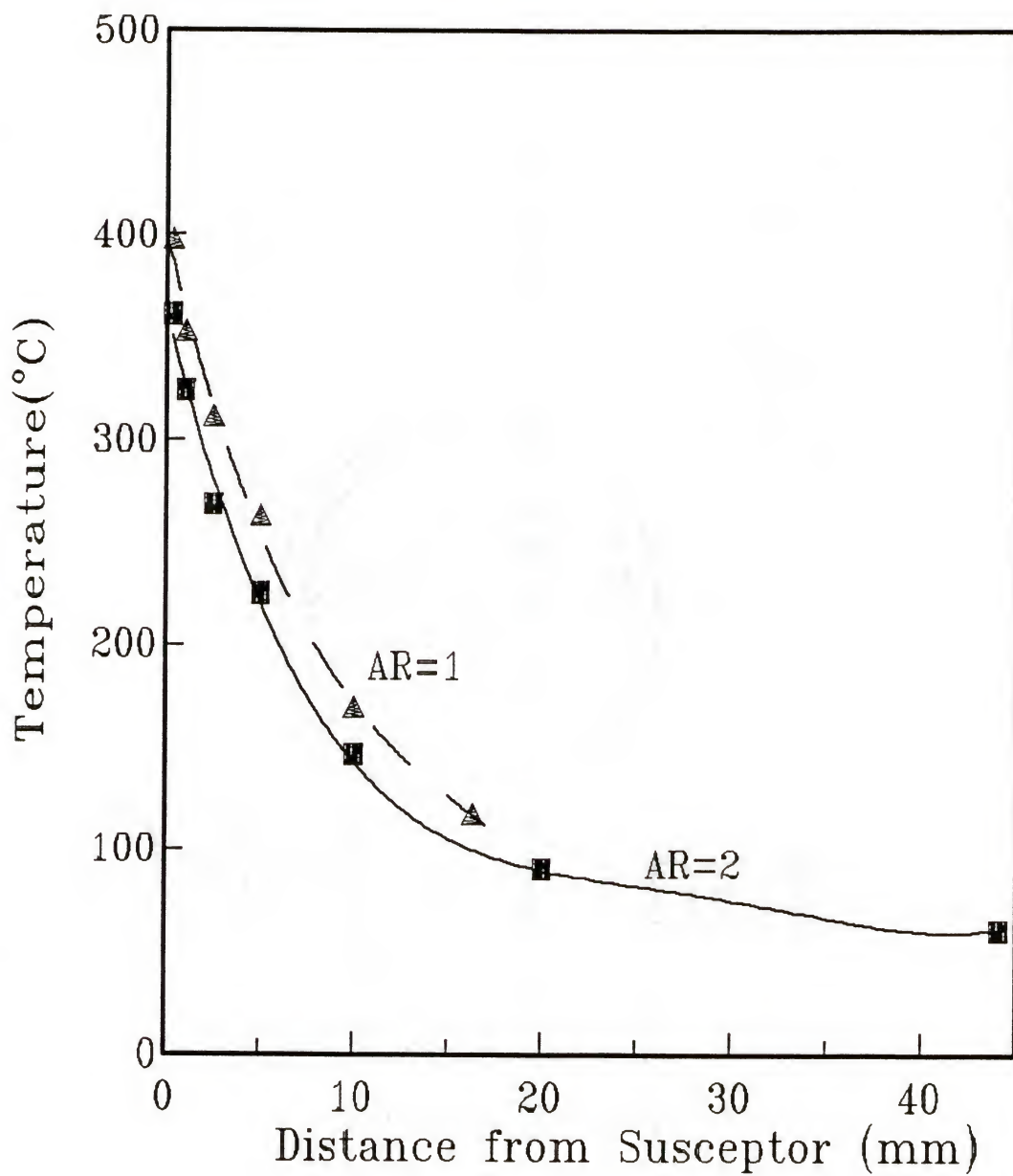


Figure 4-10: The effect of varying the aspect ratio (AR) on the axial temperature profile in the reactor for hydrogen carrier gas; $v = 1.5$ cm/s (center and sweeping); $T_{\text{set}} = 650$ °C.

from the hot susceptor. The decrease in the temperature near the center tube inlet was observed with increasing aspect ratio. The difference in the temperature profile caused by varying the aspect ratio, however, was not very large for the operating conditions used in this study.

The experimentally measured temperature profiles are compared with the calculation, and the results are shown in Figure 4-11 and Figure 4-12. The effect of changing the inlet gas velocity on the axial temperature profile in the reactor was investigated for nitrogen carrier gas (Figure 4-11) and for hydrogen carrier gas (Figure 4-12). As expected, increasing the inlet velocity made the temperature gradient steeper, simply because the gas spends less time in the reactor for heating with increased velocity. Cooling of the center tube is also enhanced with higher gas velocity, lowering the gas inlet temperature. For inlet flow velocities greater than 3.0 cm/s (both the center and the sweeping flow), at given susceptor temperature (650 °C), the axial temperature profile seems to reach a saturation region for N₂ carrier gas. Further increase in the inlet velocity did not change the axial temperature profile significantly. The high temperature zone (> 200 °C) was restricted within 2.5 mm from the susceptor surface in this case. This narrow high temperature zone near the susceptor was visually observed as a thin cloud of decomposed particles when TMI was introduced into the center flow. In the case of the H₂ carrier gas, however, no such sign of saturation was observed in the velocity range studied (0.09 to 4.5 cm/s), although the axial temperature profile became steeper with increasing inlet flow velocity. The high temperature zone (> 200 °C) was approximately within 5 mm from the susceptor surface for H₂ carrier gas with inlet flow velocity of 4.5 cm/s.

The calculated results were in good agreement with the experimental results, especially for the case of the N₂ carrier gas, when the extrapolated temperatures from the experimental data were used for the temperature at the center tube inlet and for the temperature at the inside wall of the furnace. A large temperature drop (> 200 °C) near the

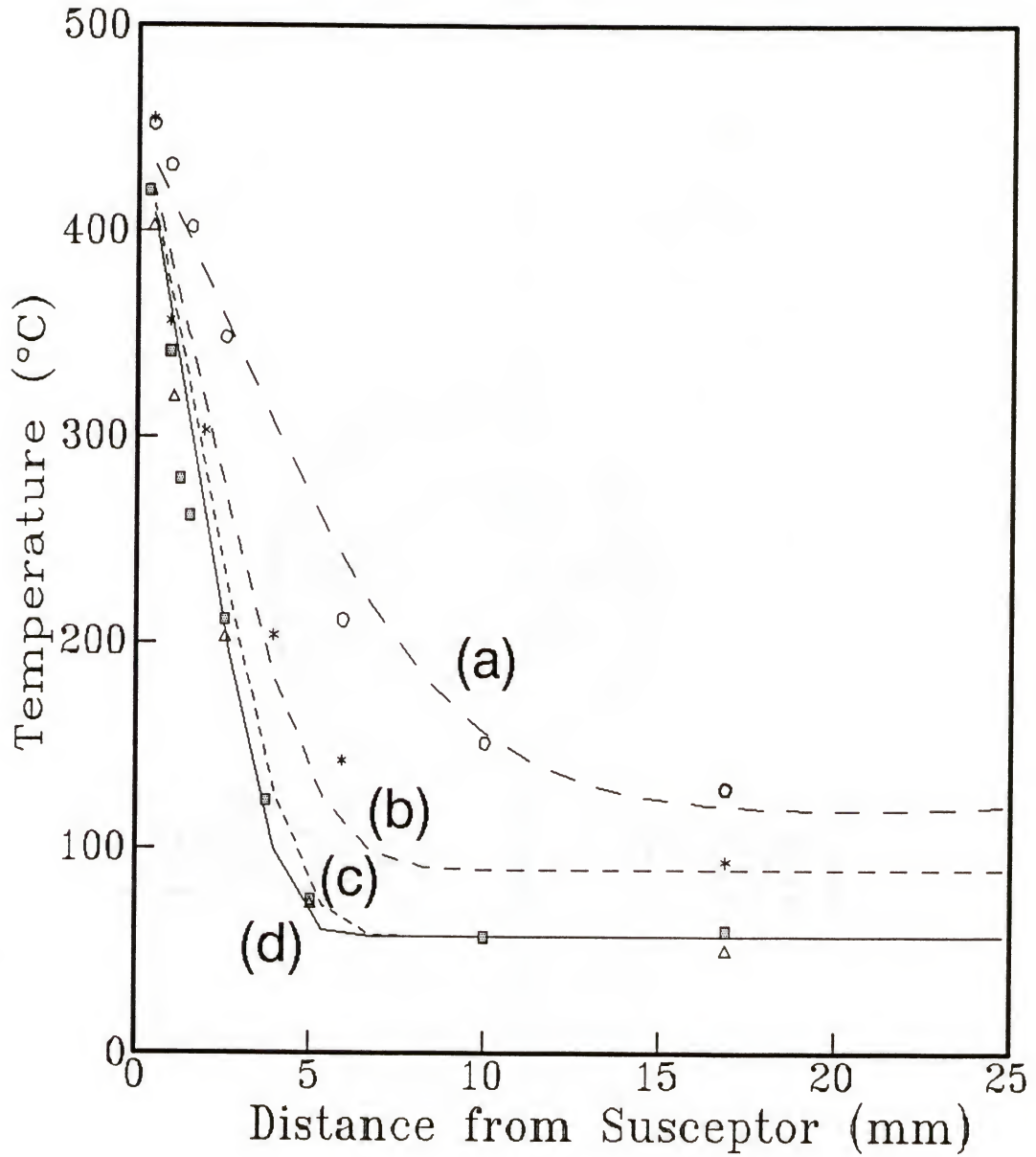


Figure 4-11: The effect of varying the gas inlet velocity on the axial temperature profile in the reactor for nitrogen carrier gas: calculated results (solid and dashed lines) are shown with the experimental data. Operating conditions: $AR = 1$; $T_{set} = 650\text{ }^{\circ}\text{C}$; $v =$ (a) 0.09 cm/s , (b) 1.5 cm/s , (c) 3.0 cm/s , (d) 4.5 cm/s .

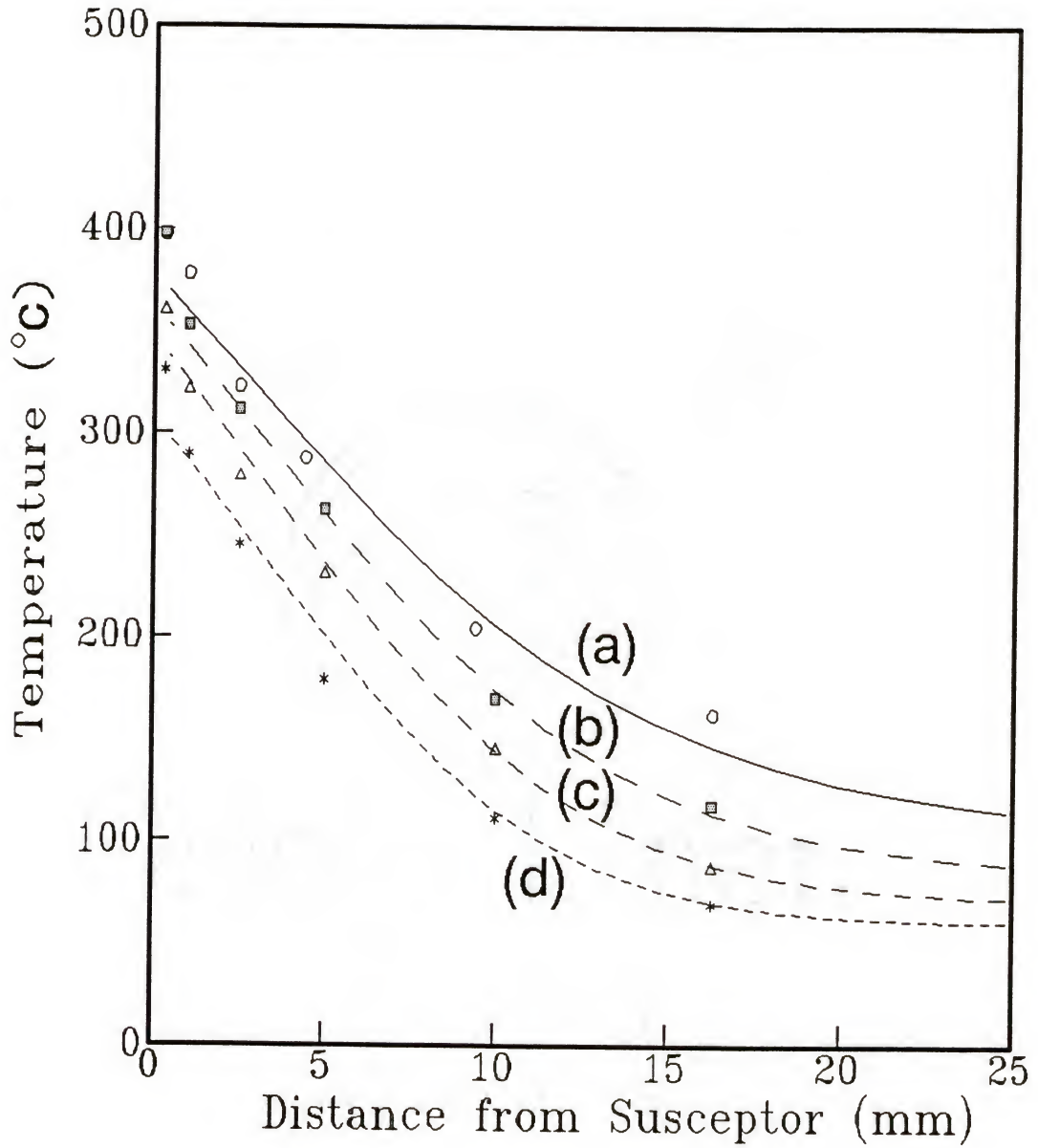


Figure 4-12: The effect of varying the gas inlet velocity on the axial temperature profile in the reactor for hydrogen carrier gas: calculated results (solid and dashed lines) are shown with the experimental data. Operating conditions: $AR = 1$; $T_{\text{set}} = 650\text{ }^{\circ}\text{C}$; $v =$ (a) 0.09 cm/s , (b) 1.5 cm/s , (c) 3.0 cm/s , (d) 4.5 cm/s .

susceptor surface (0.3 mm from the susceptor surface) from the furnace set point temperature was observed for the N_2 carrier gas, and it could not be explained by the temperature drop across the thin furnace wall and the gas, which indicates that the thermal contact resistance between the heating block and the inside wall of the furnace may cause this difference. By using the extrapolated temperature (460 °C) at the inside wall of the furnace from the experimental data, fairly good agreement between the calculation and the experiment was obtained for the N_2 carrier gas (Figure 4-11). In the case of the H_2 carrier gas, however, such a correction in the furnace temperature was not enough to accurately represent the experimental temperature profiles with varying gas inlet velocities. Further decrease in the susceptor temperature had to be assumed with increasing gas inlet velocity. The failure of the present reactor model in accurately describing the temperature profile seems to be caused by neglecting the radiation heat transfer in the system. Although the inside of the furnace was kept under vacuum which allowed an adiabatic thermal boundary condition at the inside wall of the furnace, the heat loss from the heating block to the surroundings still occurs via a radiation heat transfer. The transferred heat is then carried away by the carrier gas flowing outside the furnace, which in effect lowers the susceptor temperature. The apparent independence of the susceptor temperature with varying gas inlet velocity in the case of N_2 carrier gas is presumably due to the low thermal conductivity of N_2 . The interdependency of susceptor temperature with gas velocity, however, is clearly observed in the case of H_2 carrier gas (Figure 4-12). Similarly, the calculation with the assumption of room temperature at the gas inlets could not accurately represent the experimental data because of the radiation heating of the center inlet tube. The extrapolated temperature at the center flow inlet from the measurement was used to account for the temperature rise of the center tube. The temperature at the sweeping flow inlet was still assumed to be at room temperature, and it was found that this assumption is valid for the operating range of this study. The present model underestimates the temperature at the inside reactor wall since it does not account for the

radiation heating of the wall from the susceptor, but it was found that the centerline temperature profile is not sensitive to the reactor wall temperature once proper corrections are made for the temperature at the susceptor and at the center flow inlet.

The importance of an accurate heat transfer treatment in OMCVD reactor models has been recently emphasized by Fotiadis, *et al.*[132]. In the numerical study of a vertical downflow reactor, they have compared three different boundary conditions for the reactor wall: (a) constant room temperature (300 K), (b) adiabatic wall, and (c) a detailed thermal boundary conditions considering the radiation heat transfer from the susceptor, heat convection from the gas, heat conduction through the quartz wall, and heat transfer to the ambient by radiation and cooling. They found that the detailed wall boundary conditions produce the more uniformly distributed isotherms and correspondingly a forced convection dominated flow in the reactor. The constant room temperature boundary condition underestimated the wall temperature and generated a strong recirculation cell above the susceptor caused by a large temperature gradient developed near the susceptor. The adiabatic boundary condition overestimated the wall temperature and generated a natural convection cell next to the wall, since the hot wall caused the incoming gas to expand. The present model uses the detailed wall boundary conditions except for the radiation heat transfer terms, thus it is expected that the isotherms in the reactor be uniform and the flow be force-convection dominant. Ignoring the radiation heat transfer, however, underestimates the wall temperature, producing a larger temperature gradient near the susceptor. The relative importance of the radiation heat transfer to the reactor wall compared to the other modes of heat transfer has not been studied, but it does not seem to be important in this study due to the relatively low susceptor temperature involved (460 °C). The radiation heat transfer to the center inlet tube, however, was very important as already discussed in the previous paragraph.

Figure 4-13 and Figure 4-14 show the calculated isotherms and the flow profiles in the reactor for H₂ and N₂ carrier gas, respectively, as a function of the inlet flow velocities.

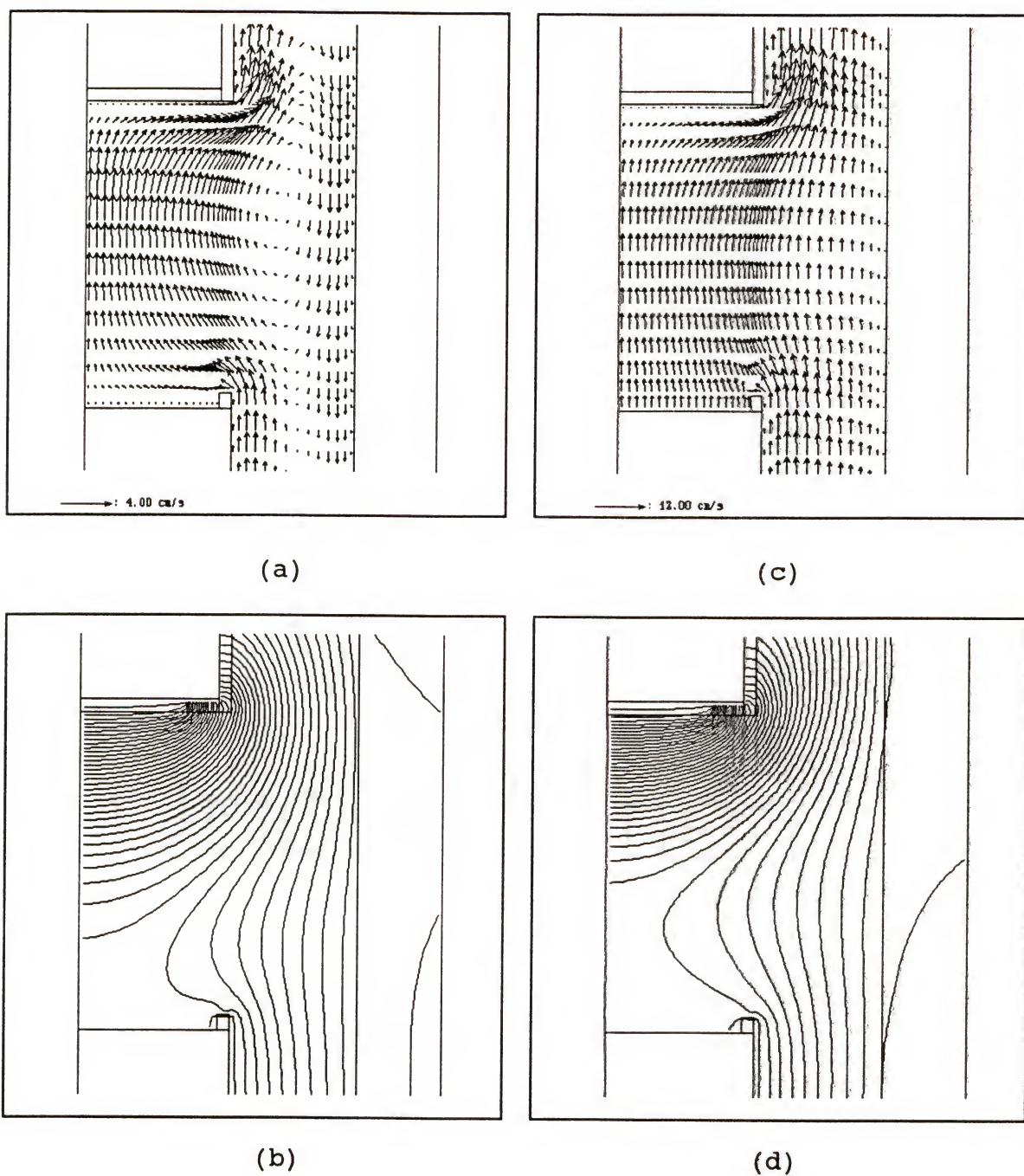


Figure 4-13: Calculated flow profiles and isotherms in the reactor for H_2 carrier gas as a function of inlet flow velocity: (a) flow profile, (b) isotherm for $v = 0.09 \text{ cm/s}$ (center and sweeping); (c) flow profile, (d) isotherm for $v = 3.0 \text{ cm/s}$ (center and sweeping). $T_{\text{set}} = 460 \text{ }^\circ\text{C}$; $T_{\text{in}} = 150 \text{ }^\circ\text{C}$.

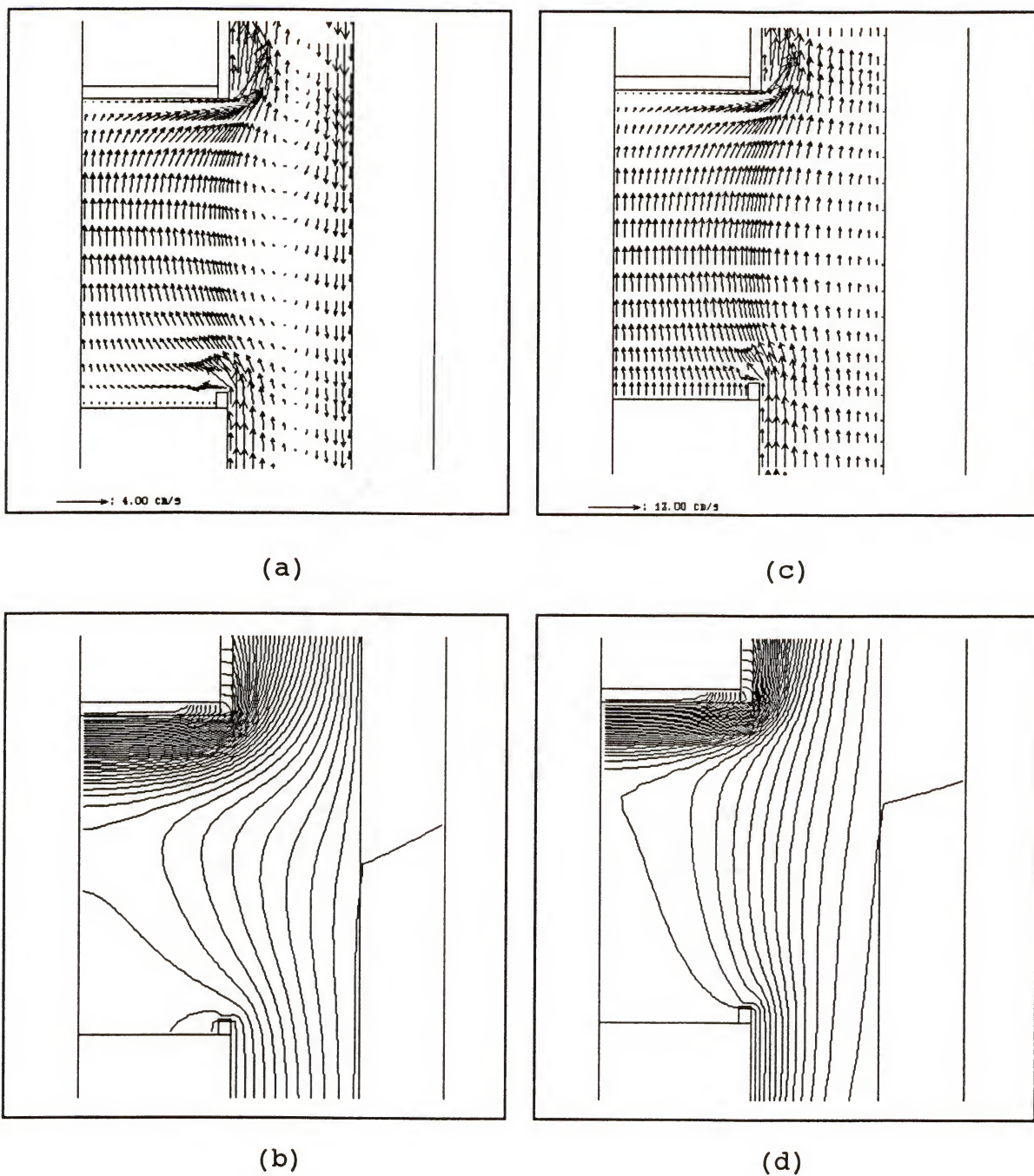


Figure 4-14: Calculated flow profiles and isotherms in the reactor for N_2 carrier gas as a function of inlet flow velocity: (a) flow profile, (b) isotherm for $v = 0.09 \text{ cm/s}$ (center and sweeping); (c) flow profile, (d) isotherm for $v = 3.0 \text{ cm/s}$ (center and sweeping). $T_{\text{set}} = 460 \text{ }^\circ\text{C}$; $T_{\text{in}} = 150 \text{ }^\circ\text{C}$.

The temperature difference between the adjacent lines in the figure of the isotherms is 10 °C, and the magnitude of the velocity is represented by the length of arrow in the figure of velocity profile with reference to the length of arrow in the bottom of the figures. The inlet flow velocities were the same for both the center flow and the sweeping flow. The susceptor temperature was 460 °C, the temperature at the center flow inlet was 150 °C, and the aspect ratio was fixed at one, which are the typical values obtained in the experiment. The other boundary conditions were the same as explained in section 4.3. At the very low inlet flow velocity (0.09 cm/s), for both H₂ (Figure 4-13b) and N₂ (Figure 4-14b), the isotherms spread out toward the gas inlet, indicating a small temperature gradient normal the susceptor surface. A recirculating flow pattern develops at this velocity, due to the acceleration of the gas flow in the center region caused by the heating of the gas, in order to satisfy the mass-conservation. A slightly stronger recirculation was observed in the H₂ carrier gas (Figure 4-13a) compared to that in the N₂ carrier gas (Figure 4-14a), because heating of gas is more efficient in H₂ than in N₂. As the inlet flow velocity increases (3.0 cm/s), the isotherms contract toward the susceptor (Figure 4-13d and Figure 4-14d), indicating a larger temperature gradient normal to the susceptor surface, and the recirculating flow patterns disappear (Figure 4-13c and Figure 4-14c). The isotherms confined to the vicinity of the susceptor and parallel to the susceptor were obtained at the higher velocity with the use of a N₂ carrier gas (Figure 4-14d), and the flow was dominated by forced convection in this case (Figure 4-14c). The isotherms developed in the reactor with the use of H₂ carrier gas, however, was not confined to the vicinity of the susceptor even at higher velocity (3.0 cm/s) because of the high thermal conductivity of H₂. The recirculating flow patterns were not strong in the entire operating range of this study except for the case with very small gas velocity (0.09 cm/s), for both H₂ and N₂ carrier gas. The calculation with this specific operating conditions found that the flow recirculations completely disappear when the flow velocity exceeds 1.4 cm/s and 1.6 cm/s for N₂ carrier gas and for H₂ carrier gas, respectively.

The relatively weak flow recirculations seem to be caused by the reactor geometry used in this study. A stabilizing density gradient is expected with this inverted reactor configuration.

Several factors can cause the gas dynamics in the reactor to deviate from the calculated results. For example, the axisymmetry cannot be hold strictly, if the center inlet tube is placed slightly off-axis, or the temperature variation exists across the susceptor surface. Sharp corners and sudden expansions (or contractions) in the flow cross-sectional area may produce the laminar vortices caused by flow instability. The two-dimensional analysis performed in this study, however, provides many useful informations regarding the gas dynamics in the reactor, and it sucessfully represents the experimentally measured axial temperature profile with proper boundary conditions. Therefore, it is used as a guiding tool in performing and interpreting the experiment.

The use of a N_2 carrier gas with high velocity seems to be desirable for the growth of epitaxial layers by the OMCVD technique from the viewpoint of the gas dynamics. Indeed, the work of Sacilotti *et al.*[164] showed that in the deposition of InP from TEI and PH_3 in a horizontal reactor, more uniform epitaxial layers were deposited with the use of a N_2 carrier gas compared to the use of a H_2 carrier gas. Even better reactor performance can be expected with the vertical upflow reactor configuration. Other problems such as the purity of the N_2 carrier gas and the unintentional doping (carbon) of the epitaxial film, however, must be addressed prior to realizing the advantages of using the N_2 as a carrier gas.

4.4.2 Tracer Study: Behavior of Reactants in the Reactor

The behavior of reactants in the reactor was studied by using a tracer species, CH_4 (5% in the carrier gas), which was introduced into the center flow (reactant mixtures flow through the center tube in actual growth). The effect of sweeping flow on the CH_4 dispersion in the reactor was investigated as a function of the velocity matching between the center and

sweeping flow. Both flows were developed for 5 min to reach the steady state conditions, and the reactor was scanned laterally and vertically to trace the CH_4 molecules flowing in the reactor. Other experimental details were previously discussed in section 4.2.3. The center inlet tube was packed with 1/8" diameter glass beads for this study to insure complete mixing of CH_4 with the carrier gas. It was found that the mixing of CH_4 with the carrier gas was not complete without the packing, especially in the case of N_2 carrier gas. This will be discussed in detail in the next section. After packing the center tube, the complete mixing was obtained in the center tube, which was verified by comparing the CH_4 concentration profile near the center tube inlet with that near the susceptor surface in the absence of the sweeping flow. The flat concentration profiles were obtained at both locations with the value of 4.6% in N_2 for the target concentration of 5%.

Figure 4-15 shows the relative CH_4 concentration profiles in the N_2 carrier gas along the y-axis for matched inlet flow velocities (*i.e.*, center flow velocity (v_c) = 2.4 cm/s and sweeping flow velocity (v_s) = 2.4 cm/s) at room temperature. The y position at 0 stands for the centerline of the reactor, and $y = 38.1$ mm is at the reactor wall. The dashed lines in the middle of the figure represent the y positions of the inside edge and the outside edge of the center tube, respectively. The concentration profiles were obtained at four different vertical positions ($z = 4, 11, 18, 27$ mm from the center flow inlet). The aspect ratio was fixed at 0.9, thus $z = 27$ mm stands for the position at 4 mm from the susceptor surface. It was found that the center flow initially contracts toward the center until it finally expands near the susceptor. The dispersion of CH_4 was not significant in the N_2 carrier gas at the operating conditions used, as shown in the Figure 4-15 by the relative independence of the concentration at $y = 0$ for different vertical positions. The center flow was well confined in the center region at these matched velocities. When the sweeping flow velocity was reduced to 0.6 cm/s by keeping the center flow velocity at 2.4 cm/s (Figure 4-16), CH_4 was detected in the sweeping flow region, and the concentration got higher near the susceptor. The center flow

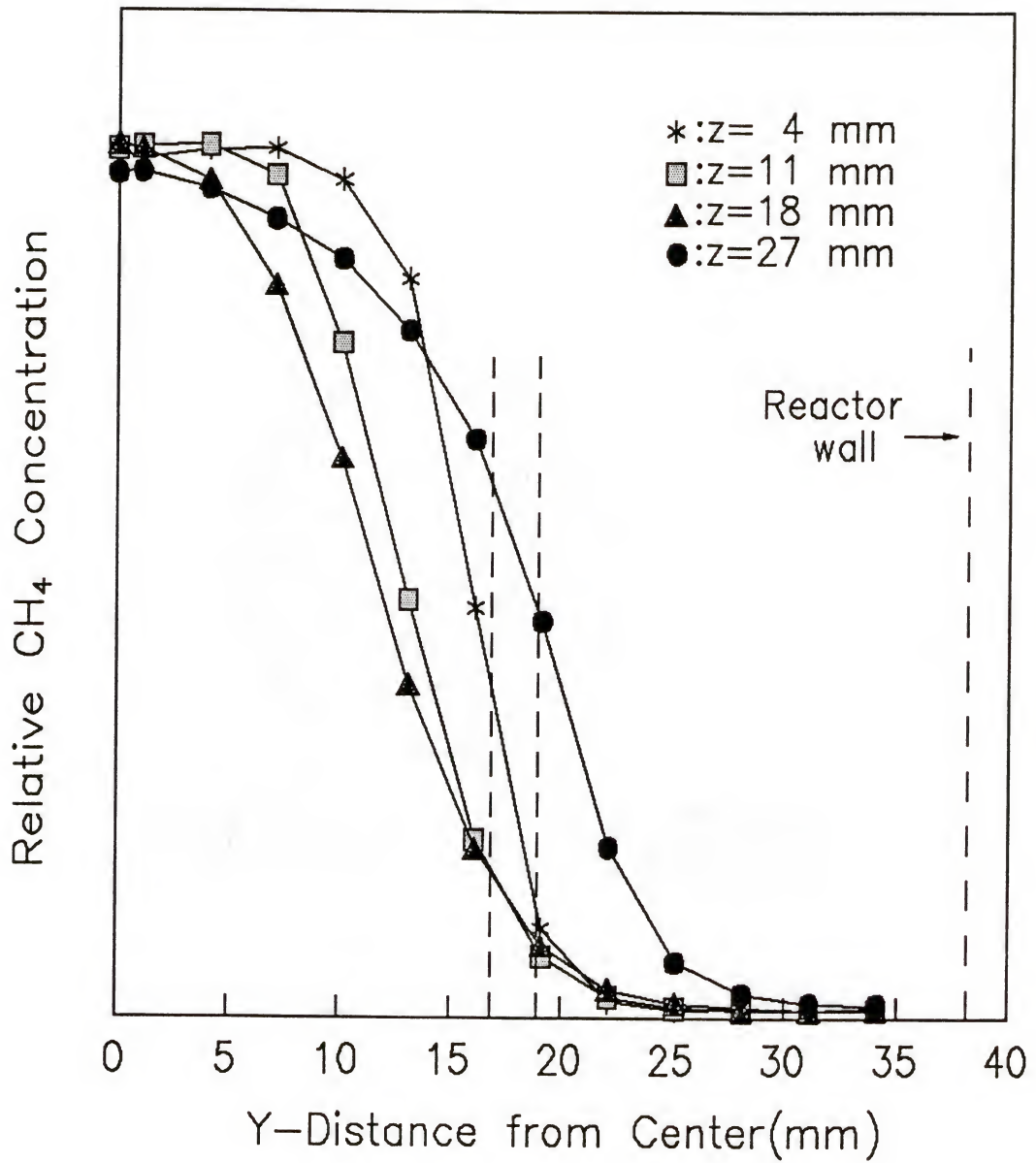


Figure 4-15: The relative CH₄ concentration profiles along the y-axis:
 matched inlet flow velocities; N₂ carrier gas; T_{set} = 25 °C;
 AR = 0.9; $v_c = 2.4$ cm/s; $v_s = 2.4$ cm/s.

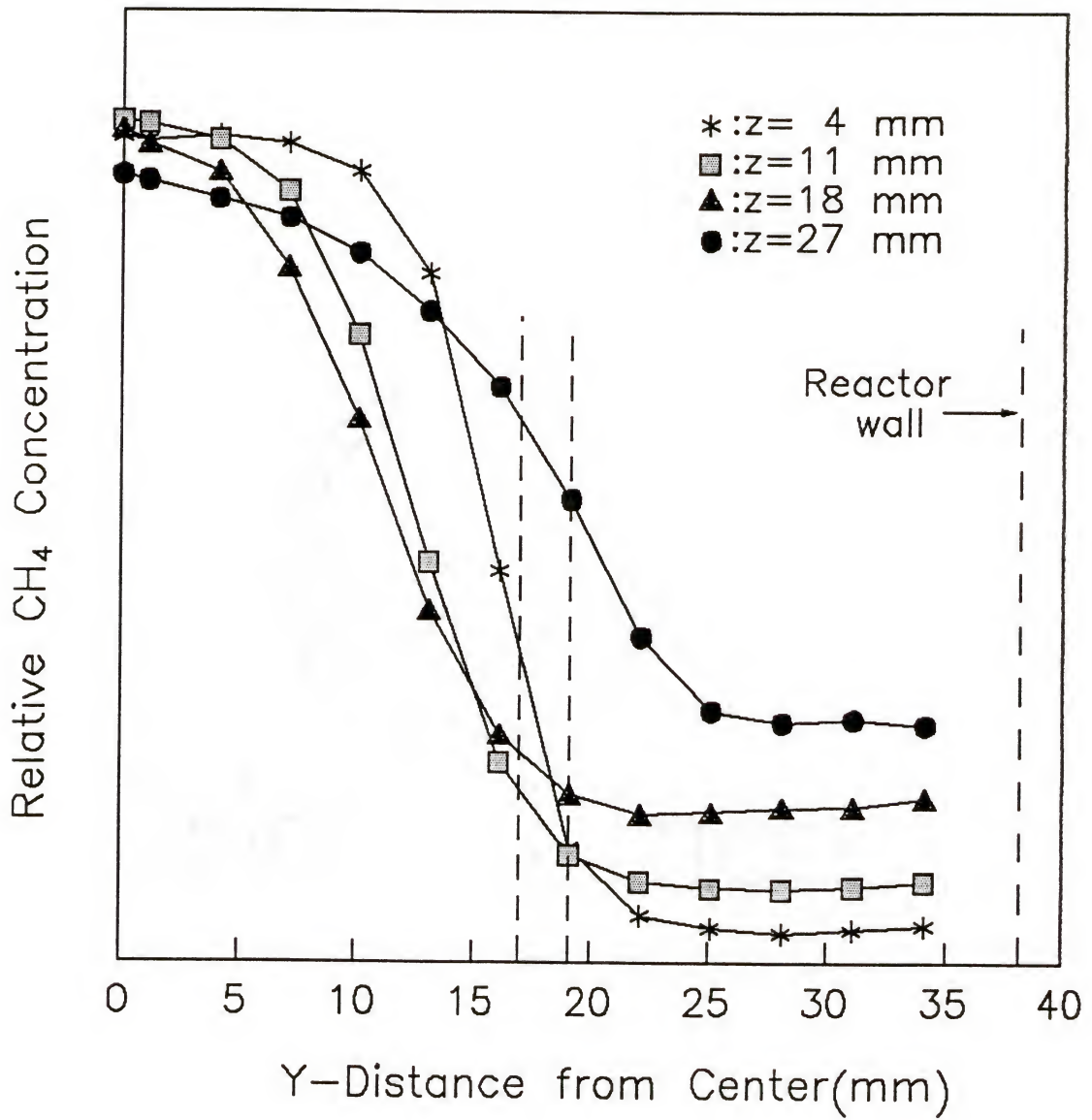


Figure 4-16: The relative CH₄ concentration profiles along the y-axis:
 unmatched inlet flow velocities; N₂ carrier gas; T_{set} = 25 °C;
 AR = 0.9; v_c = 2.4 cm/s; v_s = 0.6 cm/s.

region, however, was not affected. It is conceived that a laminar vortex develops in the sweeping flow region by the flow unmatching, which in effect, recirculates the CH_4 containing flow. The calculations of the reactor model are shown in Figure 4-17 and Figure 4-18 for matched and unmatched inlet velocities, respectively. The model does not predict any of the abnormal behavior observed in the experiment. In the case of matched inlet flow velocities, the center flow and the sweeping flow nicely join at the inlet tube edge and at the flow interface, and the center flow is well confined in the center region. It does not show the contracting flow at the inlet, either. In the case of unmatched inlet flow velocities, the model predicts the expanding center flow without any laminar vortices. It seems that the sharp corners present in the reactor and the flow unmatching may cause the flow instability which is not predicted by the simple 2-dimensional model.

Increasing the susceptor temperature to $T_{\text{set}} = 650\text{ }^{\circ}\text{C}$ did not introduce any new flow behavior other than those already observed in the room temperature experiments with the center flow velocity of 2.4 cm/s. Indeed, the concentration profiles obtained with elevated susceptor temperature almost identically reproduced the concentration profiles obtained at room temperature except for the sign of slightly increased diffusion of CH_4 , which was indicated by the small decrease in the concentration at $y = 0$ near the susceptor ($z = 27\text{ mm}$) and longer tail toward the reactor wall. The center flow was very well confined in the center region with matched inlet flow velocities. This is encouraging because one can expect that in the actual epitaxial growth runs or in the kinetic experiments, the reacting species are confined in the center flow region, thus the wall deposition can be completely removed. The heavier mass (smaller diffusivity) of actual reactants (TMI , PH_3) compared to that of CH_4 further favor the situation. Indeed, no depositions were observed at the reactor wall, when TMI was introduced into the center flow, although depositions were observed on the sides of the furnace.

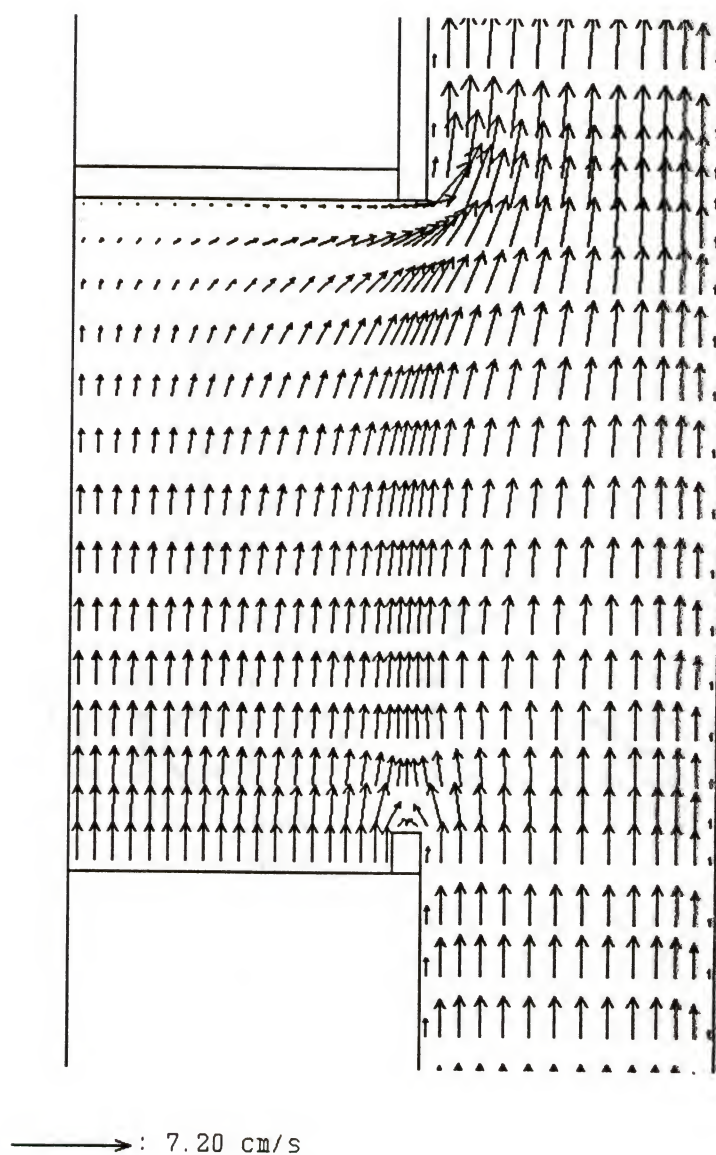


Figure 4-17: The calculated velocity profile in the reactor:
 matched inlet flow velocities; N_2 carrier gas; $T_{\text{set}} = 25^\circ\text{C}$;
 $\text{AR} = 0.9$; $v_c = 2.4 \text{ cm/s}$; $v_s = 2.4 \text{ cm/s}$.

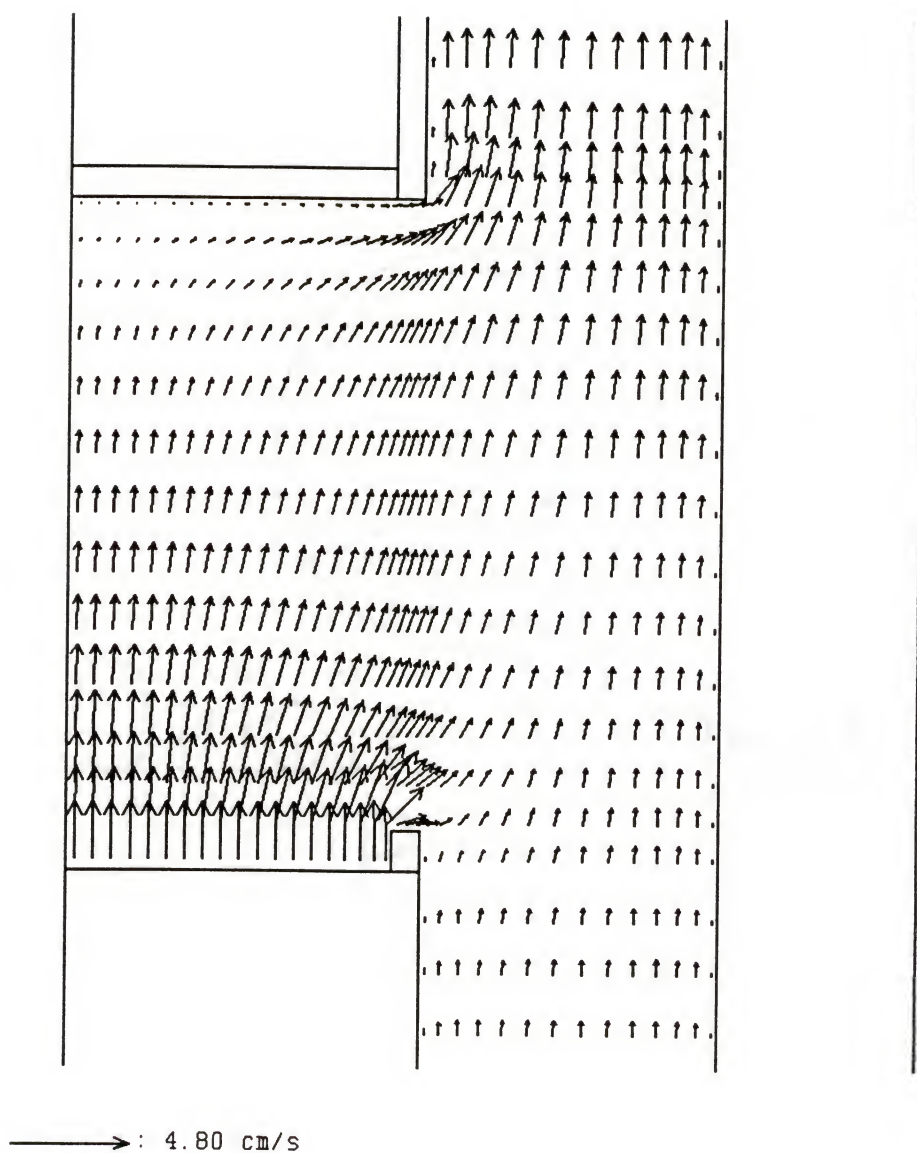


Figure 4-18: The calculated velocity profile in the reactor:
 unmatched inlet flow velocities; N_2 carrier gas; $T_{set} = 25\text{ }^{\circ}\text{C}$;
 $AR = 0.9$; $v_c = 2.4\text{ cm/s}$; $v_s = 0.6\text{ cm/s}$.

The effect of increasing the sweeping flow velocity with respect to the center flow velocity from the matched condition was studied with elevated susceptor temperature (650 °C) at very low center flow velocity (0.6 cm/s), and the results are shown in Figure 4-19. An invasion of sweeping flow into the center flow is expected in this case, and it seems that the invasion actually occurred in the reactor. The noticeable decrease in CH₄ concentration supports the argument. Figure 4-20 shows the calculated velocity profile for this case at room temperature, and the flow invasion is clearly seen in the figure. At elevated susceptor temperature with low center flow velocity, this effect should be exaggerated since the acceleration of the center flow occurs due to the gas heating (Figure 4-14a). Another characteristic feature in Figure 4-20 is the presence of a significant amount of CH₄ near the reactor wall, although the flows are matched. At this low velocity (0.6 cm/s), a buoyancy driven flow recirculation can be expected (Figure 4-14a), but the CH₄ diffusion may also play an important role. Again, the increased sweeping flow sweeps the reactor wall. It should be also mentioned that none of the above-mentioned phenomena were observed, when the center flow velocity was increased to 1.2 cm/s.

The relative concentration profiles of CH₄ in H₂ carrier gas along the y-axis were investigated for matched inlet flow velocities of 2.4 cm/s at room temperature. The effect of replacing N₂ with H₂ as a carrier gas on the CH₄ concentration profiles were studied and the results are shown in Figure 4-21. Completely different CH₄ concentration profiles were obtained compared to the previous results obtained with the N₂ carrier gas (Figure 4-15). CH₄ was evenly distributed at the center flow inlet, showing no sign of abnormal flow contraction observed with the N₂ carrier gas. A flat concentration profile up to the inside edge of the center inlet tube was obtained at $z = 4$ mm from the center flow inlet. When the center flow reaches near the susceptor surface, CH₄ is almost completely dispersed, and the elevated susceptor temperature (650 °C) did not cause any significant change. This can be explained by the relatively high (about 4 times higher) diffusivity of CH₄ in H₂ ($0.726 \text{ cm}^2\text{s}^{-1}$ [165])

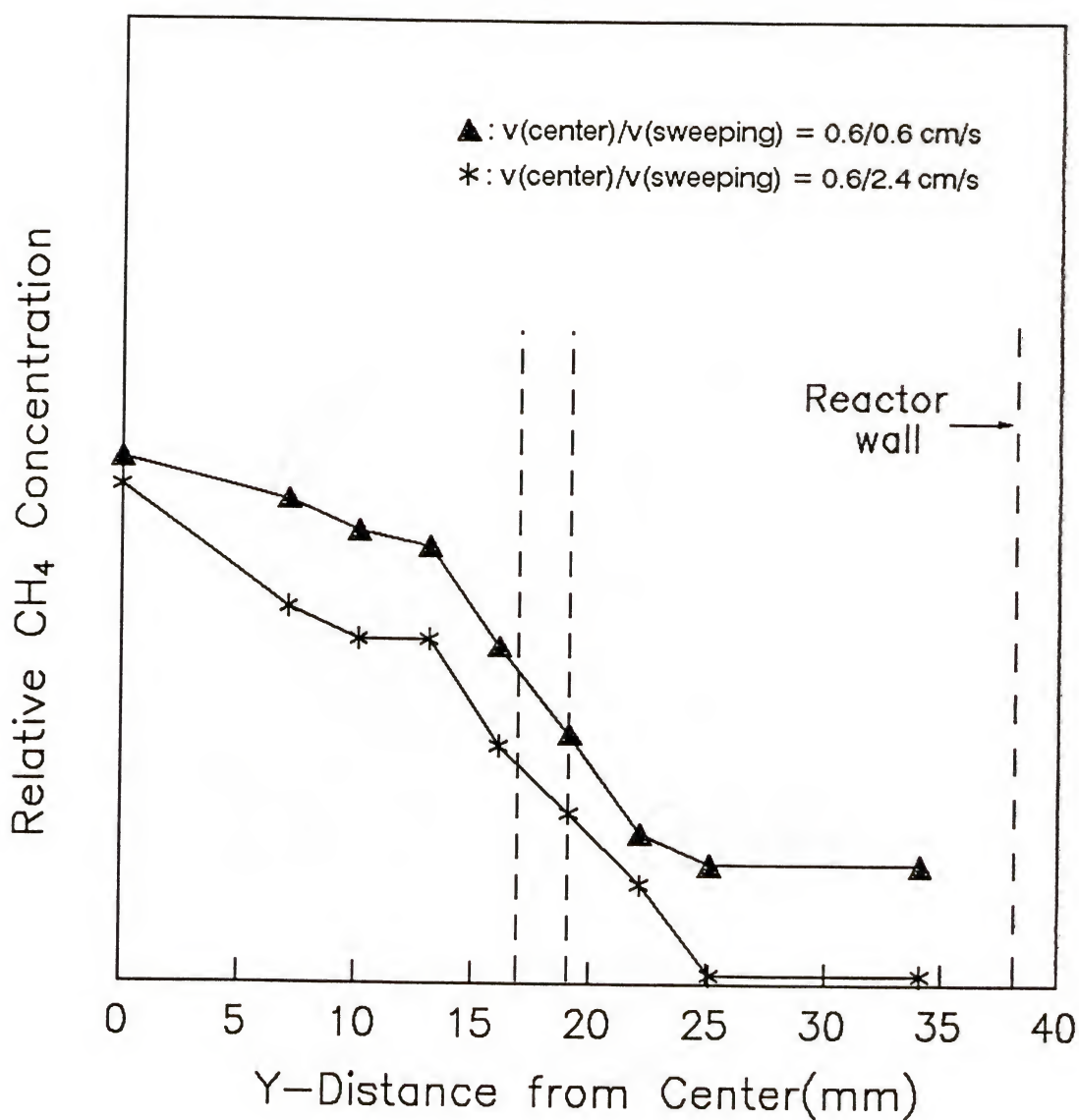


Figure 4-19: The relative CH₄ concentration profiles along the y-axis: effect of increasing the sweeping flow velocity with respect to the center flow velocity. N₂ carrier gas; $T_{\text{set}} = 650 \text{ }^{\circ}\text{C}$; AR = 0.9; $z = 27 \text{ mm}$ from the center flow inlet.

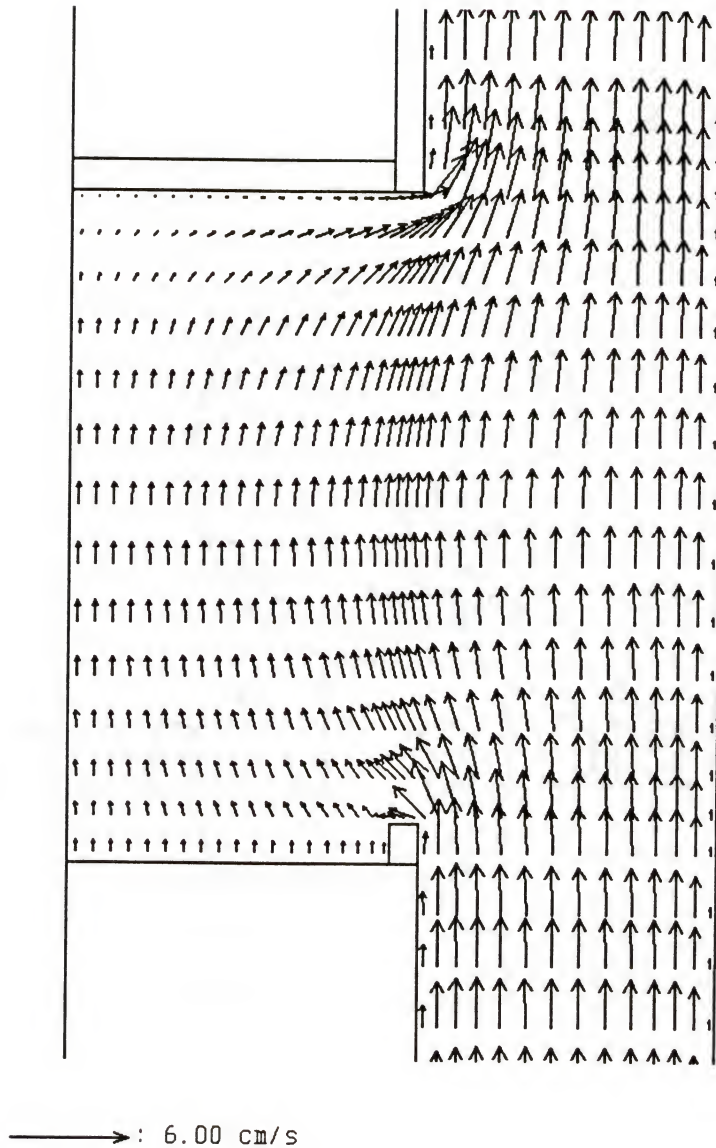


Figure 4-20: The calculated velocity profile in the reactor:
 effect of increasing the sweeping flow velocity with respect to
 the center flow velocity. N_2 carrier gas; $T_{\text{set}} = 25\text{ }^{\circ}\text{C}$; $AR = 0.9$;
 $v_c = 0.6\text{ cm/s}$; $v_s = 2.4\text{ cm/s}$.

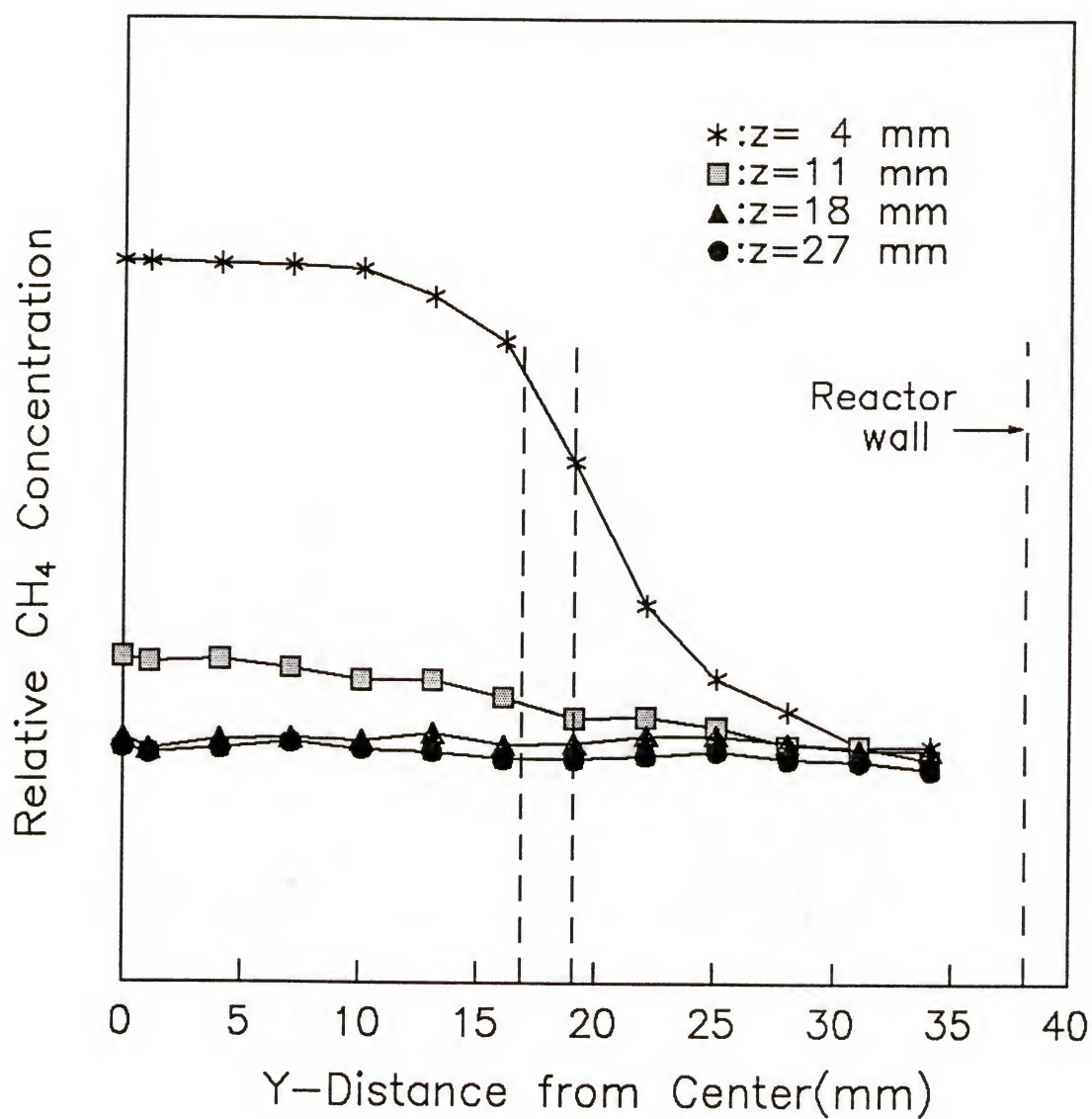


Figure 4-21: The relative CH₄ concentration profiles along the y-axis:
 matched inlet flow velocities; H₂ carrier gas; T_{set} = 25 °C
 AR = 0.9; v_c = 2.4 cm/s; v_s = 2.4 cm/s.

compared to that in N_2 ($0.196 \text{ cm}^2\text{s}^{-1}$ [165]). It was rather surprising to observe this fast dispersion of CH_4 in the reactor, and it is conceived that the reactants can be almost completely dispersed across the susceptor surface in the actual OMCVD reactors for epitaxial growth. The degree of dispersion, however, will depend on the specific reactant molecules involved in the process. This fast dispersion provides an advantage in the sense of achieving uniform inlet reactant concentrations with little effort, but it also provides a disadvantage in the sense of preventing wall depositions. The wall deposition is not desired in the growth of high quality epitaxial layers, since it can cause the growth rate variations and increased unintentional doping of the grown films. It is also detrimental in the kinetic study using in-situ optical techniques, since the experiment becomes time-dependent. Indeed, the wall depositions were observed, when TMI was introduced in a H_2 carrier gas with elevated susceptor temperature. The use of a sweeping flow could not successfully prevent the CH_4 dispersion toward the reactor wall within the operating range of this study. Further increase in the center flow velocity (9.6 cm/s) was studied and the results are shown in Figure 4-22. It shows a more confined center flow due to the increased center flow velocity, but still CH_4 was highly dispersed near the susceptor. Further increase in the velocity was not attempted, since the Raman signal became very noisy with increased velocity. The fluctuation in the signal seems to be caused by the eddies which are formed at the center flow inlet and transported with the flow.

The use of a N_2 carrier gas offers an advantage over H_2 in preventing the wall depositions. The introduction of a sweeping flow seems to be a good method. A concern in using the N_2 carrier gas, however, is the stability of the gas in a actual reactor configuration. The relative instability of N_2 compared to H_2 was reported by Giling[166] in terms of the transition from laminar flow to turbulent flow, the natural versus force convection, and the entrance effect. Thus, the design of reactor geometry must be carefully performed prior to realizing the advantages of using N_2 as a carrier gas.

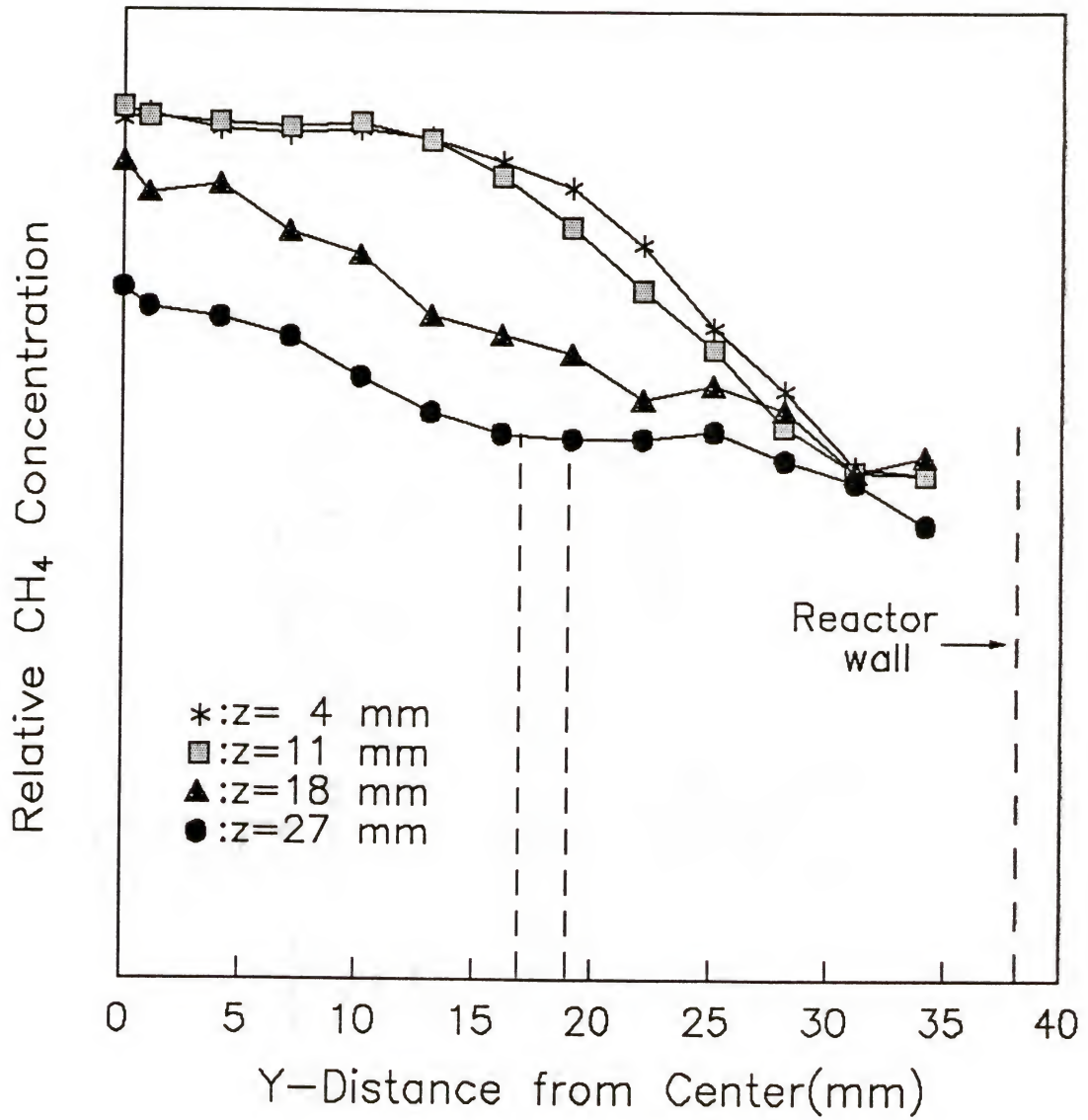


Figure 4-22: The relative CH₄ concentration profiles along the y-axis:
 unmatched inlet flow velocities; H₂ carrier gas; $T_{\text{set}} = 25$ °C
 $AR = 0.9$; $v_c = 9.6$ cm/s; $v_s = 2.4$ cm/s.

4.4.3 Tracer Study: Transient Response of the Reactor

The transient switching response of the reactor was studied by the CH_4 tracer. Initially, N_2 was used as a carrier gas. The center flow contained 10% CH_4 , and the sweeping flow contained pure N_2 . The Raman probe was moved along the centerline of the reactor ($y = 0$). At room temperature, it was found that the CH_4 intensity measured at the top position (2 mm from the susceptor surface) was about two times higher than the CH_4 intensity measured at the bottom position (12 mm from the susceptor surface), but when the Raman probe was moved slightly off the centerline at the top position, the CH_4 signal decreased drastically. It was conceived from this observation that the CH_4 molecules flow in a ribbon-like pattern and are not completely dispersed in N_2 . The reason for this phenomenon is not clear, but the sudden expansion of the flow cross-sectional area at the bottom of the inlet tube (Figure 4-1, 1/4" tubing to 1.5" tubing) may cause this flow instability. The gas injection from the side can worsen the situation (90° turn). However, this phenomenon was not observed, when N_2 was replaced by H_2 . It seems that the dispersion of CH_4 in H_2 is complete due to the relatively high diffusivity of CH_4 in H_2 . The relatively high flow stability of H_2 [166] helps the situation. Indeed, the almost complete dispersion of CH_4 in H_2 at typical operating conditions was observed as already discussed in the previous section. Packing of the center tube with glass beads enhanced the mixing of CH_4 with N_2 . However, since the packing of the center tube may introduce another variables in the experiment, H_2 carrier gas was used without the packing of the center tube for the experiment of the transient switching response of the reactor.

The transient response of the reactor to various injection times is shown in Figure 4-23. The Raman probe was fixed at 12 mm from the susceptor surface, and other operating conditions are listed in the figure caption. The center flow containing 10% CH_4 in H_2 was shunted through the reactor for labeled time period of 5 to 20 s. Under these conditions, the

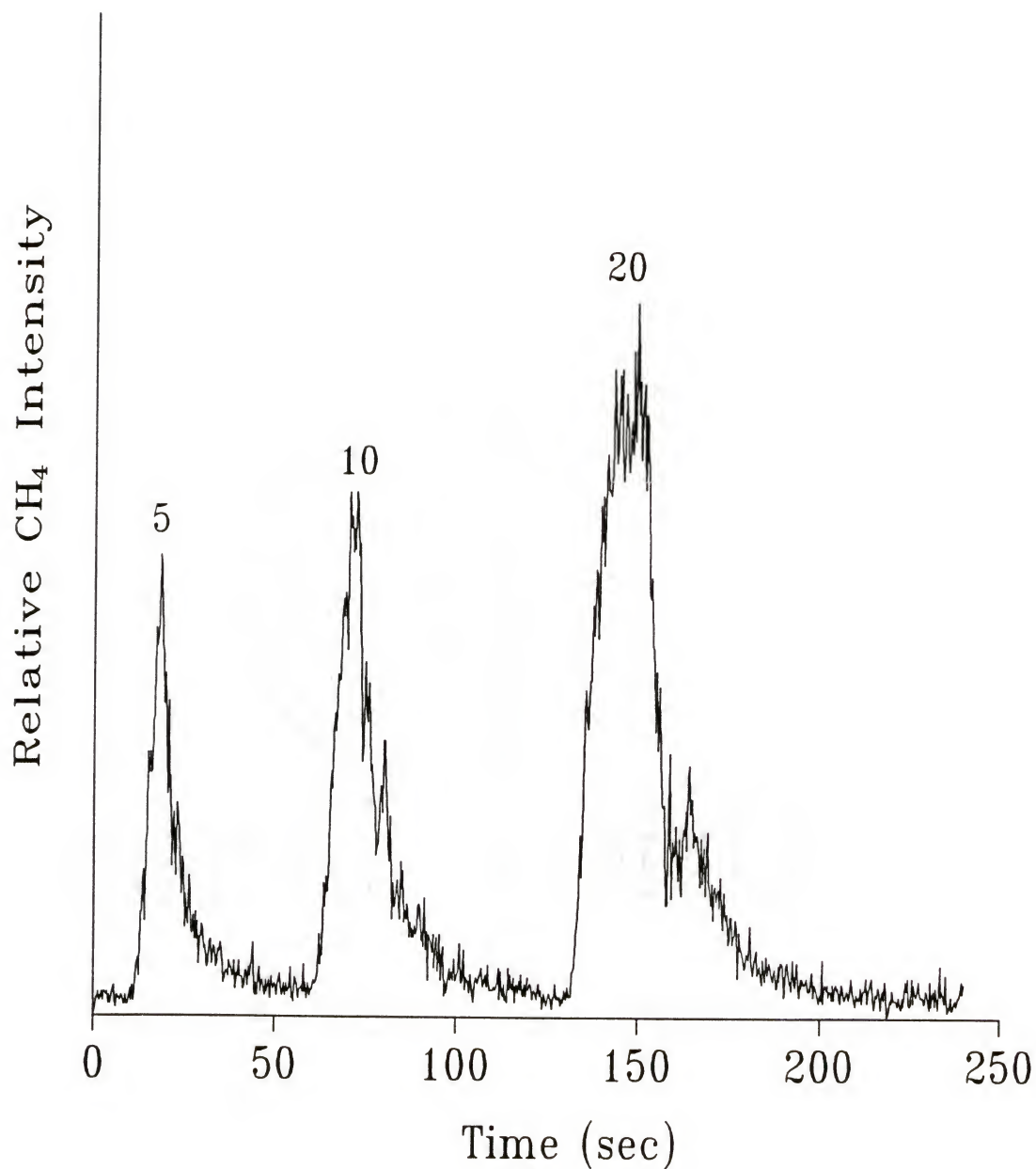


Figure 4-23: Time response of the reactor to several 10% CH_4 in H_2 injection times:
 The center flow is turned on for several time periods indicated by numbers next to the peaks. $T_{\text{set}} = 25^\circ\text{C}$; $\text{AR} = 1$; $v_c = 3.0\text{ cm/s}$; $v_s = 0.75\text{ cm/s}$;
 Probe position at $y = 0$ and $z = 12\text{ mm}$ from the susceptor.

flow stabilizes after approximately 15 s. Since the area under the on time curve represents the time integrated amount of CH_4 (after simple manipulation of the data) that has passed through the probe volume, the amount of a reactant introduced to the growth system can be monitored for exacting applications such as atomic layer epitaxy[6]. For several device structures such as very narrow quantum well devices, it is critical to precisely dope or deposit single monolayers reproducibly. Calibration of the flow system using this optical technique will allow an operator to precisely monitor and calibrate the dose of reactant gas in the system.

The time required for the reactant gas concentration to stabilize in an OMCVD reactor is of critical importance for the fabrication of abrupt interfaces and well-defined heterojunctions. Transient response of the reactor to several carrier gas flow velocities is shown in Figure 4-24. At time zero, the make-up flow was flowing in the center tube, and the sweeping flow was flowing. At time 10 sec, the center flow containing CH_4 was switched to the center tube and the make-up flow was switched to the vent. The center flow continued for 20 sec, and then it was switched back to the vent. The make-up flow was switched to the center tube at the same time. The velocities of center and sweeping flow were matched in this case. Increasing the H_2 carrier flow velocity has several effects. Increased flow velocity results in a shorter initial turn on time before any CH_4 signal is observed as well as a large increase in the rate of rise to the maximum intensity and an associated decrease in the time required to reach a steady state value. A long reactant residence time will result in a graded junction at an interface of heterostructures. The asymmetry of rise and fall seems to be caused by the stagnant volume in the center inlet tube (Figure 4-1). This asymmetry was also reduced with increasing carrier velocity. Similar results have been reported by Hebner *et al.*[146] in their study of vertical upflow reactor by UV absorption spectroscopy.

The effect of unmatched flow velocities between the center and the sweeping flow was also studied, and the results are shown in Figure 4-25. When the sweeping flow velocity was reduced to 0.75 cm/s from the matching velocity (3.0 cm/s), a shoulder peak appeared,

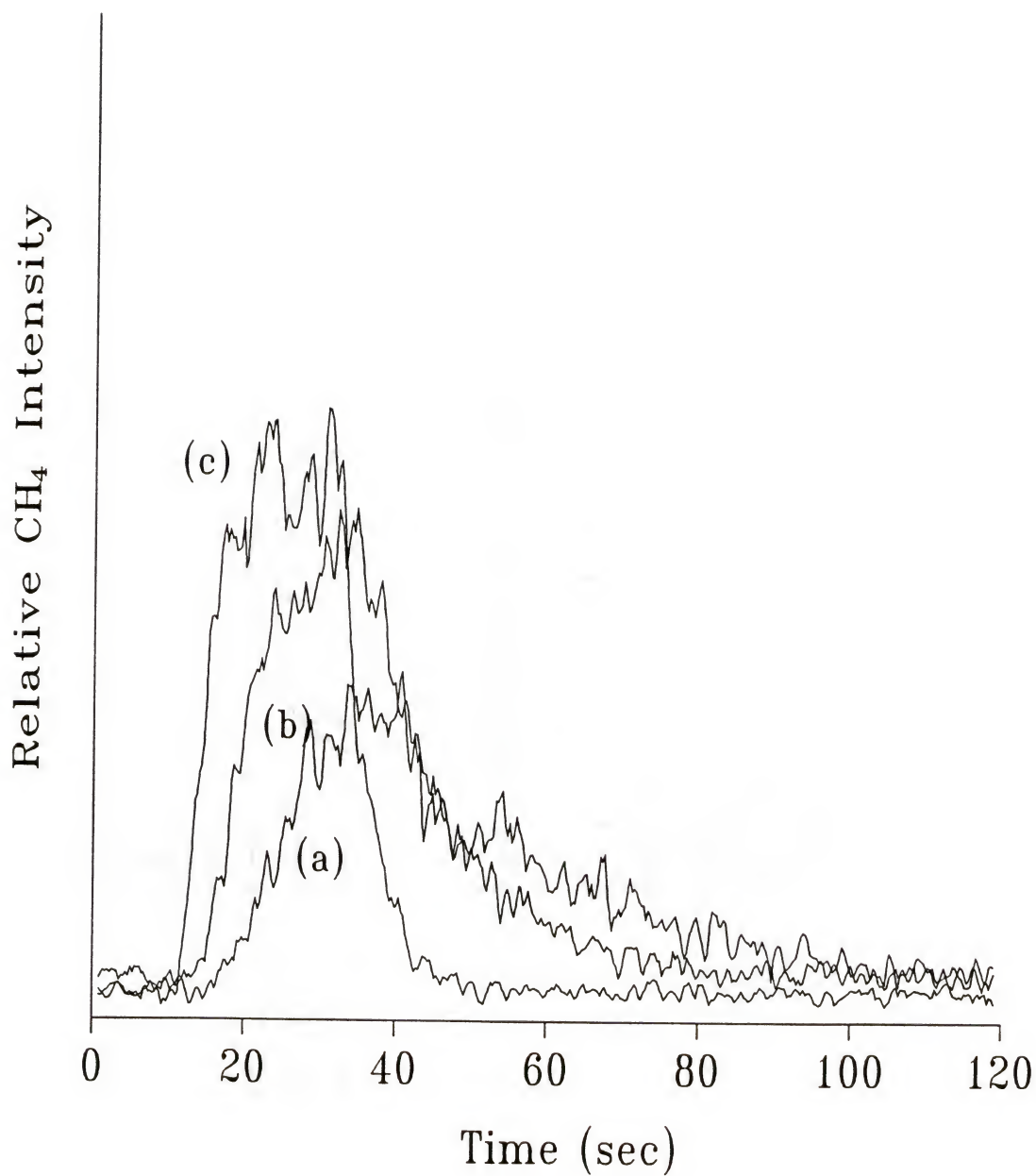


Figure 4-24: Time response of the reactor for several matched H_2 carrier velocities:

$T_{\text{set}} = 25\text{ }^\circ\text{C}$; $\text{AR} = 1$; (a) $v_c = 0.75\text{ cm/s}$, $v_s = 0.75\text{ cm/s}$; (b) $v_c = 1.5\text{ cm/s}$, $v_s = 1.5\text{ cm/s}$; (c) $v_c = 3.0\text{ cm/s}$, $v_s = 3.0\text{ cm/s}$;

Probe position at $y = 0$ and $z = 12\text{ mm}$ from the susceptor.

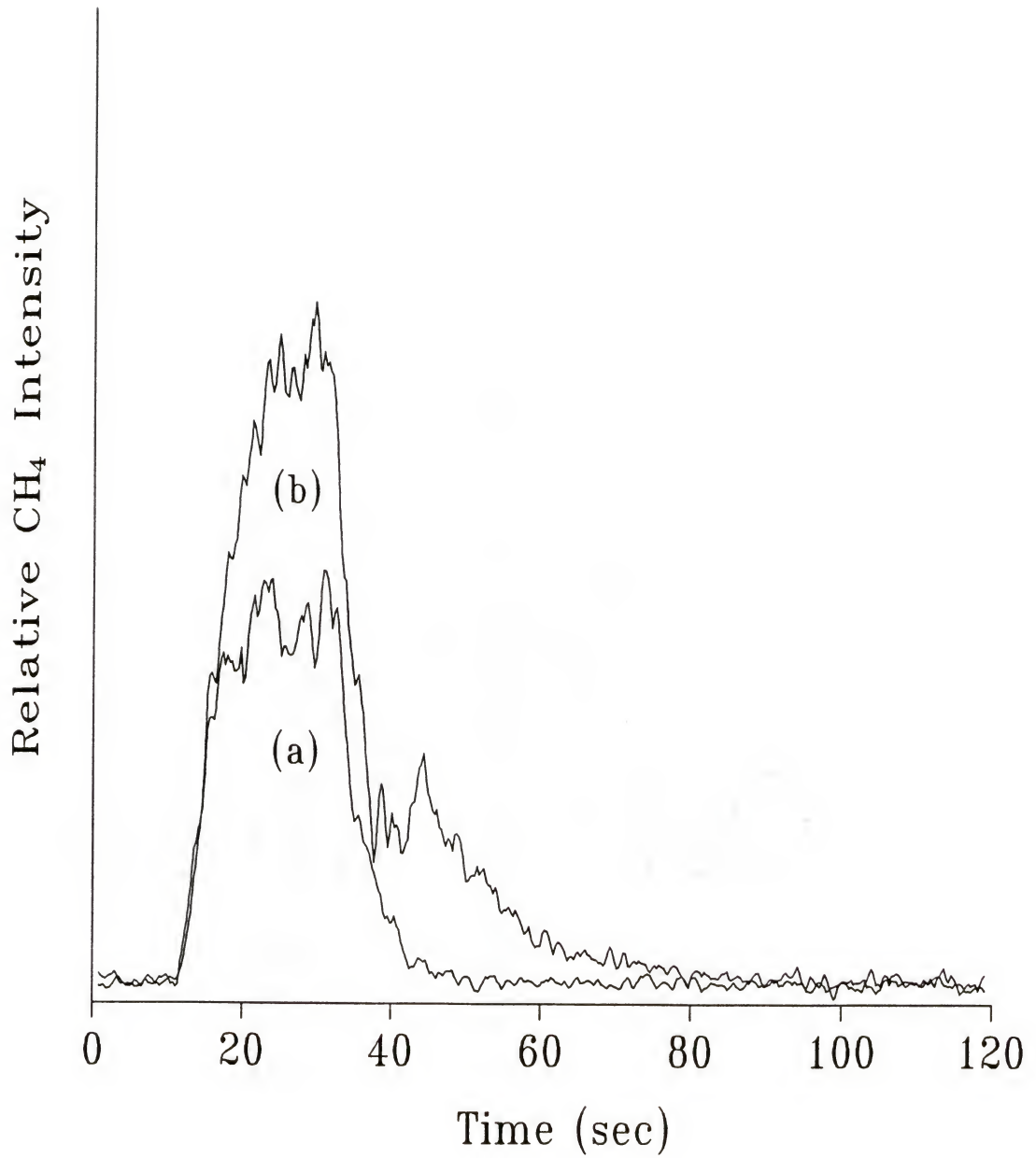


Figure 4-25: Time response of the reactor for unmatched H_2 carrier velocities:

$T_{\text{set}} = 25^\circ\text{C}$; $\text{AR} = 1$; (a) $v_c = 3.0\text{ cm/s}$, $v_s = 3.0\text{ cm/s}$;

(b) $v_c = 3.0\text{ cm/s}$, $v_s = 0.75\text{ cm/s}$;

Probe position at $y = 0$ and $z = 12\text{ mm}$ from the susceptor.

indicating that a recirculating flow was developed in the reactor because of the flow unmatching. This result is consistent with an observation in a steady flow condition (Figure 4-16), which was discussed in section 4.4.2. It seems that the unmatched flow velocities cause a recirculating flow pattern to develop even in the case of H_2 carrier gas.

4.5 Summary

A vertical upflow OMCVD reactor has been investigated in detail both by modeling and by experiment. Temperature profiles in the reactor was measured by pure rotational Raman scattering from the carrier gas molecules. It was found that a larger temperature gradient normal to the susceptor surface can be obtained with higher gas flow velocity, larger aspect ratio, and the use of a N_2 carrier gas. A two-dimensional axisymmetric model of the actual geometry was developed, and the calculated results were compared with the experiment. A good agreement in temperature profiles was obtained with proper corrections of the thermal boundary conditions. An accurate heat transfer characteristics was found to be critical in obtaining the accurate results. The buoyancy driven flow recirculations were found not to be much a problem except for very low gas flow velocities due to the stabilizing density gradient obtained by the upflow geometry.

The behavior of reactants in the reactor and the transient switching response of the reactor were studied by vibrational Raman scattering from a tracer species, CH_4 . The use of a sweeping flow was investigated as a method of preventing the wall depositions. The CH_4 dispersion toward the reactor wall could be completely blocked by the use of a sweeping flow in the case of N_2 carrier gas. However, it was not successful in the case of H_2 carrier gas because of the fast dispersion of CH_4 in H_2 . The importance of flow matching was emphasized to prevent the formation of laminar vortices caused by the flow instability.

The study of the transient switching response of the reactor revealed that the equilibration time for steady state flow conditions was decreased by increasing the carrier gas velocity. The design of gas inlet was found to be critical in obtaining a well-defined reactant flow especially with the use of N_2 carrier gas.

The use of a N_2 carrier gas offers many advantages over the use of a H_2 carrier gas from the gas dynamic standpoint. It provides a steeper temperature gradient normal to the susceptor surface, and the wall deposition can be completely suppressed with the velocity matched sweeping flow. However, a care has to be taken prior to realizing these advantages, because the N_2 carrier gas is sensitive to the conditions which can cause unexpected flow instabilities.

Based on the observations in this study, modifications were made for the gas inlet design to conduct a kinetic study for the growth of InP epitaxial films, and its schematic is shown in Figure 4-26. Water jacket was installed around the center tube to cool the center tube which is heated by radiation from the hot susceptor. This will cause the temperature gradient even steeper. The end of the jacket was rounded to remove the sharp corners, which will provide more gentle joint between the center and the sweeping flow. The center flow was introduced from the bottom, and the cross-sectional area was gradually increased to the size of the center tube. This prevents the sudden expansion of the flow and the sharp turn of the incoming gas which are the common cause of the flow instability. Initial studies of the TMI decomposition performed with the modified reactor, indeed, showed that with the use of a N_2 carrier gas, the narrow high temperature zone near the susceptor surface develops at the matched velocity of 2.0 cm/s, and the wall deposition is completely suppressed. No sign of flow instability was observed.

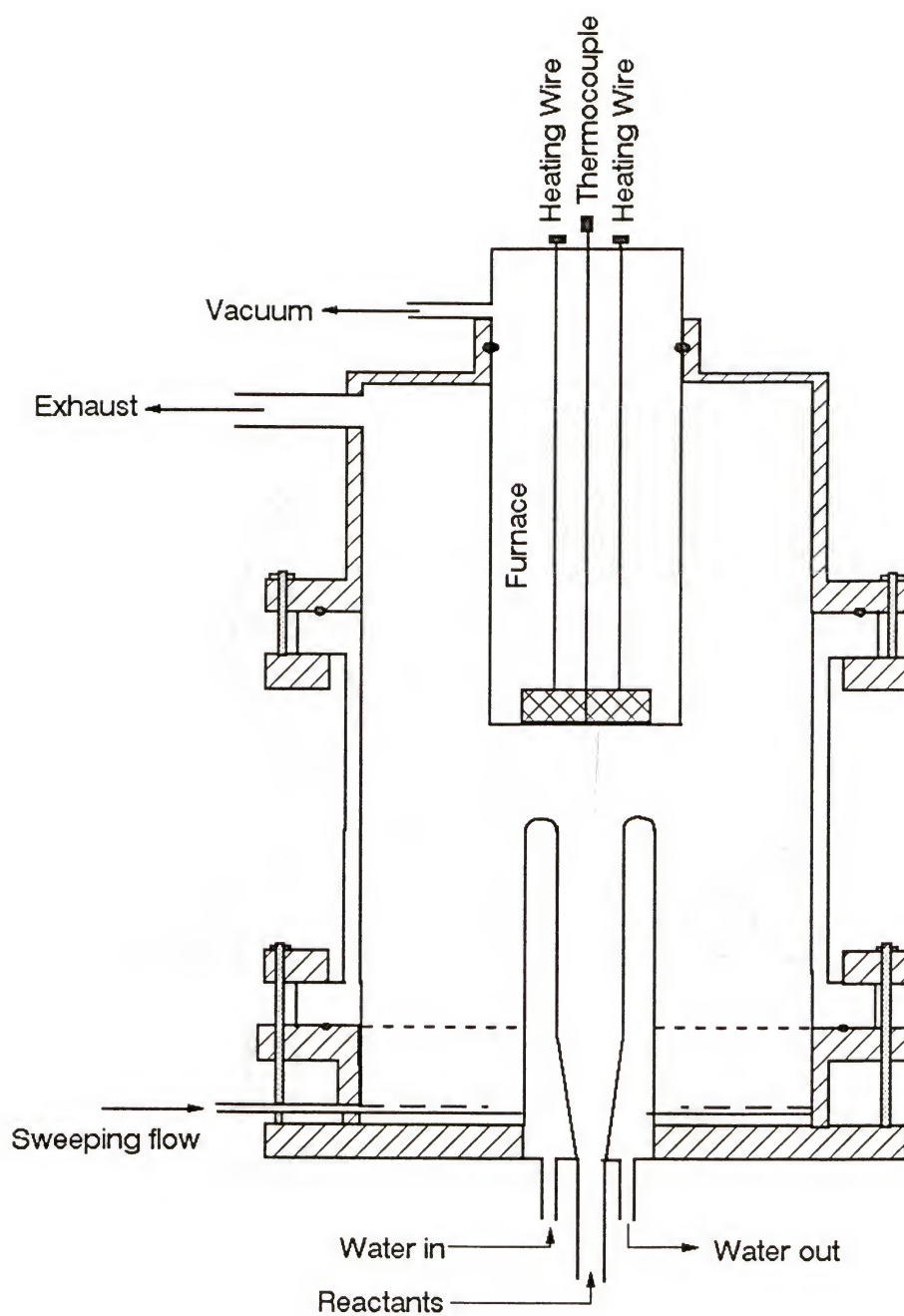


Figure 4-26: Schematic of a modified vertical upflow OMCVD reactor design.

CHAPTER V

CONCLUSIONS AND RECOMMENDED FUTURE WORK

In this dissertation work, several issues have been investigated in the growth of quaternary $\text{Ga}_x\text{In}_{1-x}\text{As}_y\text{P}_{1-y}$ compound semiconductor system by two major deposition techniques, hydride vapor phase epitaxy (VPE) and organo-metallic chemical vapor deposition (OMCVD).

The utilization of a Ga/In alloy as the group III source in the hydride VPE method was investigated for deposition of $\text{Ga}_x\text{In}_{1-x}\text{As}$. The effects of a wide range of experimental variables (*i.e.*, inlet mole fractions of HCl and AsH_3 , deposition temperature, gas velocity, Ga/In alloy composition, and reactor geometry) on the ternary composition and growth rate were investigated. The growth rate of $\text{Ga}_x\text{In}_{1-x}\text{As}$ was found to increase with increasing deposition temperature and exhibited a maximum with inlet HCl mole fraction. The growth rate increases slightly with inlet AsH_3 mole fraction and is independent of gas velocity. The Ga composition of the deposited film increased with increasing inlet HCl mole fraction and gas velocity. Increased In concentrations were observed with increases in inlet AsH_3 mole fraction and deposition temperatures. The results revealed that reaction kinetics and mass transfer play important roles, particularly in determining the growth-rate behavior.

A complex chemical equilibrium analysis of the Ga/In/As/Cl/H system was performed to evaluate the dependence of solid solution composition on process parameters at equilibrium conditions. A careful selection of species postulated to be present in the system was made, and the most updated thermochemical values were used after a critical review of the literatures. Several commonly used solution models were also tested and compared. The equilibrium analysis could explain the film compositional behavior for most process parameter changes.

Layers of $\text{Ga}_{0.47}\text{In}_{0.53}\text{As}$ latticed matched to InP were successfully grown from alloys containing 5 to 8 at.% Ga. These layers were used to produce state-of-the-art *p-i-n* photodetectors having the following characteristics: dark current, I_d (-5 V) = 10 - 20 nA; responsivity, R = 0.84 - 0.86 A/W; capacitance, C = 0.88 - 0.92 pF; break down voltage, V_b > 40 V. This study demonstrated for the first time that a simplified hydride VPE process with a Ga/In alloy source is capable of producing device quality epitaxial layers.

A problem with the technique is gallium depletion in the source with continued use. This problem is related in part to non-equilibrium conversion in the source zone. Improved reactor design for the source region with mixing zone HCl injection should extend the lifetime of an alloy source. An experimental study with the improved source zone design is suggested to fully exploit this simplified process into the actual production. Improvements in HCl conversion in the source zone can be achieved by increasing the reactant residence time, decreasing the transverse length scale, and increasing the diffusivity and reaction rate at the liquid surface. The reactant residence time can be increased by decreasing the gas velocity and/or increasing the contact length. The transverse length scale can be decreased by properly modifying the shape of the source boat. The diffusivity can be decreased by lowering the reactor pressure, but the decrease in the growth rate is also expected. The reaction rate at the liquid surface can be increased by increasing the source zone temperature, but the unintentional doping of the deposited film is also expected.

Background impurities in epitaxial layers of InP grown by the hydride VPE technique were studied by low temperature Fourier-transform photoluminescence (FTPL) spectroscopy and variable temperature Hall measurement. The Hall measurement was used to measure the net carrier concentration and mobility of InP films, and the FTPL spectroscopy was used to identify the major background impurities in the InP films. The effects of source zone temperature and inlet mole fractions of HCl and PH_3 on the extent of impurity incorporation were investigated. The background carrier concentration was found to decrease, and the

mobility was found to increase with decreasing source zone temperature and increasing HCl, but was relatively independent of PH_3 for the range of mole fraction studied. The electrical parameters of the InP films were extracted from the Hall data by performing a simple theoretical analysis, and the values were generally in agreement with reported values. The relatively high carrier concentration of the films generated lower values of donor ionization energy. The FTPL spectra revealed that the major impurities in the InP films are the Si donors and Zn acceptors. The impurity related peaks were quite broad due to the relatively high background impurity concentration. The observed behavior of unintentional doping of hydride VPE grown InP films could be explained by the thermodynamic prediction and the DiLorenzo and Moore's Si incorporation model.

Based on the results, lowering the source zone temperature and increasing inlet HCl mole fraction should lower the level of unintentional doping of the hydride VPE grown InP films. An experiment is suggested to further investigate the unintentional doping process. The effect of excess HCl downstream of the source zone on the impurity incorporation needs to be investigated. A wider range of inlet mole fraction of PH_3 needs to be studied. With the lower background concentration of InP films obtained by optimizing the process variables, it is necessary to run a high resolution FTPL spectra at low temperature (1.2 K) to separate the impurity induced photoluminescence peaks to more accurately identify the impurities in the epitaxial films.

A stagnation point flow OMCVD reactor in which cold gas flows up toward a resistively heated susceptor was investigated by gas phase laser Raman spectroscopy. Pure rotational Raman scattering from carrier molecules (N_2 or H_2) was used to determine the axial temperature in the reactor. The temperature profile was examined as a function of the inlet flow velocity and the reactor aspect ratio. A larger temperature gradient normal to the susceptor surface was obtained with higher gas flow velocity, larger aspect ratio, and the use of a N_2 carrier gas. The results were in good agreement with the computed profiles of a 2-

dimensional axisymmetric model after proper corrections were made for thermal boundary conditions. An accurate heat transfer description was found to be critical in obtaining the accurate results. The buoyancy driven flow recirculations were found to be not much of a concern except for very low flow velocities, due to the stabilizing density gradient provided by the inverted geometry.

The behavior of reactants in the reactor was studied by a tracer species, CH_4 . The use of a sweeping flow was found to be a good method of preventing the wall depositions in the case of N_2 carrier gas. However, it was not successful in the case of H_2 carrier gas because of the fast dispersion of CH_4 in H_2 . The velocity matching between the center and sweeping flow was found to be very important in the N_2 carrier gas. The study of the transient response of the reactor revealed that the equilibration time for steady state flow conditions was decreased by increasing the carrier gas velocity. The design of gas inlet was found to be critical with the use of N_2 carrier gas in order to have a well-defined reactant flow behavior in the reactor.

Based on the results obtained in this study, some modifications were made for the gas inlet design, and the modified reactor was tested in the kinetic study of TMI decomposition. Initial results were very encouraging. A narrow high temperature zone was obtained with the use of N_2 carrier gas, and no wall depositions were observed with the use of a sweeping flow of matched velocity. Actual growth experiments of InP films will verify the improved uniformity and high quality of the grown layers. The reactor model based on the modified design should give better agreement in the reactant flow behavior in the reactor. The addition of species balance equation will finalize the modeling effort to extract the kinetic data from the experiment measuring the reactant decomposition rates.

REFERENCES

- [1] Streetman, B. G., "Solid State Electronic Devices", 2nd ed., Prentice Hall, Englewood Cliffs, New Jersey, NJ, (1980).
- [2] Foyt, A. G., Proc. NATO InP Workshop, Hanscom AFB, RADC-TM-80-07, (1980).
- [3] Pearsall, T. P., IEEE J. Quant. Elect. QE-16, 709 (1980).
- [4] Greene, P. D., Wheeler, S. A., Adams, A. R., El-Sabbahy, A. N., and Ahmad, C. N., Appl. Phys. Lett. 35, 78 (1979).
- [5] Leheny, R. F., Ballmam, A. A., De Winter, J. C., Nahory, R. E., and Pollack, M. A., J. Electron. Mat. 9, 561 (1980).
- [6] Bedair, S. M., Tischler, M. A., and El-Masry, N., Appl. Phys. Lett. 47, 51 (1985).
- [7] Tsang, W. T., Appl. Phys. Lett. 45, 1234 (1984).
- [8] Kressel, H., J. Electron. Mat. 3, 747 (1974).
- [9] Kupal, E. J., J. Cryst. Growth 54, 117 (1981).
- [10] Bocchi, C., Ferrari, C., Franzosi, P., Fornuto, G., Pellegino, S., and Taiarol, F., J. Electron. Mat. 16, 245 (1987).
- [11] Barry, R. E., Thin Solid Films 39, 35 (1976).
- [12] Tietjen, J. J., Enstrom, R. E., and Richman, D., RCA Review 31, 635 (1970).
- [13] Olsen, G. H. and Zamerowski, T. J., IEEE J. Quant. Elect. QE-17, 128 (1981).
- [14] Ludowise, M. J., J. Appl. Phys. 58, R31 (1985).
- [15] Cho, A. Y., Jap. J. Appl. Phys. Suppl. 16-1, 435 (1977).
- [16] Cho, A. Y., J. Vac. Sci. Technol. 16, 275 (1979).

- [17] Longeway, P. A. and Smith, R. T., J. Cryst. Growth 89, 519 (1988).
- [18] Hsieh, J. J., Ph.D. Thesis, Dept. Chemical Engineering, Univ. of Florida, (1988).
- [19] Quinlan, K. P., J. Cryst. Growth 83, 319 (1987).
- [20] Quinlan, K. P., J. Electrochem. Soc. 135, 2108 (1988).
- [21] Ban, V. S., J. Electrochem. Soc. 118, 1473 (1971).
- [22] Karlicek, R. F., Hammarlund, B., and Ginocchio, I., J. Appl. Phys. 60, 794 (1986).
- [23] Minden, H. T., J. Electrochem. Soc. 112, 300 (1965).
- [24] Kordos, P., Schumbera, P., Heyen, M., and Balk, P., Proc. Int. GaAs and Related Compounds (Japan), No. 63, 131 (1981).
- [25] Chatterjee, A. K., Faktor, M. M., Lyons, M. H., and Moss, R. H., J. Cryst. Growth 56, 591 (1982).
- [26] Erstfeld, T. E. and Quinlan, K. P., J. Electrochem. Soc. 131, 2722 (1984).
- [27] Quinlan, K. P. and Erstfeld, T. E., J. Cryst. Growth 71, 246 (1985).
- [28] Jacobs, K., Bugge, F., and Simon, I., Cryst. Res. Tech. 21, 3 (1986).
- [29] Coronado, M. L., Abril, E. J., Balaguer, R., and Aguilar, M., Jpn. J. Appl. Phys. 27, 1268 (1988).
- [30] Olsen, G. H., Laser Focus 12, 124 (1985).
- [31] Olsen, G. H. and Zamerowski, T. J., RCA Review 44, 270 (1983).
- [32] Olsen, G. H. and Ban, V. S., Solid State Tech. 30, 99 (1987).
- [33] Smith, W. R., Ind. Eng. Chem. Fund. 19, 1 (1980).
- [34] Clasen, R. J., "Memorandum RM-4345-PR", The Rand Corporation, Santa Monica, CA, (1965).
- [35] Cruise, D. R., J. Phys. Chem. 68, 3797 (1964).
- [36] Anderson, T. J., Univ. of Florida, Proposal to the Dept. of the Air Force, (1979).
- [37] Meyer, D. J., Ph.D. Thesis, Dept. Chemical Engineering, Univ. of Florida, (1984).

- [38] Hultgren, R., Desia, P. D., Hawkins, D. T., Gleiser, K., Kelly, K. K., and Wagman, D. D., "Selected Values of the Thermodynamic Properties of the Elements", Am. Soc. Metals, Metals Park, Ohio, (1973).
- [39] Shaulov, U. K. and Mosin, A. M., Russ. J. Phys. Chem. 47, 844 (1973).
- [40] JANAF Thermochemical Tables, National Standard Reference Data Series 37, U. S. Bureau of Standards, Washington, D. C., (1971).
- [41] Mullin, J. B. and Hurle, D. J. T., J. Luminescence 7, 176 (1973).
- [42] Wagman, D. D., Evans, W. H., Parker, V. B., Halow, I., Bailey, S. M., and Schumm, R. H., Nat. Bur. Stds. Tech. Note 270-3, (1968).
- [43] Kelly, K. K., U. S. Bur. Mines. Bull., 584 (1961).
- [44] Report CODATA Task Group, J. Chem. Thermodynamics 8, 603 (1976).
- [45] JANAF Thermochemical Tables, J. Phys. Chem. Ref. Data 3, 311 (1974).
- [46] AitHou, A., Ph.D. Thesis, Chimie Appliquee, Univ. of Claude Bernard Lyon I, (1986).
- [47] Defoort, F., Ph.D. Thesis, Metallurgie, Institute of National Polytechnique of Grenoble, (1986).
- [48] Tmar, M., Ph.D. Thesis, Sciences Physique, Institute of National Polytechnique of Grenoble, (1985).
- [49] Panish, M. B. and Ilegems, M., Prog. Solid State Chem. 7, 39 (1972).
- [50] Anderson, T. J. and Ansara, I., J. Phase Equil. 12, 64 (1991).
- [51] Stringfellow, G. B., J. Phys. Chem. Solids 34, 1749 (1973).
- [52] Philips, J. C. and Van Vethen, J. A., Phys. Rev. 22, 70 (1969).
- [53] Guggenheim, E. A., "Mixtures", Oxford Press, London, England, (1952).
- [54] Onabe, K. J., Phys. Chem. Solids 43, 1071 (1982).
- [55] Stringfellow, G. B. and Greene, P. E., J. Phys. Chem. Solids 30, 1779 (1960).
- [56] Marboeuf, A. and Guillaume, J. C., Revue Phys. Appl. 19, 311 (1984).

- [57] Averbach, B. L., "Energetics in Metallurgical Phenomena", vol. II, Mueller, W. M. (Editor), Gordon and Breach, New York, (1965).
- [58] Hyder, S. B., Saxena, R. R., Chiao, S. K., and Yeats, R., Appl. Phys. Lett. 35, 787 (1979).
- [59] Shaw, D. W., J. Electrochem. Soc. 117, 683 (1970).
- [60] Putz, N., Veuhoff, E., Bachem, K. H., Balk, P., and Luth, H., J. Electrochem. Soc. 128, 2202 (1981).
- [61] Mizuno, O., Watanabe, H., and Shinoda, D., Jpn. J. Appl. Phys. 14, 184 (1975).
- [62] Swalin, R. A., "Thermodynamics of Solids", 2nd ed., John Wiley & Sons, New York, NY, (1972).
- [63] Nagai, H., J. Electrochem. Soc. 126, 1400 (1979).
- [64] Weyburne, D. W. and Quinlan, K. P., Report RADC-TR-85-238, (1985).
- [65] Jurgensen, H., Schmitz, D., Heyen, M., and Balk, P., Inst. Phys. Conf. Ser. No. 74, 199 (1985).
- [66] Buckley, D. N., J. Electron. Mat. 17, 15 (1988).
- [67] Jones, K. A. and Tu, C. W., J. Cryst. Growth 70, 127 (1984).
- [68] Shaw, D. W., J. Cryst. Growth 31, 130 (1975).
- [69] Ban, V. S. and Ettenberg, M., Proc. 4th Int. Conf. on CVD, The Electrochem. Soc., 30 (1973).
- [70] Ban, V. S., J. Cryst. Growth 17, 19 (1972).
- [71] Ban, V. S., J. Electrochem. Soc. 119, 761 (1972).
- [72] Ban, V. S. and Ettenberg, M., J. Phys. Chem. Solids 34, 1119 (1973).
- [73] Mizutani, T. and Watanabe, H., J. Cryst. Growth 59, 507 (1982).
- [74] Forrest, S. R., Ban, V. S., Gasparian, G., Gay, D., and Olsen, G. H., IEEE Electron Devices Lett. 9, 217 (1988).
- [75] Olsen, G. H., IEEE Electron Devices Lett. 2, 217 (1981).

- [76] McCollum, M. J., Kim, M. H., Bose, S. S., Lee, B., and Stillman, G. E., Appl. Phys. Lett. 53, 1868 (1988).
- [77] Kuphal, E. and Pocker, A., J. Cryst. Growth 58, 133 (1982).
- [78] Fairman, R. D., Omori, M., and Fank, F. B., Proc. 6th Intern. Symp. on Gallium Arsenide and Related Compounds, 45 (1976).
- [79] Zinkiewicz, L. M., Roth, T. J., Skromme, B. J., and Stillman, G. E., Inst. Phys. Conf. Ser. 56, 19 (1981).
- [80] Skromme, B. J., Low, T. J., Roth, T. J., Stillman, G. E., Kennedy, J. K., and Abrovkah, J. K., J. Electron. Mat. 12, 433 (1983).
- [81] Usui, A. and Watanabe, H., J. Electron. Mat. 12, 891 (1983).
- [82] Iwata, N. and Inossita, T., Appl. Phys. Lett. 50, 1361 (1987).
- [83] Olsen, G. H., "Proc. of the Symposium on III-V Opto-electronics Epitaxy and Device Related Processes", Keramidis, V. G. and Mahajan, S. (editor), Electrochem. Soc., Pennington, NJ, vol. 83-13, 231 (1983).
- [84] Cairns, B. and Fairman, R., J. Electrochem. Soc. 115, 3276 (1968).
- [85] Cairns, B. and Fairman, R., J. Electrochem. Soc. 117, 197C (1970).
- [86] Dilorenzo, J. V., Moore, G. E., and Machala, A. E., J. Electrochem. Soc. 117, 102C (1970).
- [87] DiLorenzo, J. V., Moore, G. E., J. Electrochem. Soc., 118, 1823 (1971).
- [88] Rai-Choudhury, P., J. Cryst. Growth 11, 113 (1971).
- [89] Ashen, D. J., Dean, P. J., Hurle, D. T. J., Mullin, J. B., Royle, A., and White, A. M., Proc. 5th Intl. Symp. on GaAs, Inst. Phys. Conf. Ser. 34 (1975).
- [90] Beiden, V. E., Dyachkova, N. M., Ivanyatin, L. A., and Nishanov, D., Izves. Akad. Nauk SSSR, Neorgan. Mat. 12, 1114 (1974).
- [91] Wolfe, C. M., Stillman, G. E., and Korn, D. M., Inst. Phys. Conf. Ser. 33b, 127 (1977).
- [92] Palm, L., Bruch, H., Bachem, K., and Balk, D. J., Electronic Mat. 8, 555 (1979).
- [93] Seki, H., Koukito, A., Seki, H., and Fujimoto, M., J. Cryst. Growth 43, 159 (1978).

- [94] Clarke, R. C., J. Cryst. Growth 23, 166 (1974).
- [95] Chevrier, J., Huber, A., and Linh, N. T., J. Cryst. Growth 47, 267 (1979).
- [96] Cardwell, M. J., Giles, P. L., Hales, M. C., and Stirland, D. J., Proc. 1980 NATO InP Workshop, Hanscom AFB, 285 RADC-TM-80-07, (1980).
- [97] Pogge, H. B. and Kemlage, B. M., J. Cryst. Growth 31, 183 (1975).
- [98] Kennedy, J. K., Potter, W. D., and Davies, D. E., J. Cryst. Growth 24, 233 (1974).
- [99] Enstrom, R. E. and Appert, J., J. Electrochem. Soc. 129, 2566 (1982).
- [100] Jones, K. A., J. Cryst. Growth 60, 313 (1982).
- [101] Buckley, D. N., J. Electrochem. Soc., 137, 1219 (1990).
- [102] Anderson, T. J., Research Report, USAF Rome Air Development Center, F49620-79-C-0038.
- [103] Howard, A. J., Ph.D. Thesis, Dept. Chemical Engineering, Univ. of Florida (1990).
- [104] Duncan, W. M., SPIE vol. 822, Raman and Luminescence Spectroscopy in Technology, 172 (1987).
- [105] Rowell, N. L., SPIE vol. 822, Raman and Luminescence Spectroscopy in Technology, 161 (1987).
- [106] Bell, R. J., "Introductory Fourier Transform Spectroscopy", Academic Press, New York, NY, (1972).
- [107] Anderson, D. A. and Apsley, N., The Institute of Physics, 187 (1986).
- [108] Skolnick, M. S. and Dean, P. J., J. Phys. C: Solid State Phys. 15, 5863 (1982).
- [109] Barry Bebb, H. and Williams, E. W., "Semiconductors and Semimetals", Willardson, R. K. and Beer, A. C. (Editor), Academic Press, New York, NY, (1966).
- [110] Dean, P. J., "Progresses in Crystal Growth Characterization", vol. 5, Pergamon Press, London, England, (1982).
- [111] Monemar, B., "Treatise on Materials Science and Technology", vol. 19, Herman, H (Editor), Academic Press, New York, NY, (1980).

- [112] Skromme, B. J., Stillman, G. E., Oberstar, J. D., and Chan, S. S., Appl. Phys. Lett. 44, 319 (1984).
- [113] Chevrier, J., Huber, A., and Linh, N. T., J. Appl. Phys. 51, 815 (1980).
- [114] Fairman, R. D., Omori, M., and Fank, F. B., Inst. Phys. Conf. Ser., No.33b, 45 (1977).
- [115] Chevrier, J., Horache, E., Goldstein, L., and Linh, N. T., J. Appl. Phys. 53, 3247 (1982).
- [116] Gerrard, N. D., Nicholas, D. J., Williams, J. O., Jones, A. C., Chemtronics 3, 17 (1988).
- [117] Zhu, L. D., Chan, K. T., Wagner, D. K., and Ballantyne, J. M., J. Appl. Phys. 57, 5486 (1985).
- [118] Bose, S. S., Szafrank, I., Kim, M. H., and Stillman, G. E., Appl. Phys. Lett. 56, 752 (1990).
- [119] Uwai, K., Yamada, S., and Takahei, K., J. Appl. Phys. 61, 1059 (1987).
- [120] Kellert, F. G., Whelan, J. S., and Chan, K. T., J. Electron. Mat. 18, 355 (1989).
- [121] Ovadia, S. and Iliadis, A., SPIE vol. 822, Raman and Luminescence Spectroscopy in Technology, 40 (1987).
- [122] Inoue, T., Shimakura, H., Kainosho, K., Hirano, R., and Oda, O., J. Electrochem. Soc. 137, 1283 (1990).
- [123] Heim, U., Roder, O., Queisser, H. J., and Pilkuhn, M., J. Luminescence 1, 542 (1970).
- [124] Bonner, W. A. and Temkin, H., J. Cryst. Growth 64, 10 (1983).
- [125] Hirtz, J. P., Razeghi, M., Bonnet, M., and Duchemin, J. P., "GaInAsP Alloy Semiconductors", Pearsall, T.P. (Editor), John Wiley & Sons, New York, NY, (1982).
- [126] Kuech, T. F., Mater. Sci. Rept. 2,1 (1987).
- [127] Jensen, K. F., J. Cryst. Growth 98, 148 (1989).
- [128] Michealidis, M. and Pollard, R., J. Electrochem. Soc. 131, 860 (1984).
- [129] Wahl, G., Thin Solid Films 40, 13 (1977).

- [130] Wang, C. A., Groves, S. H., and Palmateer, S. C., *J. Cryst. Growth* 77, 136 (1986).
- [131] Fotiadis, D. I., Kremer, A. M., Mckenna, D. R., and Jensen, K. F., *J. Cryst. Growth* 85, 154 (1987).
- [132] Fotiadis, D. I., Kieda, S., and Jensen, K. F., *J. Cryst. Growth* 102, 441 (1990).
- [133] Monteil, Y., Favre, R., Bekkaoui, A., Raffin, P., Bouix, J., Marcillat, J., and Dutto, P., *J. Cryst. Growth* 93, 270 (1988).
- [134] Houtman, C., Graves, D. B., and Jensen, K. F., *J. Electrochem. Soc.* 133, 961 (1986).
- [135] Lee, P., Mckenna, D., Kapur, D., Jensen, K. F., *J. Cryst. Growth* 77, 120 (1986).
- [136] Takahashi, R., Koga, Y., and Sugawara, K., *J. Electrochem. Soc.* 119, 1406 (1972).
- [137] Koppitz, M., Vestavik, O., Pletschen, W., Mircea, A., Heyen, M., and Richter, W., *J. Cryst. Growth* 68, 136 (1984).
- [138] Monteil, Y., Berthet, M. P., Favre, R., Hariss, A., Bouix, J., Vaille, M., and Gibart, P., *J. Cryst. Growth* 77, 172 (1986).
- [139] Stock, L. and Richter, W., *J. Cryst. Growth* 77, 144 (1986).
- [140] Fotiadis, D. I., Boekholt, M., Jensen, K. F., and Richter, W., *J. Cryst. Growth* 100, 577 (1990).
- [141] Giling, L. J., *J. Electrochem. Soc.* 129, 634 (1982).
- [142] Moffat, H. and Jensen, K. F., *J. Cryst. Growth* 77, 108 (1986).
- [143] Jensen, K. F., Fotiadis, D. I., and Mountziaris, T. J., *J. Cryst. Growth* 107, 1 (1991).
- [144] Van de Ven, J., Rutten, G. M. J., Raaijmakers, M. J., and Giling, L. J., *J. Cryst. Growth* 76, 352 (1986).
- [145] Sillmon, R. S., Bottka, N., Butler, J. E., and Gaskill, D. K., *J. Cryst. Growth* 77, 73 (1986).
- [146] Hebner, G. A., Killeen, K. P., and Biefeld, R. M., *J. Cryst. Growth* 98, 293 (1989).

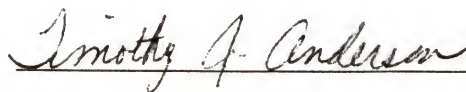
- [147] Haspeklo, H., Konig, U., Heyen, M., and Jurgensen, H., *J. Cryst. Growth* 77, 79 (1986).
- [148] Boldish, S. I., Ciofalo, J. S., and Wendt, J. P., *J. Electron. Mat.* 14, 587 (1985).
- [149] Boldish, S. I. and Ciofalo, J. S., U. S. Patent 4,777,022, Oct. 11 (1988).
- [150] Ban, V. S., *J. Electrochem. Soc.* 125, 317 (1978).
- [151] Giling, L. J., *J. Physique* 43, C5-235 (1982).
- [152] Long, D. A., "Raman Spectroscopy", McGraw-Hill, New York, NY, (1986).
- [153] Schrotter, H. W. and Klockner, H. W., "Raman Spectroscopy of Gases and Liquids", Weber, A. (Editor), Springer, Berlin, Germany, (1979).
- [154] James, T. C. and Klemperer, W., *J. Chem. Phys.* 31, 130 (1959).
- [155] Asawaroengchai, C. and Rosenblatt, G. M., *J. Chem. Phys.* 72, 2664 (1980).
- [156] Cheung, L. M., Bishop, D. M., Drapcho, D. L., and Rosenblatt, G. M., *Chem. Phys. Lett.* 80, 445 (1981).
- [157] Bendtsen, J., *J. Raman Spectroscopy* 2, 133 (1974).
- [158] Huber, K. P. and Herzberg, G., "Constants of Diatomic Molecules", Van Nostrand, New York, NY, (1979).
- [159] Drake, M. C. and Rosenblatt, G. M., *Chem. Phys. Lett.* 44, 313 (1976).
- [160] Bird, R. B., Stewart, W. E., and Lightfoot, E. N., "Transport Phenomena", John Wiley & Sons, New York, NY, (1960).
- [161] Jenkinson, J. P. and Pollard, R., *J. Electrochem. Soc.* 131, 2911 (1984).
- [162] Weast, R. C. (Editor), "Handbook of Chemistry and Physics", 67th ed., CRC Press, Boca Raton, FL, (1987).
- [163] White, F. M., "Heat Transfer", Addison-Wesley, Reading, MA, (1984).
- [164] Sacilotti, M., Mircea, A., and Azoulay, R., *J. Cryst. Growth* 63, 111 (1983).
- [165] Cussler, E. L., "Diffusion Mass Transfer in Fluid Systems", Cambridge University Press, London, England, (1984).

- [166] Giling, L. J., "Crystal Growth of Electronic Materials", Kaldis, E. (Editor), Elsevier Science, (1985).

BIOGRAPHICAL SKETCH

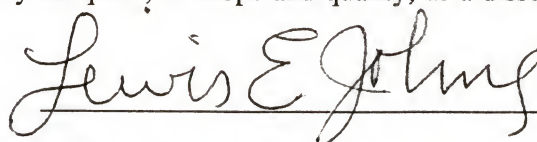
Chinho Park was born on August 22, 1958, in Choongmu, Korea, which is located on the southern shore of Korean peninsula. His family later moved to Seoul, Korea, where he received his primary and high school education. He graduated from Hanyang University with a Bachelor of Science degree in chemical engineering in 1981. He enrolled at Seoul National University in the same year for his Master of Science degree in chemical engineering. As part of his master's program, the author spent a year and six months at the Reaction Engineering Laboratory of Korea Advanced Institute of Science and Technology performing research on the supported metal catalysts in methanation reaction. He received his M.S. degree in 1983. After serving in the Republic of Korea Army Reserve as commissioned second lieutenant, the author joined the Semiconductor Division of Hyundai Electronics Industries, Co., Ltd., in Ichon, Korea, in 1984, at the very early stage of the company. As a process engineer, he was involved in variety of projects with extensive work in wet chemical etching, plasma etching, multilevel metallization technology, and process integration of VLSI memory devices. In 1987, the author was admitted to the University of Florida in Gainesville, Florida, to pursue his Ph.D. degree in chemical engineering. His graduate research has been focused on the growth of GaInAsP on InP by hydride VPE technique, reaction thermodynamics of hydride VPE, investigation of an OMCVD reactor by gas phase laser Raman spectroscopy, characterization of semiconductors, and micro-Raman spectroscopy of solids. The author plans to work in a semiconductor device manufacturing company upon his completion of his Doctor of Philosophy degree in chemical engineering.

I certify that I have read this study and that in my opinion it conforms to acceptable standards of scholarly presentation and is fully adequate, in scope and quality, as a dissertation for the degree of Doctor of Philosophy.



Timothy J. Anderson, Chairman
Professor of Chemical Engineering

I certify that I have read this study and that in my opinion it conforms to acceptable standards of scholarly presentation and is fully adequate, in scope and quality, as a dissertation for the degree of Doctor of Philosophy.



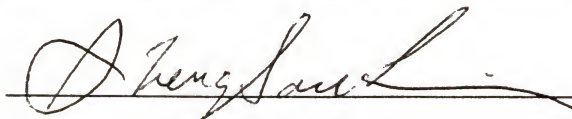
Lewis E. Johns
Professor of Chemical Engineering

I certify that I have read this study and that in my opinion it conforms to acceptable standards of scholarly presentation and is fully adequate, in scope and quality, as a dissertation for the degree of Doctor of Philosophy.



Chang-Won Park
Assistant Professor of Chemical Engineering

I certify that I have read this study and that in my opinion it conforms to acceptable standards of scholarly presentation and is fully adequate, in scope and quality, as a dissertation for the degree of Doctor of Philosophy.



Sheng S. Li
Professor of Electrical Engineering

I certify that I have read this study and that in my opinion it conforms to acceptable standards of scholarly presentation and is fully adequate, in scope and quality, as a dissertation for the degree of Doctor of Philosophy.



Vladimir S. Ban
Executive Vice President, Epitaxx, Inc.

This dissertation was submitted to the Graduate Faculty of the College of Engineering and to the Graduate School and was accepted as partial fulfillment of the requirements for the degree of Doctor of Philosophy.

August 1992

A handwritten signature in dark ink, appearing to read "W. Phillips", written over a horizontal line.Handwritten initials "for" in dark ink, positioned to the left of the printed name.

Winfred M. Phillips
Dean, College of Engineering

Madelyn M. Lockhart
Dean, Graduate School